CENTRO DE INVESTIGACIÓN Y DE ESTUDIOS AVANZADOS DEL INSTITUTO POLITÉCNICO NACIONAL

UNIDAD MÉRIDA
DEPARTAMENTO DE FÍSICA APLICADA

Nanostructured ZnO films: growth and doping from standard and hybrid targets and its applications as antireflective transparent conductive oxide

Tesis que presenta

Enrique Adrián de Atocha Martín Tovar

Para obtener el grado de

Doctor en Ciencias

En Fisicoquímica

Director de tesis:

Dr. Román Ernesto Castro Rodríguez

Mérida, Yucatán, México. Agosto 2017

CENTRO DE INVESTIGACIÓN Y DE ESTUDIOS AVANZADOS DEL INSTITUTO POLITÉCNICO NACIONAL

UNIDAD MÉRIDA
DEPARTAMENTO DE FÍSICA APLICADA

Películas nanoestructuradas de ZnO: crecimiento y dopaje a partir de blancos estándar e híbridos y sus aplicaciones como oxido anti-reflejante conductor.

Tesis que presenta

Enrique Adrián de Atocha Martín Tovar

Para obtener el grado de

Doctor en Ciencias

En Fisicoquímica

Director de tesis:

Dr. Román Ernesto Castro Rodríguez

Mérida, Yucatán, México. Agosto 2017

DEDICATORIAS

A mi madre, María Concepción, a su amor y valentía debo lo que soy. En todos y cada uno de mis logros puedo citarla como la autora principal.

A mis hermanos, Macarena, Ernesto y Daniela, por su afecto fraternal y su paciencia en todas y cada una de mis excentricidades.

A mis sobrinas Kathia y Samantha, que son como mis hermanas.

A Elizabeth, mi compañera, porque su amor y cariño me han vuelto un mejor hombre.

AGRADECIMIENTOS

- Al Consejo Nacional de Ciencia y Tecnología (CONACYT) por el apoyo económico brindado a través de una beca para mis estudios de doctorado.
- Al Dr. Román Ernesto Castro Rodríguez, director de esta tesis, su guía, constante apoyo e invaluable amistad me han formado como el hombre de ciencia que soy.
- Al Dr. Augusto Andrés Iribarren Alfonso, por sus grandes aportaciones, consejos y guía para la realización de este trabajo.
- Al M. en C. Luis Germán Daza Casiano, por su amistad y acompañamiento en todas las aventuras y vivencias que a lo largo de estos años pudimos compartir.
- Al M. en C. Mario Herrera Salvador y al Ing. Oswaldo Gómez por todo su apoyo técnico y paciencia, sin duda gracias a su habilidad técnica mi trabajo doctoral se desarrolló con éxito.
- A Lourdes Pinelo Rivera y Zhirnay Rodríguez por su eficaz, paciente y oportuno apoyo secretarial.
- Al personal técnico del Cinvestav Unidad Mérida: Ing. Wilian Cauich, M. en C. Dora Huerta, M. en C. Daniel Aguilar y M. en C. Mauricio Romero por su apoyo en toda medición y caracterización realizada en este trabajo.
- A la Dra. Milenis Acosta Díaz, por su apoyo en las mediciones de propiedades eléctricas.
- A los profesores que aceptaron formar parte del sínodo, por el tiempo invertido en la revisión de este trabajo y sus valiosos comentarios.
- A los profesores del Departamento de Física Aplicada por todas sus enseñanzas.
- A mis amigos y compañeros del Cinvestav Unidad Mérida, por hacer más amena y enriquecedora esta etapa de mi vida.
- Al Cinvestav-Unidad Mérida por todo el apoyo recibido.
- Al Dr. Enrique Chan y Díaz por su colaboración científica como parte de su estancia posdoctoral.
- Al CONACYT por su apoyo al proyecto No. CB/2012/17874813 CONACYT/México, bajo el cual fue desarrollada parte de esta tesis.

ABSTRACT

The present work is based on the study of thin films of pure and doped ZnO, grown by the pulsed laser ablation and magnetron sputtering techniques under a wide variety of conditions, emphasizing on their nanostructuration.

The CdTe isoelectronic doping of ZnO thin films deposited on glass substrates by the pulsed laser deposition was investigated. The reduction of the structural defects such as oxygen vacancies and interstitial zinc atoms, which frequently appear in the crystalline lattice of ZnO, was the primary interest of this work. The obtained results showed the successful formation of a hexagonal structure which is characteristic of ZnO along with Zn-Te bonds, which would prove the occupation of the oxygen vacancies by Te atoms in the ZnO crystalline lattice, additionally Cd- Te and Te-O bonds were found, although in a lesser extent.

ZnO thin films were grown by the pulsed laser deposition technique on glass substrates using two types of targets, the first one made with pure ZnO and the second one with pure ZnO embedded within a cyanoacrylate glue matrix, this was done in order to make a comparison between the resulting physical properties, as well as to perform a nitrogen doping. The films grown with the second target had a diffraction pattern very similar to the powder pattern which is used as reference for ZnO, suggesting that the incorporation of cyanoacrylate reduces stress and improves the crystalline structure of the samples. The chemical studies confirmed the formation of Zn-N bonds, along with Zn-O bonds. Additionally, the comparisons between the morphological, structural and optical properties for both type of targets is presented.

The effect of substrate rotation on the optical, structural, morphological and electrical properties of aluminum doped ZnO thin films (AZO) grown by magnetron sputtering technique was investigated. The characterizations results showed that the substrate's rotation speed had a deep influence on the morphological and structural properties of the deposited films, specifically a columnar deposit was obtained, which presented a greater definition as the rotation speed increased.

Finally, the properties of AZO thin films grown with the magnetron sputtering technique and the oblique angle deposition method were investigated. A tilted nanocolumnar deposit was obtained which was related to inclination angle of the substrate. The effect of this growth method on the optical properties was investigated, in particular the refraction index, which decreased by 16% due to the columnar growth.

RESUMEN

El presente trabajo se basa en el estudio de películas delgadas de ZnO puro y dopado, crecido a través de las técnicas de ablación con láser pulsado y erosión catódica con magnetrón bajo una variedad de condiciones, haciendo énfasis en conseguir su crecimiento en forma nano-estructurada.

Se investigó el dopaje isoelectrónico del ZnO con CdTe para películas delgadas crecidas con la técnica de láser pulsado sobre vidrio, para buscar la reducción en los defectos estructurales tales como vacancias de oxígeno y zinc intersticial, los cuales se presentan con frecuencia en la red cristalina del ZnO. Los resultados obtenidos demostraron la formación exitosa de una estructura hexagonal característica del ZnO y de enlaces Zn-Te, lo cual probaría la ocupación de vacancias de oxígeno por átomos de Te en la red cristalina del ZnO, también se encontraron en menor proporción enlaces Cd-Te y Te-O.

Se crecieron películas delgadas de ZnO por medio de la técnica de láser pulsado sobre substratos de vidrio haciendo uso de dos tipos de blancos, el primero fabricado con ZnO puro y el segundo compuesto de ZnO puro embebido dentro de una matriz de cianoacrilato, con el fin de hacer una comparación entre las propiedades físicas resultantes, así como realizar un dopaje con nitrógeno. Las películas crecidas con el segundo blanco presentaron un patrón de difracción muy similar al patrón en polvo que se usa como referencia en el ZnO, esto sugiere que la incorporación del cianoacrilato reduce el estrés y mejora la estructura cristalina en las muestras. Los estudios químicos confirmaron la formación de enlaces Zn-N, junto con Zn-O, se presentan además las comparaciones entre las propiedades morfológicas, estructurales y ópticas para las muestras crecidas con ambos blancos.

Se realizó un estudio sobre el efecto de la rotación de substrato en las propiedades ópticas, estructurales, morfológicas y eléctricas de películas delgadas de ZnO dopadas con aluminio (AZO) crecidas por medio de la técnica de erosión catódica con magnetrón. Los resultados de las caracterizaciones mostraron que la velocidad de rotación de substrato tenía influencia en las propiedades morfológicas y estructurales de las películas depositadas, específicamente se obtuvo un depósito columnar, el cual fue presentando una mayor definición conforme se aumentaba la velocidad de rotación.

Finalmente, se investigaron las propiedades de películas delgadas AZO crecidas con la técnica de erosión catódica con magnetrón y con el método depósito por ángulo oblicuo. Se obtuvo un depósito nanocolumnar inclinado que estaba relacionado con el ángulo de inclinación del substrato. Se realizó un estudio del efecto de este tipo de crecimiento en las propiedades ópticas, en particular el índice de refracción el cual disminuyó un 16% debido al crecimiento columnar.

List of Publications

The present work has resulted in the following publications

1. **E.A Martín-Tovar**, L.G. Daza, A.J.R. López-Arreguín, R. Castro-Rodríguez, A. Iribarren. "Effect of substrate rotation speed on the structure and properties of Al-doped ZnO thin films prepared by rf-Sputtering". *Transactions of Nonferrous Metals Society of China*, (Submitted and accepted for its publication in 2017).
2. **E.A Martín-Tovar**, R. Castro-Rodríguez, L.G. Daza, J. Méndez-Gamboa, R. Medina-Esquivel, I. Pérez-Quintana, A. Iribarren. "Structural and optical properties of ZnO thin films prepared by laser ablation using target of ZnO powder mixture with glue". *Bulletin of Materials Science* 40 (2017) 467-471
3. **E.A Martín-Tovar**, E. Chan y Díaz, M. Acosta, R. Castro-Rodríguez, A. Iribarren "N-doped ZnO films grown from hybrid target by the pulsed laser deposition technique". *Applied Physics A*, 122 (2016) 919.
4. **E.A. Martín-Tovar**, E. Denis-Alcocer, E. Chan y Díaz, R. Castro-Rodríguez, I. Iribarren. "Tuning of refractive index in Al-doped ZnO films by rf-sputtering using oblique angle deposition". *Journal of Physics D: Applied Physics*, 49 (2016) 295302.
5. **E.A. Martín-Tovar**, R. Castro-Rodríguez, I. Iribarren. "Isoelectronic CdTe-doped ZnO thin films grown by PLD". *Material Letters*, 139 (2015) 352-354.

Other publications to which the author has contributed

1. L.G. Daza, **E.A. Martín-Tovar**, R. Castro-Rodríguez, Aluminum-doped zinc oxide thin films deposited on flexible cellulose triacetate substrates prepared by RF Sputtering, *Journal of Inorganic and Organometallic Polymers and Materials*, (2017) DOI: 10.1007/s10904-017-0617-6.
2. L.G. Daza, R. Castro-Rodríguez, M. Cirerol-Carrillo, **E.A Martín-Tovar**, J. Méndez-Gamboa, R. Medina-Esquivel, I. Pérez-Quintana, A. Iribarren. "Nanocolumnar CdS thin films grown by Glancing Angle Deposition from a Sublimate Vapor Effusion source". *Journal of Applied Research and Technology*, 15 (2017) 271-277.
3. L.G. Daza, R. Castro-Rodríguez, **E.A Martín-Tovar**, A. Iribarren. "CdTe films grown using a rotating sublimate vapor effusion source in glancing angle deposition mode". *Materials Science in Semiconductor Processing*, 59 (2017) 23-28.
4. M. Acosta, I. Riech, **E. Martín-Tovar** "Effects of the Argon Pressure on the Optical Band Gap of Zinc Oxide Thin Films Grown by Nonreactive RF Sputtering". A*dvances in Condensed Matter Physics*, 2013 (2013) Article ID 970976.

Conferences

1. Effect of substrate rotation speed on the structure and properties of Al-doped ZnO thin films prepared by rf-sputtering. **E.A Martín-Tovar**, L.G. Daza, A.J.R. López-Arreguín, R. Castro-Rodríguez, A. Iribarren. XIV Simposio Sociedad Cubana de Física, 27-30 March 2017, Poster presented (Havana, Cuba).
2. Morphological engineering for modifying the optical properties of Al-doped ZnO thin films obtained by rf-sputtering with oblique angle deposition. **E.A Martín-Tovar**, E. Denis-Alcocer, E. Chan, R. Castro-Rodríguez, A. Iribarren. XIV Simposio Sociedad Cubana de Física, 27-30 March 2017, Poster presented (Havana, Cuba).
3. Isoelectronic CdTe-doped ZnO thin films grown by PLD. **Enrique Martín Tovar**, Román Castro Rodríguez, Augusto Iribarren Alfonso. VII International Conference on Surfaces, Materials and Vacuum, 6-10 October 2014, Poster presented (Ensenada, Mexico).
4. Tuning the optical band gap of zinc oxide thin films by controlling oxygen/argon ratio in radio frequency magnetron sputtering. Milenis Acosta Díaz, Inés Riech Méndez, **Enrique Martin Tovar**. VII International Conference on Surfaces, Materials and Vacuum, 6-10 October 2014, Poster presented (Ensenada, Mexico).
5. CdTe isoelectronic doping of ZnO in films grown by PLD. **E.A. Martín-Tovar**, R. Castro-Rodríguez, A. Iribarren. XXIII International Materials Research Congress, 17-21 August 2014, Poster presented (Cancun, Mexico).
6. CdTe-doped ZnO thin films grown by PLD. **E.A Martín-Tovar**, A. Iribarren, R. Castro-Rodríguez. XIII Simposio y XI Congreso de la Sociedad Cubana de Física, 17-21 March 2014, Poster presented (La Havana, Cuba).
7. ZnO thin films as a buffer and antireflective layer in glass/ITO/ZnO/CdS structures. **E.A Martín-Tovar**, R. Castro-Rodríguez. VI International Conference on Surfaces, Materials and Vacuum, 23-27 September 2013, Oral presentation (Merida, Mexico).
8. Microsocopio óptico acoplado a Webcam. **Adrián Martín-Tovar**, Eduardo Flores Cuevas, Elías Polanco Euan, Joel Tun Guerrero, Mario Perez Cortes, Mauricio Ortiz Gutierrez. LI Congreso Nacional de Física y II Congreso Latinoamericano de Física, 20-24 October 2008, Poster presented (Zacatecas Mexico).

CONTENTS

Abstract……………………………………………………………………………………………vii

Resumen……………………………………………………………………………………………ix

List of publications……………………………………………………………………………..xi

List of figures……………………………………………………………………………………xvii

List of tables……………………………………………………………………………………xxi

Chapter 1 Introduction 1

1.1 Zinc oxide: Properties and applications 1

1.1.1 Electrical properties 3

1.1.2 Optical properties 4

1.1.3 Nanostructured ZnO 4

1.2 Objectives 5

1.3 Thesis layout 6

1.4 References 7

Chapter 2 Deposition techniques background 11

2.1 Introduction 11

2.1.1 Physical vapor deposition techniques 11

2.1.2 Chemical vapor deposition 12

2.2 Pulsed laser deposition 13

2.2.1. Laser radiation interaction with the target material 14

2.2.2. Plume formation and expansion 16

2.2.3. Nucleation and growth of ablated material on the substrate's surface 17

2.2.4 Advantages of PLD 18

2.2.5. Disadvantages of PLD 19

2.2.6. PLD experimental set-up 19

2.3 Sputtering 21

2.3.1. Different types of sputtering systems 23

2.3.2. DC Sputtering 23

2.3.3. RF Sputtering 25

2.3.4. RF Magnetron Sputtering 25

2.3.5. Sputtering experimental set-up 26

2.4 References 28
Chapter 3 Characterization techniques 31
3.1 X-ray Diffraction (XRD) 31
3.2 Atomic force microscopy (AFM) 32
3.3 Thin film thickness 33
3.4 X-ray photoelectron spectroscopy (XPS) 34
3.5 Scanning Electron Microscope (SEM) 35
3.6 Optical characterization 36
3.6.1 Determination of the optical band gap 37
3.7 Electrical characterization 40
3.7.1 The Van Der Pauw technique 40
3.7.2 Hall Effect technique 41
3.8 References 42
Chapter 4 Isoelectronic co-doping of Te and Cd in ZnO 45
4.1 Isoelectronic impurities 45
4.2 Experimental details 47
4.2.1 Target preparation 47
4.2.2 Pulsed laser deposition and growth conditions 47
4.2.3 Substrate preparation 48
4.2.4 Characterization techniques 48
4.3 Results and discussions 48
4.3.1 X ray diffraction and profilometry results 48
4.3.2 Morphological analysis 49
4.3.3 Chemical studies and bonding properties 50
4.3.4 Optical analysis 53
4.4 Partial conclusions 54
4.5 References 54
Chapter 5 Nitrogen doped ZnO thin films grown from hybrid target by the laser ablation technique 57
5.1 Strategies to modify the conductivity of ZnO thin films 57
5.1.1 The problem of p-doping ZnO 57
5.1.2 Nitrogen doping of ZnO by cyanoacrylate glue using laser ablation 58

5.2 Experimental details 59
5.2.1 Target preparation 59
5.2.2 Pulsed laser deposition and growth conditions 59
5.2.3 Substrate preparation 60
5.2.4 Characterization techniques 60
5.3 Results and discussions 60
5.3.1 Structural studies 60
5.3.2 Profilometry results 63
5.3.3 Morphological analysis 63
5.3.4 Chemical studies and bonding properties 65
5.3.5 Optical and electrical analysis 67
5.4 Partial conclusions 69
5.5 References 69
Chapter 6 Effect of substrate rotation speed on the structure and properties of Al-doped ZnO thin films prepared by rf-Sputtering 75
6.1 Transparent Conductive Oxides 75
6.1.1 Optical properties 75
6.1.2 Electrical properties 77
6.1.3 Applications of TCO'S 77
6.2 Al-doped Zinc Oxide as a TCO 78
6.3 RF- Magnetron sputtering technique for the growth of Al-doped Zinc Oxide thin films 78
6.3.1 Substrate rotation in the Sputtering process 78
6.4 Experimental details 79
6.5 Results and discussions 79
6.5.1 Morphological and structural characterization 79
6.5.2 Optical characterization 87
6.5.3 Electrical characterization 88
6.6 Partial conclusions 89
6.7 References 90
Chapter 7 Tuning of refractive index in Al-doped ZnO films by rf-sputtering using oblique angle deposition 95

7.1 Introduction....95
7.1.1 Fundamentals of the Oblique Angle Deposition method....95
7.1.2 Importance of Al-doped zinc oxide as TCO....99
7.1.3 ZnO as antireflective coating....99
7.2 Growth conditions and characterization techniques.....101
7.2.1 Theoretical optical basis....102
7.3 Results and discussions....103
7.3.1 Nanocolumnar tilting angle as a function of the substrate inclination....103
7.3.2 Structural properties....104
7.3.3 Optical properties....105
7.3.4 Optical processing....107
7.3.5 Refractive index versus nanocolumnar tilt....109
7.4 Partial conclusions....111
7.5 References....111
GENERAL CONCLUSIONS....117

LIST OF FIGURES

Figure 1.1 Crystalline structures for ZnO (a) Cubic Rocksalt (b) Cubic Zincblende (c) Hexagonal wurtzite. The grey and blue spheres denote Zn and O atoms respectively. 2
Figure 1.2 Plain view (a) and cross-sectional view (b) of a ZnO film deposited on fluorine doped SnO2 on glass, which are used as a substrate for dye-sensitized solar cells 5

Figure 2.1 A representative PVD chamber. The source is vaporized, the vapor travels through the chamber to substrate, and the vapor condenses to solid phase on the substrate. 12
Figure 2.2 Schematic diagram of the experimental pulsed laser deposition setup. A laser ablates target material, resulting in the evaporation thereof towards a substrate under a vacuum environment. 14
Figure 2.3 Basic thermal cycle induced by a laser pulse (a) Fusion begins, (b) Propagation of the fusion front, (c) Retreat of the fusion process, (d) Complete solidification. 16
Figure 2.4 Schematic diagrams of the atomic processes in the nucleation of three-dimensional clusters on the surface of a substrate 18
Figure 2.5 Schematics of the PLD deposition system employed for the realization of this thesis 20
Figure 2.6 Photograph of the Nd: YAG laser employed in this work. 20
Figure 2.7 Substrate holder and heating system 21
Figure 2.8 A general outline of the sputtering process. 22
Figure 2.9 Schematic diagram of a DC sputtering setup. 24
Figure 2.10 Schematic diagram of a magnetron sputtering process 26
Figure 2.11 Rf-magnetron sputtering employed in this work (a) front view (b) top view 27

Figure 3.1 Schematic of the X-ray diffraction phenomenon. 31
Figure 3.2 Schematic of the X-ray diffractometer 32
Figure 3.3 Schematic of an AFM device 33
Figure 3.4 Schematic of the thickness measurement carried out by a profilometer 34
Figure 3.5 A Scheme of X- ray photoelectron spectroscopy process 34
Figure 3.6 Schematic diagram of a Scanning Electron Microscope (SEM) General Setup. 36
Figure 3.7 Schematic diagram of the optical transmission in a thin film. 37
Figure 3.8 Scheme of a (a) direct and (b) indirect transition in a material. 39
Figure 3.9 Two possible set-ups for the contacts on the Van der Pauw technique. 40
Figure 3.10 The eight possible configurations to measure the resistivity. 41

Figure 4.1 A two-dimensional schematic representation of a ZnO crystal, a) with perfect stoichiometry, and b) with an oxygen vacancy. 46
Figure 4.2 Diffractograms of the CdTe-doped (upper) and undoped ZnO (lower) thin films, respectively. The blue lines correspond to the standard pattern peaks. 49

Figure 4.3 2D (a) 2D AFM image (b) 2D AFM phase image and (c) 3D AFM image of the CdTe-doped ZnO film....50
Figure 4.4 EDS results of the CdTe-doped ZnO thin films....51
Figure 4.5 XPS survey spectrum of the CdTe doped ZnO thin films....51
Figure 4. 6 XPS spectrum of the CdTe doped ZnO thin films. Binding energy spectrum of (a) Zn 2p, (b) O 1s, (c) Te $4d_{5/2}$ and 3d (d)....52
Figure 4.7 Optical transmittance spectra of the CdTe-doped ZnO thin films....53
Figure 4.8 $(\alpha h\nu)^2$ vs. $h\nu$ curves of the CdTe-doped ZnO thin films....54

Figure 5.1 Chemical structure of the Ethyl 2- Cyanoacrylate....59
Figure 5.2 Diffractograms of the films grown from the hybrid (upper) and sintered (lower) targets, respectively. Dashed lines correspond to the standard pattern peaks....61
Figure 5.3 Surface (a) and cross-sectional (b) images of the HT film....64
Figure 5.4 3D AFM images of the ZnO HT (a) and ST (b) films....64
Figure 5.5 (a) 2D AFM images for the HT ZnO thin film (b) 2D AFM image for the ST ZnO thin film 65
Figure 5.6 XPS spectra of HT films: (a) wide scan and high resolution spectra of the (b) O 1s; (c) Zn 2p; and (d) Zn Auger L3M4,5M4,5 regions....66
Figure 5.7 Tauc plot of $(\alpha h\nu)^2$ vs. $h\nu$ calculated from the transmission spectra....67
Figure 5.8 Linear approximation of the Zn3N2 and ZnO (a) band gaps and (b) CBM and VBM in a (Zn3N2)r-(ZnO)s pseudobinary alloy....68

Figure 6.1 Interactions of light photons within a TCO material....76
Figure 6. 2 Transmission, reflection, and absorption spectra of a typical TCO....76
Figure 6.3 Cross-sectional FESEM image of AZO thins films on glass substrate grown at ω_s of (a) 0, (b) 150, (c) 230, (d) 350 and (e) 475 rpm respectively....80
Figure 6.4 AFM images of the AZO thin films with at different ω_s of a) 0, b) 150, c) 230, d) 350 and e) 475 rpm respectively....82
Figure 6.5 Number of hills (Nh) and first neighbor distances (FND) at different substrate velocities. 84
Figure 6.6 XRD patterns of AZO thin films prepared at different rotation velocities....85
Figure 6.7 Position of the (002) peak and FWHM values at different substrate speed....87
Figure 6.8 Optical transmittance spectra of AZO thin films....88
Figure 6.9 Electrical properties of AZO thin films deposited at different substrate rotation velocities. 89

Figure 7.1 Schematic of an OAD setup....96
Figure 7.2 OAD growth mechanisms schematically represented [9] (a) Initial arrival of the vapor flux to the substrate in an oblique angle (b) Nuclei centers growth by shadowing effect (c) Columnar growth (d) Columnar extinction by shadowing effect....97

Figure 7.3 Archetypal OAD fabricated nanostructures, (a) slanted columns, (b) zigzag columns, (c) helical columns, (d) vertical columns and (d) graded-density columns. 98
Figure 7.4 Interference process of light in a (a) ARC material and (b) non ARC material. 100
Figure 7.5 SEM image of AZO films without tilting (above), θ = 75° tilted (below left) substrate holder and surface SEM image of θ = 75° tilted (below right). 104
Figure 7.6 Nanocolumnar tilt angle dependence of substrate holder inclination. 104
Figure 7.7 Diffractograms of AZO films as a function of the substrate inclination. Dashed lines correspond to the ZnO pattern diffractogram lines. 105
Figure 7.8 Optical transmittance spectra of the AZO thin films deposited at different tilting angles. 106
Figure 7.9 Tauc plot of AZO thin film growth at different tilting angles. 106
Figure 7. 10 Plot of experimental transmission (solid line) and Tf (dashed line) of the sample grown at θ = 75°. The inset shows the exponential fitting applied in the plot of $(\alpha h\nu)^2$ as a function of hν where the dashed line corresponds to the fitted tail. 108
Figure 7.11 Behavior of the refractive index as a function of the wavelength for different substrate holder tilts. 109
Figure 7.12 Effective refractive index at λ ≈ 700 nm dependence on columnar tilting angle. 109
Figure 7. 13 Scheme of the disordered area (shadowed region in the projection) that the light cuts across in vertical (left) and slanted (right) nanocolumns at normal incidence. 110
Figure 7.14 (a) Scheme of a suggested multilayer changing the nanocolumn tilt angle. Yellow bars proportionally illustrate the values of refractive index for each layer. (b) SEM image of an experimentally obtained multilayer with continuous variation of the nanocolumn tilt angle 14.7° to 0° with respect to the normal at the substrate. 111

LIST OF TABLES

Table 1.1 Some physical properties of the ZnO.......... 3

Table 5.1 Structural parameters obtained from diffractograms. 62

Table 5.2 Comparison of the relative peak intensity of pattern, Hybrid Target (HT) thin film and Sintered Target (ST) thin film.......... 63

Table 6.1 Characteristics of the samples estimated from AFM and XRD data.......... 87

Chapter 1 Introduction

This thesis outlines the work done in controlling the growth and doping of zinc oxide (ZnO) thin films and nanostructures via the pulsed laser deposition (PLD) and RF-magnetron sputtering techniques, being the main focus obtaining samples with potential applications as antireflective layers and transparent conductive oxides. The deposition of thin films by the PLD technique was developed in the mid-1960s, but it did not become a mainstream deposition method until 1987 when it was found that it was capable of depositing high temperature superconductors such as $YBa_2Cu_3O_7$ [1]. The thin films of the aforesaid material obtained by this technique were of a higher quality than from any other technique that had previously overshadowed the pulsed laser deposition. Thereafter, PLD became one the most important techniques for the production of high-quality thin films, the further development of more advanced lasers with shorter pulse widths has been instrumental in the solidification of the PLD as wide accepted technique. The other technique employed for the development of this thesis was the RF-sputtering deposition method, which is placed in high regard among many other techniques due to its versatility, efficiency, simplicity and high reproducibility at industrial level, these characteristics allow depositing thin films with fine-tuned properties over large areas in a wide variety of substrate materials.

The material used throughout this work was zinc oxide. ZnO is well known for its medical properties and its great variety of applications, such as: paints, additive for rubber and plastics, catalysts, lotions, skin ointments and powders, additionally it is generally the main component of sun screen lotions. ZnO has a major importance in the materials science field, and has raised an extensive interest in fundamental and applied research, more so when it is in its nanostructured form, where it exhibits an abundant configurations of nanostructures[2]; this is due to its remarkable physical properties which make it a promising material for a large number of optoelectronic applications, namely; UV light-emitters, varistors, transparent high power electronics, surface acoustic wave devices, piezoelectric transducers, gas-sensing and as a window material for display and solar cells [3]. This research spans different deposition conditions and growth techniques, sol-gel, spray-pyrolysis, atomic layer deposition, molecular beam epitaxy, and the ones concerning this thesis, PLD and sputtering. In the following chapter the basic properties concerning zinc oxide are explained, its electrical, optical, morphological and structural properties are described, as well as its most important and common applications as bulk, thin film and nanostructured material. Finally the layout of the thesis will be given in full detail.

1.1 Zinc oxide: Properties and applications

Zinc oxide is an inorganic white colored compound which is naturally found in the zincite mineral, this mineral crystalizes in the hexagonal wurtzite $P6_{3mrc}$ [4]. ZnO is called II-VI semiconductor because the zinc and the oxygen belong to the group II and VI of the periodic table, respectively. Zinc oxide crystallizes in three different phases: Hexagonal wurtzite, cubic zincblende and in a cubic rocksalt (NaCl) phase. The Zinc blende ZnO can be formed as a metastable phase by means of epitaxial growth on cubic substrates [5, 6], while the rocksalt phase is obtainable by compressing the ZnO wurtzite structure

upon pressures up to the order of 9.8 GPa [7]. So the hexagonal wurtzite structure is the most stable and common phase found in nature; its lattice parameters are *a* = 0.325 nm and *c* = 0.52066 nm [8]; their coordination is such that zinc atoms are surrounded by the oxygen atoms in an almost tetragonal arrangement, being its coordination number four, this means that each atom has 4 neighboring atoms in its closest environment. The crystalline structures mentioned before are illustrated in Figure 1.1.

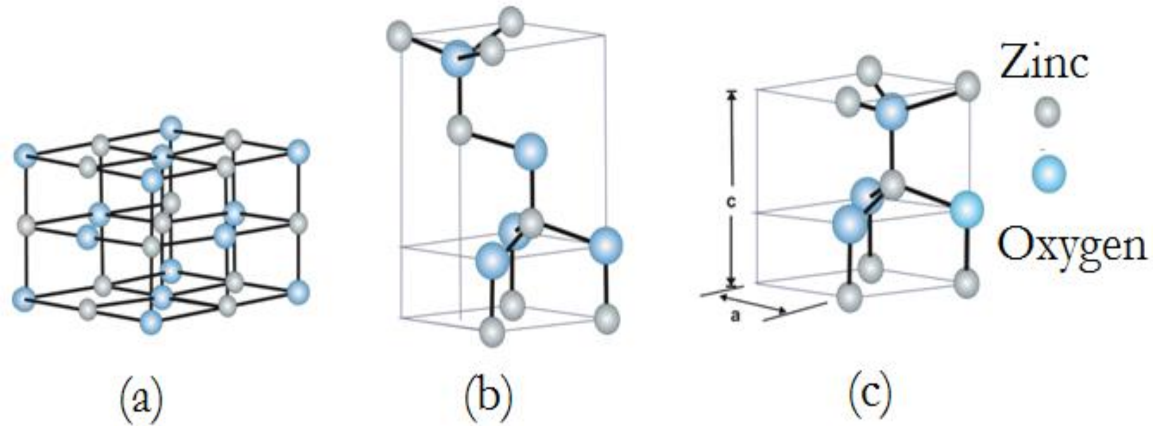

Figure 1.1 Crystalline structure for ZnO (a) Cubic Rocksalt (b) Cubic Zincblende (c) Hexagonal wurtzite. The grey and blue spheres denote Zn and O atoms respectively [9].

Zinc oxide is a semiconductor material that has been investigated since 1912. The invention of the transistor began the semiconductors era, which led to the rise in investigation of the ZnO as semiconductor compound. Decades later the discovery of its excellent piezoelectric properties led to its first application in electronics as thin layer in surface acoustic wave devices (SAW) [10]. It has a variety of structural and optoelectronic properties and it's because of them that it is used in various technological fields, to name a few: Ultraviolet lasers (UV) and electronic short wavelength devices [11, 12]. It could also be used in photoconductors [13], gas sensors [14], and in solar cell applications [15]. Its high crystalline preferential orientation along the *c*-axis and its wide band gap energy, which is a direct band gap of 3.37 eV are useful properties in acoustic surface and in acoustic-optic devices [16].

All the properties mentioned before make ZnO a promising material to replace the materials traditionally used in various applications, for example, many ZnO based alloys could become an alternative to materials based gallium nitride (GaN), which is currently used in UV devices. Both GaN and ZnO have a similar band gap value, but ZnO has an exciton binding of more than twice of that of GaN, which is close to 18 to 28 meV, this is an advantage because it allows producing exciton emissions above the threshold of room temperature, something that does not occur in GaN [17]. However, ZnO has a prevalent *n*-type conductivity caused by oxygen vacancies and zinc interstitials, so reproducible *p*-type conductivity with good quality is hard to attain. This is a major limitation for many optoelectronic applications given that the fabrication of *p*-*n* junctions is mandatory in such devices [18]. Some of the properties of the ZnO are enlisted in Table 1.1.

Table 1.1 Some physical properties of the ZnO [19].

Parameter	Symbol (units)	Value for ZnO
Melting point	T_M (K)	2248
Space group		$P6_{3mrc}$
Crystal structure		Hexagonal Wurtzite
Coordination geometry		Tetrahedral
Lattice constants	*a* , *c* (nm)	0.32495, 0.52069
Heat capacity	C_p (Cal/ mol K)	9.6
Density	ρ (g/cm^3)	5.506
Thermal conductivity	λ (W/cm K)	0.6
Refractive index	n	2.029
Band gap energy	E_g (eV)	3.37
Exciton binding energy	(meV)	60
Electron effective mass		0.24
Hole effective mass		0.59

1.1.1 Electrical properties

Most semiconductor oxide materials possess an insulating behavior in their stoichiometry form, deviations from latter result in a rise in their electrical conductivity; however, as it was mentioned before most of them have *n*-type conductivity due to the presence of oxygen vacancies. Thus, it is expected that the amount of oxygen in ZnO crystals will determine the electrical carrier concentration of electrical carriers and therefore their conductivity value, this is caused by the balance reaction between the oxygen vacancies or the interstitials zinc atoms and conduction band electrons. The behavior of the ZnO as an *n*-type semiconductor is due to deviations in its stoichiometry, this means that the intrinsic defects in the ZnO act as dopants. There are two kinds of these defects oxygen vacancies and interstitial zinc atoms, and depending on the growth conditions for the material, one of them will be dominant [8].

In all semiconductors there are two types or charge carriers, one of them are electrons, the other type are the mobile vacancies left on the valence band by the electrons as a result of doping process, these are called "holes" and they possess a positive charge, which is of the opposite value to that of the electrons. In semiconductor materials there is a good chance that an electron-hole pair could be created by

the aforementioned structural defects, this is known as "exciton". These excitons can be observed by optical photoluminescence measurements.

The electrical resistivity (ρ) in ZnO thin films is determined by both their electrical carrier concentration n_e and mobility (μ), this relationship is given by the following expression:

$$\rho = \frac{1}{\mu e n_e} \quad (1.1)$$

Where e is the fundamental electric charge, consequently increasing both carrier concentration and mobility will result in lower resistivity; most research suggests that this achieved through the formation of oxygen vacancies and doping [20]. Quantifying the electrical properties of ZnO has proven to be difficult a task; this is due to large variety of quality and properties of the available samples. Depending on the quality of the layers, the background carrier concentration varies a lot, but it is usually $\sim 10^{16}$ cm^{-3}. The largest n and p type doping reported has been $\sim 10^{20}$ cm^{-3} and $\sim 10^{19}$ cm^{-3} respectively, however the quality and reproducibility of such p-type doping has been questioned and it is still subject of debate [21]. The corresponding electron Hall mobility at 300K for low n-type conductivity is $\mu = 200$ $cm^2 V^{-1} s^{-1}$, and for low p-type conductivity is 5–50 $cm^2 V^{-1} s^{-1}$ [3].

1.1.2 Optical properties

The intrinsic and extrinsic defects determine the optical properties in any semiconductor material, such as ZnO. The optical properties and processes in ZnO as well as its refractive index were extensively studied many decades ago [22]. A renewed interest in ZnO has risen due its potential applications as an optoelectronic material, owing this to some of its remarkable properties, such as its direct wide band gap (3.37 eV) and its large exciton binding energy (60 meV). This strong binding energy ensures an efficient exciton emission at room temperatures under low excitation energy, which makes it promising candidate as photonic material in the blue UV region.

Much of the research on the optical properties for bulk and nanostructured ZnO has been carried out by luminescence techniques at low temperatures, e.g. in the work published by B. K. Meyer et al [23], an extensive analysis and investigation was made of the excitonic spectra obtained from ZnO, which assigned many defect related spectra features, and donor-acceptor pair emissions as well. A broad defect related peak that ranges from ~ 1.9 to 2.8 eV is a frequent optical feature of ZnO. This defect is known as "green band", and the origin of its luminescence is still not well understood, defects and impurities are often employed to explain it. Other fundamental optical quantities of ZnO, such as refractive index have been extensively studied, being its value for the wurtzite ZnO equal to n =2.029 [3].

1.1.3 Nanostructured ZnO

One of the most recent breakthroughs in material science was the emergence of nanotechnology. Due to its wide range of possible applications (such nanomedicine, nanoelectronics, biomaterials energy production, and consumer products) it has led to an enthusiastic research interest for obtaining new materials is nanostructured form, i.e., with their dimensions reduced to a nanometric scale, this is due to

the fact that when a material reaches these dimensions it presents new and interesting electrical, mechanical, optical and chemical properties that differ from its source material, and ZnO is included in the list of materials that are among them.

There are a large number of ZnO nanostructures that are attainable through many growth and deposition techniques, such as: nanotubes [24] nanowires [25], nanorods [26], nanobelts [27], nanocables [28] and nanoribbons [29]. Many of the aforementioned nanostructures generated a great interest in their scientific research due to their great importance and their potential technological applications, which include UV lasers [30], chemical sensors [31], or transparent substrates for thin film solar cells, e.g. as an alternative to TiO_2 in injection type solar cells or in organic solar cells [32, 33, 34]. One the most recent and interesting applications of ZnO nanowires was reported by Wang et al [35]. They reported that by combining ZnO nanowires with a zig-zag metal electrode, a device called "nanowire nanogenerator" capable of producing continuous direct-current output driven by ultrasonic waves was fabricated. In the aforesaid work the authors took advantage of the piezoelectric properties of ZnO, using to extract a voltage due to mechanical bending of the nanowire. Figure 1.2 shows scanning electron micrographs of an array of ZnO nanowires grown on a magnetron-sputtered ZnO film on a fluorine-doped SnO_2 covered glass substrate.

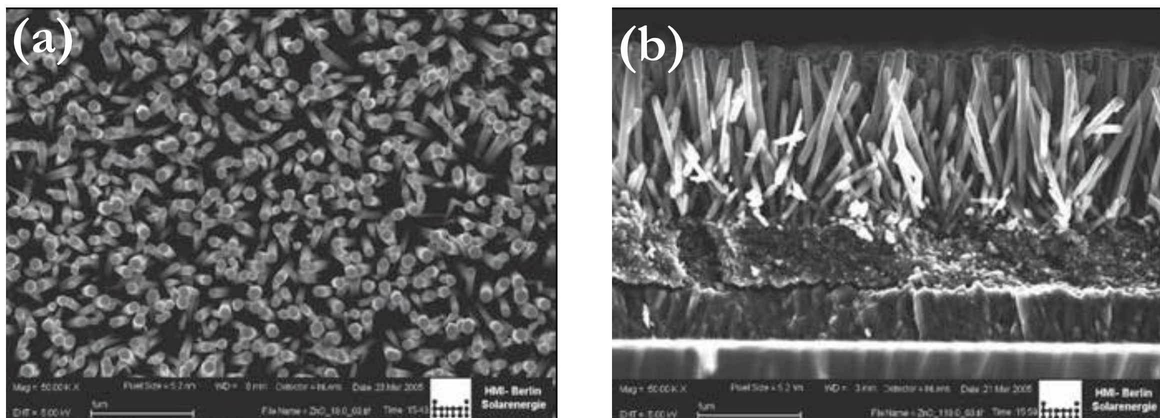

Figure 1.2 Plain view (a) and cross-sectional view (b) of a ZnO film deposited on fluorine doped SnO_2 on glass, which are used as a substrate for dye-sensitized solar cells [8].

1.2 Objectives

The main objective of the present thesis is to fabricate doped and undoped ZnO thin films and nanostructured samples from different types of targets, employing the pulsed laser deposition (PLD) and RF-magnetron sputtering techniques, in order to obtain samples with the suitable properties for their future applications as antireflective layers and transparent conductive oxides. The specific objectives were to:

- Study the effect of the isoelectronic doping of ZnO by CdTe on the morphological, optical, structural and chemical properties of thin films deposited by PLD.
- Study the effect of nitrogen doping ZnO from a cyanoacrylate glue target on the morphological, optical, structural and chemical properties of thin films deposited by PLD.

- Compare the properties of the ZnO thin films fabricated with the cyanoacrylate glue target to those grown from a standard pure ZnO target, for its future applications as antireflective layer.
- Study the effect of substrate rotation speed on the morphological, structural, optical and electrical of properties of Al-doped ZnO (AZO) nanostructured thin films deposited by RF-magnetron sputtering.
- Employ the oblique angle deposition (OAD) method to grow nanostructured Al-doped ZnO thin films.
- Study the effect of the oblique substrate angle on the morphological, structural and optical properties of Al-doped ZnO (AZO) nanostructured thin films deposited by RF-magnetron sputtering.

1.3 Thesis layout

The thesis itself is divided into seven chapters. The following is a brief description of the contents for each chapter.

Chapter One:

The basic concepts, history, importance and properties of ZnO are presented briefly. Additionally, the objectives of the thesis are established.

Chapter two:

The theoretical background of the pulsed laser deposition and sputtering techniques is presented, its importance and applications is briefly described as well.

Chapter three:

The experimental techniques used to study the structural, morphological, optical, electrical and chemical properties; of the deposited ZnO thin films are described and summarized.

Chapter four:

Presents all of the data results, analysis and conclusions of the study of CdTe isoelectronic ZnO thin films grown by the pulsed laser deposition technique.

Chapter five:

Presents all of the data results, analysis and conclusions of the work done depositing nitrogen doped ZnO thin films from both a pure and hybrid cyanoacrylate targets by the PLD technique.

Chapter six:

The data results, analysis and conclusions for the study carried out on the effects of substrate rotation on deposited AZO thin films grown by RF-sputtering.

Chapter seven

The data results, analysis and conclusions for the study carried out on the AZO thin films obtained by the oblique angle deposition method are presented in this chapter.

1.4 References

[1] D. Dijkkamp, T. Venkatesan, X. D. Wu, S. A. Shareen, N. Jiswari, Y. H. Min-Lee, W. L. McLean, and M. Croft, Preparation of Y-Ba-Cu Oxide Superconductor Thin Films Using Pulsed Laser Evaporation from high Tc Bulk Materials, Applied Physics Letters 51 (1987) 619-621.

[2] Zhong Lin Wang, ZnO nanowire and nanobelt platform for nanotechnology, Materials Science and Engineering R 64 (2009) 33–71.

[3] S.J. Pearton, D.P. Norton, K. Ip, Y.W. Heo, T. Steiner, Recent progress in processing and properties of ZnO, Progress in Materials Science 50 (2005) 293–340.

[4] R.G.W. Wyckoff, Crystal Structures, Interscience, New York, 1963.

[5]Ü. Özgür, Ya. I. Alivov, C. Liu, A. Teke, M. A. Reshchikov, S. Doğan, V. Avrutin, S.-J. Cho, and H. Morkoç, A comprehensive review of ZnO materials and devices, Journal of Applied Physics 98 (2005) 041031.

[6] A. B. M. Almamun Ashrafi, Akio Ueta, Adrian Avramescu, Hidekazu Kumano, Ikuo Suemune, Young-Woo Ok, and Tae-Yeon Seong, Growth and characterizacion of hypothetical zinc-blende films on GaAs (001) substrates with ZnS buffer layers, Applied Physics Letters 76 (2000) 550-552.

[7] Haozhe Liu, John S. Tse and Ho-kwang Mao, Stability of rocksalt phase of zinc oxide under strong compression: Synchrotron x-ray diffraction experiments and first-principles calculation studies, Journal of Applied Physics 100 (2006) 093509.

[8] K. Ellmer , A. Klein., Transparent Conductive Zinc Oxide Basics and Applications in Thin Film Solar Cells, Springer, Berlin Heidelberg New York, 2008.

[9] Luis German Daza Casiano, Películas delgadas de óxido de zinc dopadas con aluminio (AZO) sobre substratos flexibles obtenidas por RF sputtering no reactivo, Master's Thesis, Centro de Investigación y de Estudios Avanzados del Instituto Politécnico Nacional Unidad Mérida, 2014.

[10] X.Y. Du , Y.Q. Fu , S.C. Tan , J.K. Luo, A.J. Flewitt , S. Maeng , S.H. Kim , Y.J. Choi , D.S. Lee , N. M. Park , J. Park , W.I. Milne, ZnO film for application in surface acoustic wave device, Journal of Physics: Conference Series 76 (2007) 012035.

[11] S.B. Majumder, M. Jain, P.S. Dobal, R.S. Katiyar, Investigations on solution derived aluminium doped zinc oxide thin films, Materials Science and Engineering B103 (2003) 16-25.

[12] T. Ratanaa, P. Amornpitoksukb, T. Ratanac, S. Suwanboon, The wide band gap of highly oriented nanocrystalline Al doped ZnO thin films from sol–gel dip coating, Journal of Alloys and Compounds 470 (2009) 408–412.

[13] Liqiao Qin, Christopher Shing, Shayla Sawyer, Partha S. Dutta, Enhanced ultraviolet sensitivity of zinc oxide nanoparticle photoconductors by surface passivation, Optical Materials 33 (2011) 359–362.

[14] S.I. Boyadjiev, V. Georgieva, R. Yordanov, Z. Raicheva, I.M. Szilágyi, Preparation and characterization of ALD deposited ZnO thin films studied for gas sensors, Applied Surface Science 387 (2016) 1230–1235.

[15] Chih-Hao Liang, Yu-Jen Hsiao, Weng-Sing Hwang, Comparative study of structural and electro-optical properties of ZnO:Ga films grown by steered cathodic arc plasma evaporation and sputtering on plastic and their application on polymer-based organic solar cells, Thin Solid Films 612 (2016) 419–429.
[16] Z. Banu Bahşi, A. Yavuz Oral, Effects of Mn and Cu doping on the microstructures and optical properties of sol–gel derived ZnO thin films, Optical Materials 29 (2007) 672–678.
[17] Madelung, U Rössler, M Schulz, Semiconductors ·Group IV Elements, IV-IV and III-V Compounds. Part b - Electronic, Transport, Optical and Other Properties, Springer, Verlag Berlin Heidelberg, 2002.
[18] Chao Wang, Zhenguo Ji, Junhua Xi, Juan Du, Zhizhen Ye, Fabrication and characteristics of the low-resistive p-type ZnO thin films by DC reactive magnetron sputtering, Material Letters 60 (2006) 912-914.
[19] Coleman V., Jagadish C., Look D., Zinc Oxide Bulk, Thin Films and Nanostructures; Processing, Properties and Applications, Elsevier, Oxford, 2006.
[20] Robert Eason. Pulsed Laser deposition of thin films applications-LED growth of functional materials. John Wiley & Sons, Inc. Hoboken, New Jersey, 2007.
[21] D. C. Look, B. Claflin,Ya. I. Alivov, S. J. Park, The future of ZnO light emitters, Physica Status Solidi A 201 (2004) 2203-2212.
[22] D.G. Thomas, The exciton spectrum of zinc oxide, Journal of Physics and Chemistry of Solids 15 (1960) 86-96.
[23] B. K. Meyer, H. Alves, D. M. Hofmann, W. Kriegseis, D. Forster, F. Bertram, J. Christen, A. Hoffmann, M. Straßburg, M. Dworzak, U. Haboeck, A. V. Rodina, Bound exciton and donor–acceptor pair recombinations in ZnO, Physica Status Solid B 241 (2004) 231-260.
[24] Sungkwon Cho, Dai-Hong Kim, Byoung-Sun Lee, Joohyun Jung, Woong-Ryeol Yu, Seong-Hyeon Hong, Seonghoon Lee, Ethanol sensors based on ZnO nanotubes with controllable wall thickness via atomic layer deposition, an O_2 plasma process and an annealing process, Sensors and Actuators B 162 (2012) 300–306.
[25] Jingbiao Cui, Zinc oxide nanowires, Materials Characterization 64 (2012) 43 – 52.
[26] Rajneesh Mohan, Karthikeyan Krishnamoorthy, Sang-Jae Kim, Enhanced photocatalytic activity of Cu-doped ZnO nanorods, Solid State Communications 152 (2012) 375–380.
[27] K. Momeni, Gregory M. Odegard, Reza S. Yassar, Finite size effect on the piezoelectric properties of ZnO nanobelts: A molecular dynamics approach, Acta Materialia 60 (2012) 5117–5124.
[28] Jianping Deng, Minqiang Wang, Jing Liu, Xiaohui Song, Zhi Yang, Arrays of ZnO/AZO (Al-doped ZnO) nanocables: A higher open circuit voltage and remarkable improvement of efficiency for CdS-sensitized solar cells, Journal of Colloid and Interface Science 418 (2014) 277–282.
[29] Teng Ma, Yong Wang, Rui Tang, Hongyu Yu, Hanqing Jiang, Pre-patterned ZnO nanoribbons on soft substrates for stretchable energy harvesting applications, Journal of Applied Physics 113 (2013) 204503.
[30] Michael H. Huang, Samuel Mao, Henning Feick, Haoquan Yan, Yiying Wu, Hannes Kind, Eicke Weber, Richard Russo, Peidong Yang, Room-Temperature Ultraviolet Nanowire Nanolasers, Science 292 (2001) 1897-1899.

[31] Davide Barreca, Daniela Bekermann, Elisabetta Comini, Anjana Devi, Roland A. Fischer, Alberto Gasparotto, Chiara Maccato, Giorgio Sberveglieri, Eugenio Tondello, 1D ZnO nano-assemblies by Plasma-CVD as chemical sensors for flammable and toxic gases, Sensors and Actuators B 149 (2010) 1–7.
[32] Julian Tornow, Klaus Schwarzburg, Transient Electrical Response of Dye-Sensitized ZnO Nanorod Solar Cells, Journal of Physical Chemistry C 111 (2007) 8692–8698.
[33] T. Soga, Nanostructured Materials for Solar Energy Conversion, Elsevier, Oxford, 2006.
[34] M.S. White, D.C. Olson, S.E. Shaheen, N. Kopidakis, D.S. Ginley, Inverted bulk-heterojunction organic photovoltaic device using a solution-derived ZnO underlayer ,Applied Physics Letters 89 (2006) 143517.
[35] X. Wang, J. Song, J. Liu, Z.L. Wang, Direct-Current Nanogenerator Driven by Ultrasonic Waves Science 316 (2007) 102-105.

Chapter 2 Deposition techniques background

2.1 Introduction

Nowadays solid state physics aims to obtain materials with properties suitable for their use in devices whose applications include areas as diverse as biophysics, optoelectronics and nanotechnology [1]. The size of these devices has diminished over time as well as the dimensions of the materials that constitute them, even reaching microscopic sizes. This is why it is essential to study the process that allows them to be obtained, including its deposition as thin films. Materials science has an important application in the renewable energies sector, specifically in the field of solar cells; in the aforementioned field there is a great variety of materials that require thin films of a few micrometers of thickness in order to properly absorb the sunlight and transform it in usable energy.

When one of the dimensions in a material is much smaller than the others, it could be called a "thin film" [2]. Devices bases on thin films have typical dimensions of about 5 to 50 μm whereas bulk devices have thicknesses of about 50 to 250 μm [3]. There are a great variety of techniques that are used to deposit thins films, and each one has an important role in the resulting properties and microstructure that will be present in the obtained films, so choosing the appropriate deposition technique is of major importance for many technological applications. For example the microstructural features of the absorber layer sensitively influence the photovoltaic performance in a solar cell and in some cases, specific microstructures may be necessary to obtain the desired performance, and such specific microstructures might only be obtained by a specific deposition technique with the right deposition conditions. Many of the final properties in a thin film are dependent on the deposition conditions in which it was obtained, e.g., background pressure, substrate temperature, the type of substrate, the rate of deposition, among others, consequently by varying such conditions during the growth of the film it is possible to obtain a wide variety of properties in the resulting thin films. The desired application for which a given material will be employed determines the most suitable technique for the preparation of thin films of that material, so selecting the right deposition technique and conditions is crucial.

Two deposition techniques were mainly employed to obtain all the thin films which were studied for the development of this thesis, namely, radio-frequency magnetron sputtering (RF sputtering) and pulsed laser deposition (PLD). The RF sputtering technique was employed for the deposition of the Al doped zinc oxide thin films, while the pulsed laser deposition technique was used to deposit pure ZnO thin films along with ZnO doped with CdTe and nitrogen. The optical, morphological, electrical, chemical and structural properties of the obtained films were studied using different characterization tools. In this chapter, the theoretical background for both of the previously mentioned techniques will be discussed.

2.1.1 Physical vapor deposition techniques

The deposition techniques in which the main physical processes involved are erosion and evaporation are called physical vapor deposition methods (PVD). In a PVD process a source material (metal, metal oxide or even polymer) is vaporized under vacuum and free vapor phase atoms travel throughout the vacuum enclosure to create a thin film, this basic principle is shown in Figure 2.1.

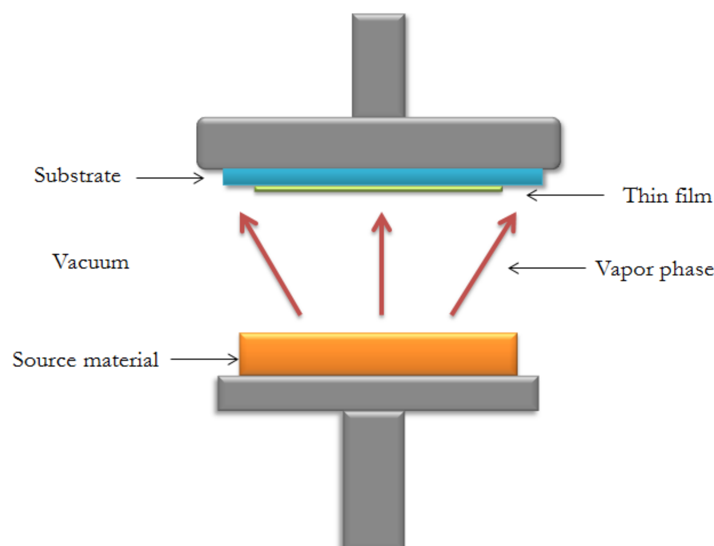

Figure 2.1 A representative PVD chamber. The source is vaporized, the vapor travels through the chamber to substrate, and the vapor condenses to solid phase on the substrate.

1. Generation of species to be deposited, i.e., the transition of condensed phases in form of solids or liquids to vapor-gas phases.
2. Transport of the source species to the substrate.
3. Growth of the film in the substrate. The processes that occur in the substrate depend on the energy of the incident particles and the temperature of the substrate.

Vacuum systems are commonly used in these techniques to prevent contamination or the incorporation of undesirable agents into the films [4]. The use of vacuum plays a major role in the deposition of thin films because it allows the production of high purity films required in many technological applications.

2.1.2 Chemical vapor deposition

In these techniques, chemical reactions take place in growth process of thin films; these reactions are carried out using a precursor material from which the material that is desired to be deposited is formed. In the simplest CVD process, a precursor gas flows into a deposition chamber where one or more heated objects to be coated are contained. In the aforesaid chamber chemical reactions occur on and near the hot surfaces, resulting in the deposition of a thin film on the substrate material. Non-desired by-products are also produced, which are removed from the deposition chamber by a gas flow. Among the most commonly used CVD techniques are: Metal organic CVD (MOCVD), atmospheric pressure CVD (APCVD), low pressure CVD (LPCVD), ultrahigh vacuum CVD (UHCVD), aerosol assisted CVD (AACVD), direct liquid injection CVD (DLICVD), etc. Usually in these techniques the precursor material is reacted with the substrate, so that three main phases can occur in the process:

1. Formation of the material before contact with the substrate, so when it arrives to thereof, only the film is deposited and grows.

2. The material is not completely formed and upon reaching the substrate, depending on the conditions thereof, ends up forming and accumulating in such a way that the film grows.

3. The reactive material depends on both the conditions of the surface, the substrate and their characteristics.

The chemical deposition processes are very complex and can often occur several of the phases mentioned above mentioned in a single deposition process [4]. The following sections will focused on the theoretical background and experimental set-ups specifically for the sputtering and PLD techniques.

2.2 Pulsed laser deposition

The pulsed laser deposition (also known as "laser ablation") technique is a physical vapor deposition process which takes place in a vacuum system. In this technique a laser erodes a solid material referred to as "target" which is desired to be deposited onto a substrate; this is accomplished through the absorption of the energy emitted by each pulse emanated by a laser source, thus reaching the ablation threshold for the aforesaid material. The laser pulses employed in an ablation process are of a high power, reaching energy densities of 10^8 W/cm^2, this energy is used to melt, ionize and excite the target material. This process produces a plume of transient and highly luminous plasma which expands rapidly away from the target. Afterwards the eroded material is deposited on the substrate's surface in which it condenses and the film nucleates and grows [5, 6]. The plasma expands and deposits on a substrate in an atmosphere under vacuum or in a reactive medium.

The ejected material is composed of ions, atoms and molecules that will be eventually arranged in one or more crystallographic orientations when they reach the substrate's surface. This deposition technique was initially used to fabricate thin films with complex stoichiometry and was subsequently used in the growth of nanostructures. Laser ablation is the most widespread method for deposition of thin films of ceramic superconductors, such as $YBa_2Cu_3O_{7-x}$ (YBCO or 1-2-3) and was the first technique to get a successful deposition as a thin film thereof [7, 8]. Since then, many thin films from materials with complicate compositions have been successfully grown by PLD

The first laser ablation demonstrations were carried out by Smith and Turner in 1965 and they were made afterwards the development of the ruby lasers [9]. The technique remained unpopular for many years, due to the fact that deposited films were inferior to those obtained by other techniques such as chemical vapor deposition and molecular beam epitaxy. It was not until the development of lasers with sufficiently energetic pulses and short durations favored the acceptance of PLD as a deposition technique, i.e., gas lasers with high-power thyratron switches or Q-switched solid state lasers [10], being the major breakthrough for this technique the successful deposition of the high temperature superconductor material $YBa_2Cu_3O_{7-x}$ by Dijkkamp et al. [8], which resulted in thin films of superior quality than those deposited with alternative techniques.

From an experimental point of view, the laser ablation technique is relatively simple, as shown in Figure 2.2. The simplest PLD experimental configuration consists of a substrate and target holders. A high-intensity beam from the laser is focused and shot on the target, thus vaporizing it; subsequently the evaporated material is deposited on the substrate. Usually the process is carried out in a vacuum

environment and prior to the deposition the chamber is evacuated to pressures ranges of 10^{-6} to 10^{-4} Torr. Shooting the target in the same spot must be avoided, since it would eventually degrade its surface and would lead to the end of the ablation process. To avoid this, it is necessary to rotate the target holder, thus the ablation occurs successively at different points leading to a homogenous consumption of the target.

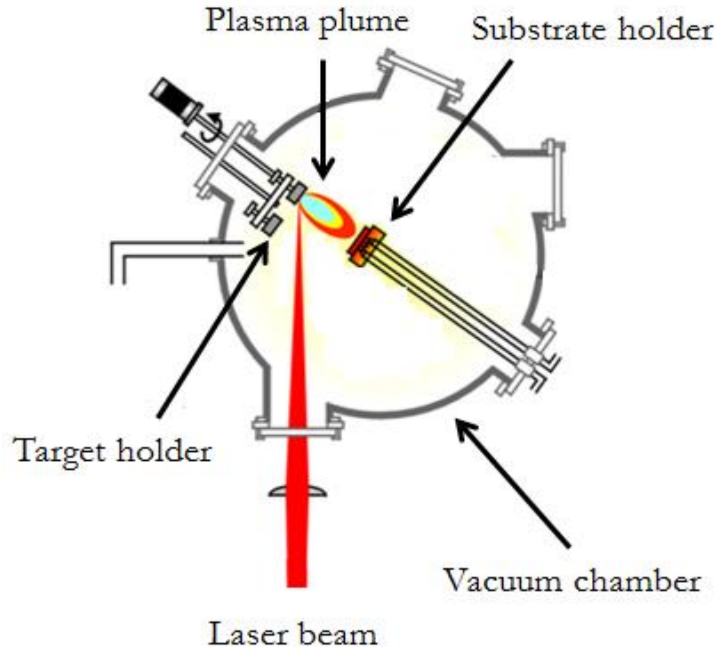

Figure 2.2 Schematic diagram of the experimental pulsed laser deposition setup. A laser ablates target material, resulting in the evaporation thereof towards a substrate under a vacuum environment.

The technique is simple yet versatile, and is widely used to deposit a large variety of materials [11]. In contrast to its apparent simplicity, the physical processes involved in an ablation process are of a great complexity, and have not been fully understood so far [12, 13]. In general thin film formation process in PLD generally can be divided into the following three physical processes:

1. Laser radiation interaction with the target material
2. Plume formation and expansion
3. Nucleation and growth of ablated material on the substrate's surface

Furthermore, these physical processes are dependent on the experimental parameters employed in the deposition process, namely, the laser wavelength, pulse width, the laser fluence (energy per unit area), background gas type and pressure, substrate's type and temperature, the deposition geometry, among others [14]. In following sections, the most important physical phenomena involved in a PLD process will be described briefly.

2.2.1. Laser radiation interaction with the target material

The first physical process in PLD occurs when the high energy pulses emitted by the laser source hit the surface of a solid target, this is often referred to as "laser ablation" (also called photon induced sputtering). In this context "ablation" covers a variety of phenomena which will occur during the laser-target interaction such as absorption, surface melting and vaporization, ejection of particles, plasma

formation and expansion [14]. According to Kelly and Miotello [15] the laser ablation process can be divided into primary and secondary mechanisms that occur simultaneously. The corresponding share of each particular mechanism is difficult to determine. The aforementioned mechanisms are described as follows:

- The target material melts and evaporates by absorbing the laser energy; this is referred to as "thermal ablation or sputtering". The heat conduction equation, the laser and thermodynamic parameters are often used to model this process [16]. Molten droplets can also be expelled from the target material into the plasma plume by the laser induce recoil pressure or the subsurface heating [17].
- Repeated thermal shocks detach flaked shaped chunks of the target. This only happens when the target is made of a material with a high linear thermal expansion coefficient, a high Young's modulus, and a high melting point, this is called "Exfoliational sputtering".
- Transient melting could lead to the formation of droplets at the target's surface, which also induce the formation of asperities on its surface; this is called "Hydrodynamic sputtering".
- The direct interaction between the electronic system of the target and the laser's photons leads to the breaking of the chemical bonds presented in the target, this is called "Non thermal photo-induced electronic sputtering". The photons can also create color centers that enhance thermal absorption of the target material [18].
- Secondary ions and electrons generated by photon collisions from the plasma provoke an indirect collision sputtering of the target which in turn results in cone formation and target erosion [19].

There are many interactions that take place in an ablation process, so only taking into account the laser-target interaction is not enough to fully understand the whole process, the laser-vapor, vapor-target, laser-plasma and plasma-target interactions have to be considered as well. Several theoretical models are proposed to describe this ablation process, however most of them only deal with parts of the interaction or only work for a specific material, thus having limited success [6]. Nonetheless a general characteristic for the ablation process is that every material has an ablation threshold, i.e., a minimum value for the laser power density for which below it not possible to remove any material from the target, the typical power densities for most material are in the range of 10^7-10^8 W/cm^2 [20].

Figure 2.3 shows the basic thermal cycle caused by the interaction of the laser with the target. In Figure 2.3 (a) the laser pulse is absorbed to begin the fusion and vaporization of the target. The molten material is represented by the shaded area and the arrows indicate the movement of the solid-liquid inter phase.

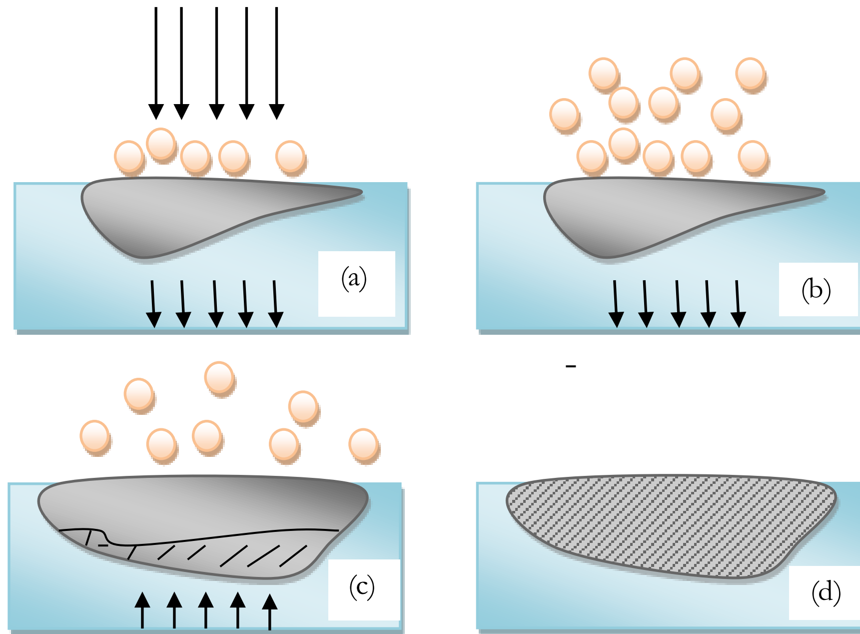

Figure 2.3 Basic thermal cycle induced by a laser pulse (a) Fusion begins, (b) Propagation of the fusion front, (c) Retreat of the fusion process, (d) Complete solidification.

The propagation of the melting front is shown in Figure 2.2 (b) through the material, at the same time as the vaporization thereof occurs. There is recoil in the melting process shown in Figure 2.3 (c); the scratched portions indicate a re-solidified segment in the target. In Figure 2.3 (d) a complete solidification is shown.

2.2.2. Plume formation and expansion

The radiated energy from the laser is partially absorbed by the vaporized material, obtaining very high temperatures on a relatively small surface of the target and therefore an evaporation plume perpendicular to the radiated surface is formed. To avoid deforming the plume, the target is rotated, thus preventing the formation of craters on its surface. This high energy interaction with the vaporized material results in the generation of plasma which expands in a background atmosphere, this plasma contains excited molecules, atoms, ions (mostly positive), electrons, ultraviolet radiation and low energy X-rays [10, 21, 22]. At the beginning of the plasma creation there might be high density of its particles, within the range of $10^{18}-10^{20}$ cm^{-3}, all of this particles begin to interact with each other and tend to lose memory of the primary ablation mechanism [14]. In addition to this, the plasma particles close to the target surface have an anisotropic velocity distribution, i.e., all their velocity vectors point away from the target. Nonetheless, the collision processes between the ablated particles transform this anisotropic behavior into an isotropic one. All of the aforementioned processes take place in a region within just few mean-free paths away from the target surface, which is called the Knudsen layer [23]; this layer plays a critical role in accurately modeling rarefied and micro-scale gases, and in a PLD process is the region where the majority of energy emanated from the laser is absorbed into the plasma. Some models proposed to describe the behavior of the plasma consider it as a fluid, one of them was proposed by Singh and Narayan [24], they

concluded that the acceleration of the plasma varies inversely with its dimensions; therefore the highest velocities are expected to be obtained perpendicularly to the target surface.

The presence of a background gas and its possible reactive character determine the conditions in which the plasma expansion takes place, i.e., since the plume particles besides interacting with each other also interact with the aforementioned gas, additional effects on the former can also be produced, such as: scattering, attenuation and thermalisation. This is due to the fact that many parameters on the plasma plume (The kinetic energy, the spatial distribution and the nature of the species present in the plasma, to name a few) can be altered. Furthermore, the plasma plume particles are capable of reacting with the background gas particles. All this affects the morphology, composition and crystalline structure of the thin films deposited by PLD. Therefore, the control of the plasma expansion dynamics and the analysis of the processes taking place during this expansion are critical for determining optimum synthesis conditions for any sample.

2.2.3. Nucleation and growth of ablated material on the substrate's surface

The nucleation of atomic clusters from the target material onto a substrate involves several processes. The velocity of the atoms that reach the substrate depends on the parameters used in the deposition process, as they can be deposited in various regions thereof, either in empty regions or in those where clusters of atoms where previously deposited. These atoms may subsequently diffuse onto the substrate or surface clusters deposited before them, find other moving atoms to form mobile or stationary clusters, attach to preexisting clusters, be re-evaporated from the substrate, cluster, or film, or remain on the surface of the substrate [24, 25].

Contrary to processes described in the subsections above, the nucleation and growth on the substrates surface for the PLD technique can be described by many existing models, which also apply to other deposition techniques such as beam epitaxy (MBE), sputtering (ion-beam deposition) [20], to name a few: The hree-dimensional material islands (Volmer-Weber), two-dimensional full monolayers (Frank-van Der Merwe), and two-dimensional monolayer growth followed by three-dimensional islands (Stranski-Krastanov), if the growth rate per laser pulse is less than 0.2 nm per pulse [26].

Figure 2.4 shows a schematic diagram of atomic processes in the nucleation of three-dimensional clusters of atoms on the surface of a substrate (1) arrival of an atom to the substrate (2) Re-evaporation from the substrate, (3) Deposition of an atom onto a cluster (4) Re-evaporation from a cluster, (5) Nucleation of a cluster (6) Diffusion of a cluster (7) Disassociation from a cluster.

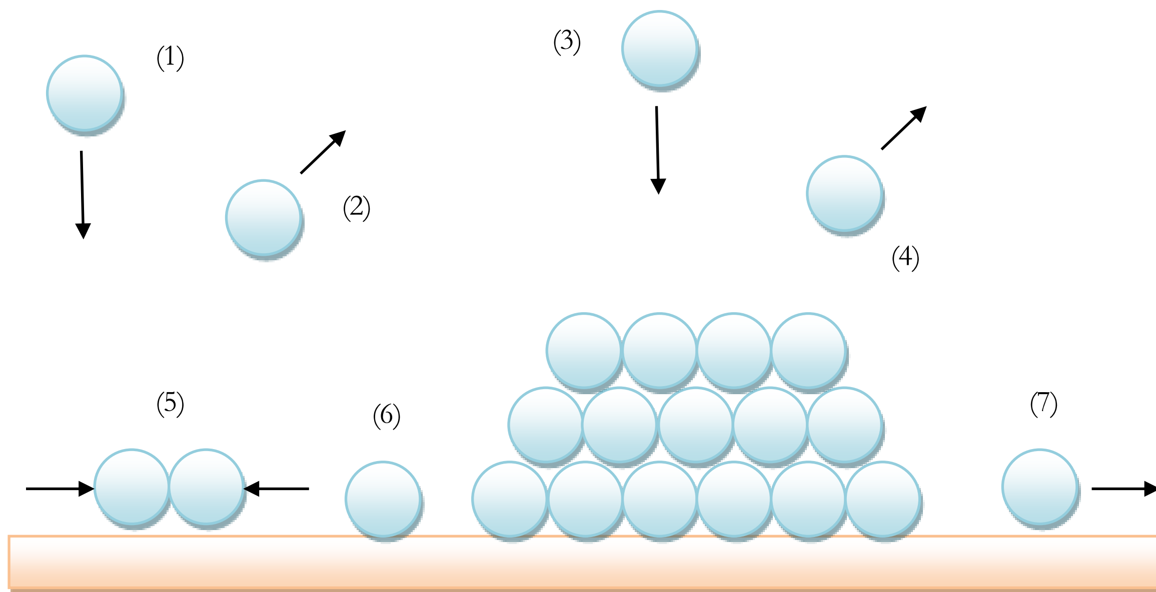

Figure 2.4 Schematic diagrams of the atomic processes in the nucleation of three-dimensional clusters on the surface of a substrate.

2.2.4 Advantages of PLD

Some advantages of the PLD technique are [27, 28, 29]:

1. - It is possible to make deposits of complex oxides with high melting points easily, as long as the materials of the target can absorb the energy of the laser.

2. - PLD allows the growth of films under a highly reactive gaseous atmosphere over a wide range of pressures.

3. - The chemical composition of the target is almost perfectly transferred to the deposited film which results in a highly stoichiometric deposition. This is advantageous when obtaining thin films from targets of different compositions is desired.

4. - The PLD technique is very effective and suitable for the development of epitaxial films and allows the fabrication of multilayers, and heterostructures.

5. - PLD is a versatile, reliable and fast deposition technique. The deposition rate is of the order of some nm/min for substrates areas of about 1 cm^2. The thickness of the films can be easily controlled by varying the number of laser shots.

6. -The laser as an external source of energy for vaporization of materials and the deposition chamber are spatially separated, resulting in an extremely clean process. The PLD does not require a filament or a plasma gas inside the vacuum chamber as opposed to the sputtering or thermal evaporation techniques. Therefore an inert or reactive gas can be applied during the PLD process with virtually no limitations for the pressure values, which can be controlled in ranges from 10^{-4} Torr to 1 Torr [29].

2.2.5. Disadvantages of PLD

Despite these advantages, the industrial applications of the PLD technique have been scarce and slow [18], with very limited use in the private sector. Most of the work on PLD has been carried in scientific research centers and not industries due to its disadvantages, which are listed below [6, 17]:

1. - The volume deposition rate is only 10^{-5} cm^3/s, which is much lower than other PVD techniques like MBE or magnetron sputtering [1]. In addition to this, the energy efficiency of high power lasers is low, which means that the efficiency of PLD is low as well. Therefore the application of the PLD technique is limited to areas of 5 inches in diameter due to the high directionality of the plasma plume. Therefore, without additional lateral scaling of the substrate, sufficient thickness and good homogeneity the growth process is limited to films deposited in an area of 1 in^2 [30].

2. - Depending on target's density and its constituent material and the deposition conditions as well, molten particles and globules, sometimes called "droplets" can be found in deposited films [31]. Their size is about 1 μm. The presence of these droplets is detrimental in many thin film applications [17].

3. - The fundamental mechanisms of PLD, namely, the ablation of the material, the creation and expansion of the plasma, along with the processes of nucleation of the film and its growth, are not fully understood yet, and need continuing fundamental research. Additionally their dependence of the deposition parameters is difficult to control [27, 32].

2.2.6. PLD experimental set-up

The PLD system used for the development of this thesis consists of a vacuum chamber which contains a substrate and target holder. The target holder is attached to a rotational system, which in turn controls the rotational speed of the target. The substrate holder is connected to a heating system which allows to control the temperature at which the deposition is carried out. The vacuum chamber has a quartz window where the laser beam impinges, which is focused by means of a lens system which is placed outside of the vacuum chamber.

The initial stage of vacuum is carried out by a mechanical pump that reaches a pressure in the order of 10^{-2} Torr, afterwards a diffusion pump which under optimum conditions reaches pressures in the order of $\approxeq 10^{-6}$ Torr. There is also a vent employed to allow the entrance of gas if the deposition needs to take place under a reactive atmosphere [14, 33]. A sketch of the PLD equipment is shown in Figure 2.5.

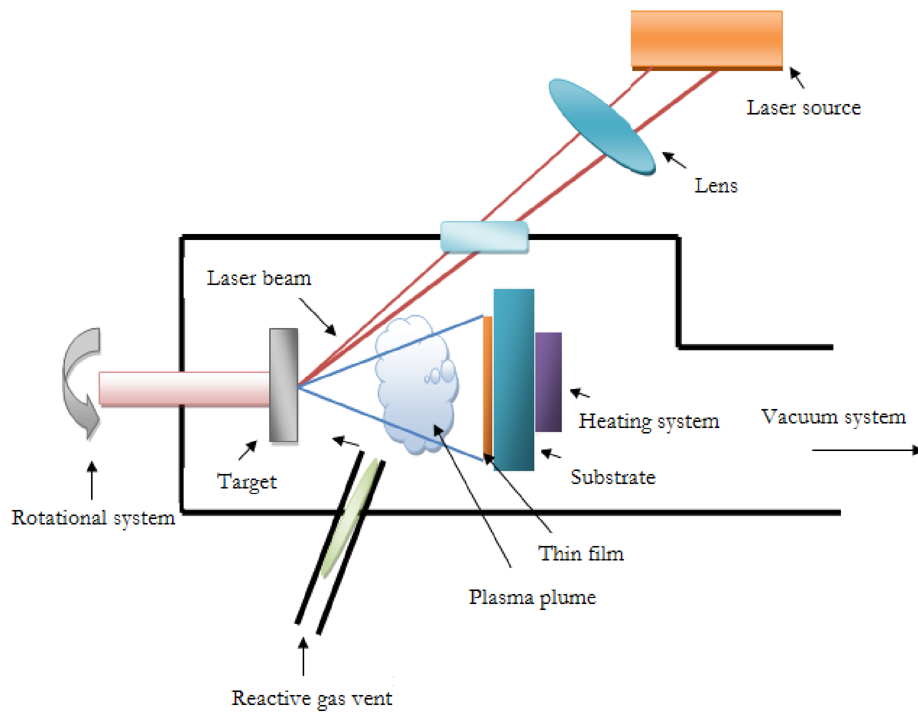

Figure 2.5 Schematics of the PLD deposition system employed for the experimental work on this thesis.

The energy source employed for all the depositions consists in a Nd: YAG (λ= 1068 nm) laser, which operates in frequencies in the range of 1-10 Hz. The laser pulses have energies of around ≃ 2 J/ cm^2 $shot^1$, with a full width at half maximum (FWHM) of 10 ns. The optical system employed to focus the laser beam consists of a lens (focal length 453 nm at 1068 nm) which passes through a window and impinges the target at 45° of incidence [14]. Several vacuum gauges are placed around the deposition chamber to adequate measurement of the pressure within it; MKS 97A sensors were connected to these gauges in order to carry out the measurements. A Picture of the laser employed for the development of this thesis is shown in Figure 2.6.

Figure 2.6 Photograph of the Nd: YAG laser employed in this work [14].

The heating system consisted of a radiation source from a tungsten lamp (300 watts) with a voltage supplied by an Omega CN442Q-TRF1 temperature controller. The heating system allows fine-tuning the temperature variations from room temperature (RT) up to 500 °C with a control of ± 1 °C during growth. As it was mentioned above the heating system is attached to the substrate holder, nonetheless, its setup allows the movement of the substrate holder, therefore the target-substrate distance can be adjust between 10-70 mm. A maximum of four targets can be placed in the system [25], this allows the deposition of multilayer films without breaking the vacuum. A picture of the substrate holder and the heating system is shown in Figure 2.7.

Figure 2.7 Substrate holder and heating system [14].

2.3 Sputtering

The other deposition method employed for de development of this work is the sputtering technique, and just like PLD it is a physical vapor deposition method. It consists of bombarding a negatively polarized target surface (cathode) with particles (usually ions or molecules) originated from plasma. It is customary to employ ions in a sputtering bombarding process due to their ability to be accelerated under an electric field, these ions normally come from an inert gas, and this is because no chemical reaction between the target or the deposited thin film is desired; argon is usually employed in sputtering due to its low price and abundance [34]. The ions generated by the plasma are accelerated towards the target by means of an applied electric field; afterwards the ions impinge on the target thus provoking its erosion. If particles that impinge on the target have the enough amount of energy, its constituent atoms or molecules can be ejected, this is caused by the energy and momentum transmission between the impinging particles and the target's surface. This momentum and energy transmission is the fundamental mechanism of the sputtering process, and it is caused by a cascade of collisions in the superficial layer of solids [35]. The multiple collisions provide enough energy to some atoms in order to leave the target's surface, reach the substrate and get attached to it. Most of the energy provided by the incident ions is converted into heat, which is dissipated by a cooling circuit which prevents the cathode to

overheat. Furthermore, large numbers of target atoms are displaced from their equilibrium positions in the crystal lattice, producing some structural disorder, where even some incident particles are contained within the crystal lattice of the target [36].

When the ions hit the target, in addition to the erosion of the material, other effects occur, such as the emission of secondary electrons and recombination processes, which are responsible for the luminous glow near the cathode surface. Additionally, the secondary electrons contribute to increase the ionization process in the plasma, thus making the bombardment of target more frequent and this effect is used to increase the efficiency of the process by the use of magnets that confine the movement of these secondary electrons, and it will be explained with more detail in a following section. An outline of the processes describe above is shown in Figure 2.8.

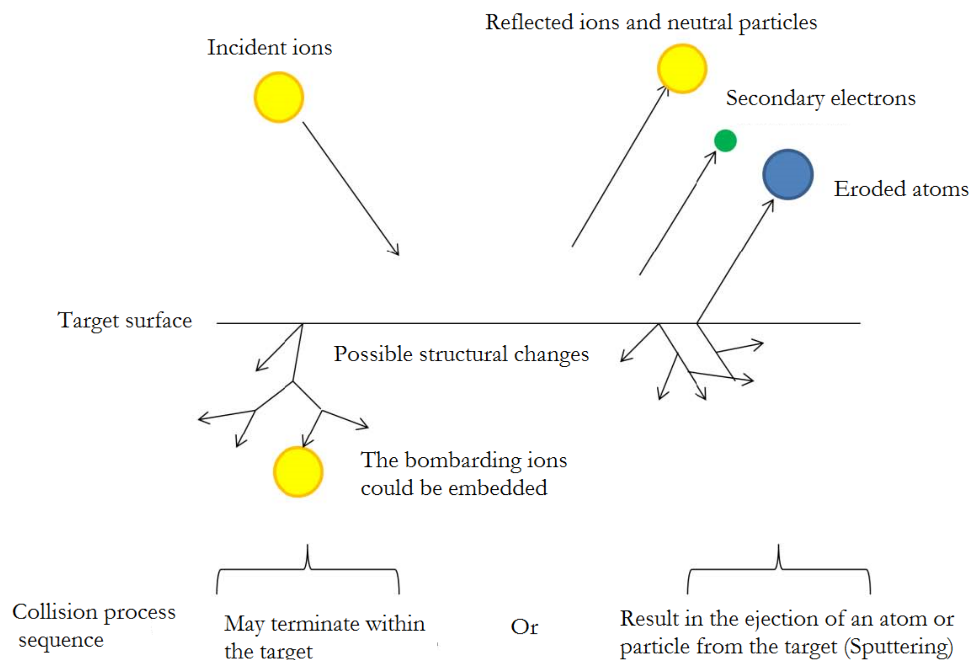

Figure 2.8 A general outline of the sputtering process.

The sputtering technique is widely diffused industrially, particularly in the manufacture of semiconductors and antireflective coatings due to the simplicity of its physical process and its versatility [38]. Among its advantages are: the good film/substrate adhesion caused by the high kinetic energies with which the atoms or molecules arrive to the surface of the substrate, good film uniformity, eroding materials with high melting point is possible, its ability to make depositions in relatively large areas (> 1 m^2), good control of chemical composition under the right conditions. Additionally, the deposited films have the same composition as the target thus having a high reproducibility [37]. Other worth mentioning advantages of the sputtering technique is that it allows deposition processes at relatively low temperatures which are desirable for many applications that require plastic substrates or sensitive photo-resistors which are used in light emitting diodes and solar cells [38]. Finally, it also possible to deposit a great variety of compound thin film coatings using targets of elemental materials under an atmosphere filled with a reactive gas, i.e., oxides and nitrides of many metals are deposited in under atmospheres of oxygen and nitrogen respectively, which combine chemically with the eroded materials, in a process known as reactive

sputtering. However it is also important to point out the principal limitations and disadvantages of the sputtering technique, to name a few:

- The cost of sputtering equipment is relatively high compared to other deposition techniques.
- For some applications the growth process is too slow.
- There are materials that are incompatible with processes that require vacuum, either because of their inherent properties or because of the products they generate during the sputtering process, among them are some organic solids, which often degrade completely.
- The presence of vacuum pumps presents problems with targets having volatile components, resulting in poor films.
- The introduction of defects by energetic particles as they are sputtered onto the pre-existing film is considered undesirable.

The sputtering process takes place in a vacuum chamber, since an adequate vacuum environment is essential to carry out a sputtering process; this allows the average mean free path of the gaseous particles to be so large that they practically do not collide with each other, thus ensuring that eroded species reach the substrate successfully, this is carried out by high vacuum pumps. The pressure range suitable for a deposition is generally between 10^{-2} to 10^{-4} Torr, since at these values both excellent thermal and electrical insulation is achieved; and it is called "working pressure". However, before deposition the chamber is evacuated to pressures of 10^{-7} Torr and then filled with an inert gas until the working pressure is attained again, this considerably decreases the amount of external polluting particles in the gaseous atmosphere that could alter the quality of the resulting thin film. Each sputtering system has a different optimum working pressure, taking into account the fact that there is a relation between the mean free path for the particles contained in the plasma and the required pressure to sustain the ionizing discharge. The smaller the pressure the greater the mean free path, and therefore the greater the energy at which the particles reach the target and the substrate. However if the pressure is too low there are not enough ions and discharge is extinguished quickly.

2.3.1. Different types of sputtering systems

Plasma is defined as a gas which partially consists of ions, atoms and electrons [39]. There are a lot of processes that occur in plasma, among them, is the collision of electrons with atoms or molecules from the inert gas used, which is the most important in sputtering, this process is known as ionization and is the basis for obtaining plasma. In a sputtering deposition there is always a characteristic glow which is given by the relaxation of the atoms excited by the electrons which are accelerated towards the anode. There are different ways to create plasma and in the following sections the different sputtering configurations employed to do so will be described in detail.

2.3.2. DC Sputtering

As it was mentioned before, there are different ways to configure a sputtering system in such a way that target erosion occurs. The simplest way to do so is through the generation of plasma with a direct current (DC) diode discharge. This discharge requires two electrodes placed in a high vacuum chamber and an external high voltage source. The material that is desired to be eroded is the target in the

sputtering process, which becomes the cathode of an electric circuit and has a high negative voltage V (DC). The substrate is where the thin film grows and is placed on an anode that is electrically grounded a few inches away from the cathode [34]. Hence an electric field is always present in the vacuum chamber during deposition and its role is to accelerate the electrons towards the anode.

Under appropriate gas density conditions, electron will have enough energy to ionize the gas atoms in the chamber by colliding with them, thus generating ions and secondary electrons. Afterwards these charged particles are accelerated by the electric field, the electrons towards the anode (causing more ionization in their path) and the ions towards the cathode, producing an electric current. The ions that are accelerated towards the target can tear away some its atoms by colliding with it, while also contributing to the emission of secondary electrons, which enables the ionization to continue, in fact these secondary electrons are responsible for sustaining the glowing discharge. When the number of generated electrons and ions is equal and when there is the same amount of electrons as of ions, the plasma reaches certain equilibrium and the discharge is said to be self-sustained, that is when a characteristic glowing light is observed in the gas. The atoms that were tore away from the target travel in different directions and some of them reach the substrate (the anode), condense and form the thin film [34].

Most of the energy that results from the collision between the ions and the target is transformed into heat, that's why a cooling circuit is required to avoid overheating the cathode. A schematic of a DC sputtering system is shown in Figure 2.9.

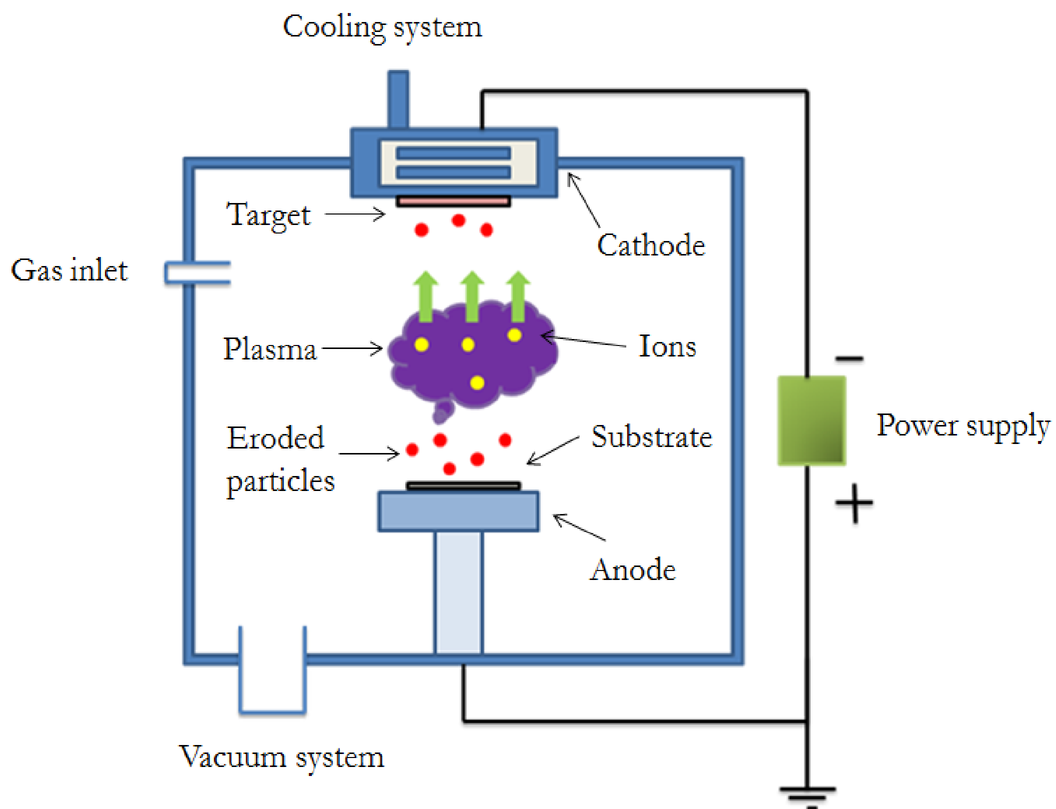

Figure 2.9 Schematic diagram of a DC sputtering setup.

2.3.3. RF sputtering

The main limitation of the DC sputtering process is its inability to maintain the luminescent discharge when the target placed in the cathode is an insulating material instead of a metallic one. When an insulating material is placed in the cathode of a DC sputtering system an unavoidable positive charge build-up occurs on the target's surface due to the constant ion bombardment. This accumulation of charge can lead to a decrease in the sputtering efficiency, even stopping the discharge altogether. To get around this problem the DC power source is replaced with a Radio Frequency (RF) operating one. The RF voltage source operates as follows: For a small part of the radiofrequency cycle, the cathode and anode reverse their polarities. This eliminates the accumulation of positive charge on the target by providing an equal number of ions, then electrons, then ions, and so on. This allows to successfully eroding almost any insulating material [40]. This is made by changing the polarity of the anode-cathode bias at a high frequency rate, normally is 13.56 MHz, which a conventional frequency for industrial, scientific and medical uses [41]. This alternating polarity has an additional benefit as well. When the polarity of the electric field is change, the electrons that have not reached the substrate yet will be accelerated towards the "new" anode, therefore increasing the chances of colliding with an atom. This implies a higher sputtering rate and density of ions.

2.3.4. RF magnetron sputtering

One of the major drawbacks of a conventional sputtering process is the inevitable heating of the substrate caused by the bombardment of secondary electrons and its low deposition rates. The use of magnetron which provides a strong magnetic field in the close vicinity of the cathode was conceived to solve this issue. The magnetic field confines the electrons in an intense plasma region near the cathode; this severely increases the electron density being nearly 10 to 1000 greater than in a traditional the sputtering process, thus, the secondary electrons generated in the bombardment are confined to a region near the surface of the cathode, where these electrons are governed by the Lorentz force and forced by helical paths parallel to the surface of the cathode. This increases the ionization of the working gas resulting in higher ion current densities (typically 10 to 100 times higher than a sputtering without magnetron [42]) at considerably lower working pressures (in the range of 0.1 to 1 Pa), consequently the eroded atoms from the target go under fewer collisions in their way to the substrate, thus having more kinetic energy when they reach thereof. It should be mentioned that a cooling system is necessary for the cathode in any magnetron system, since increasing the ionization rate increases the amount of ions that bombard the target, which can cause its melting due the excess of heating. Figure 2.10 shows a schematic of a magnetron Sputtering set-up.

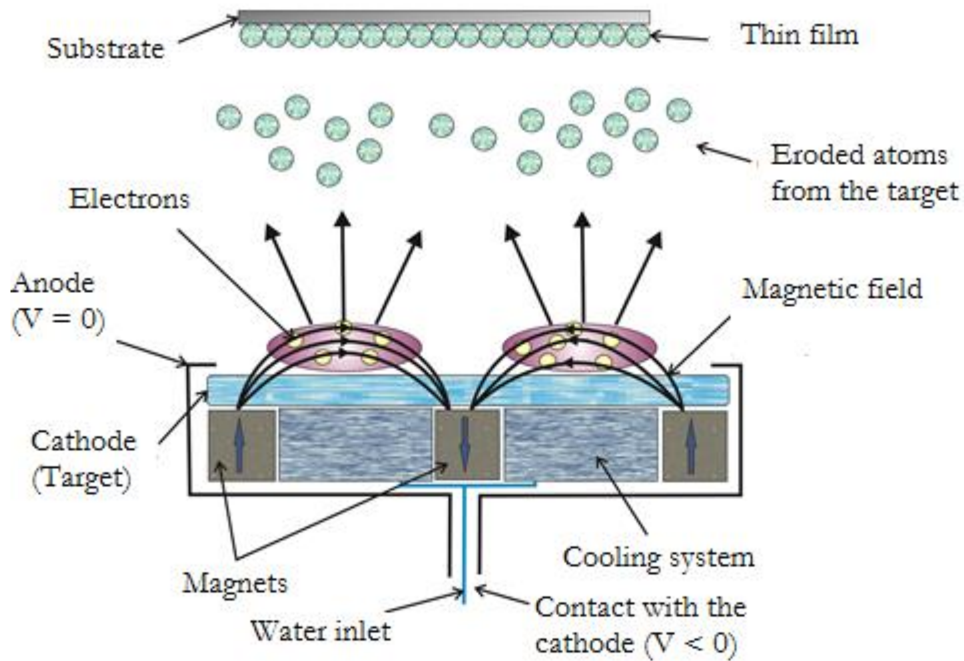

Figure 2.10 Schematic diagram of a magnetron sputtering process [43].

In Figure 2.10 the electrons are confined in a region close to the cathode and cannot move freely, this eliminates much of the heating that the substrate undergoes due to the electrons that could impinge its surface [44]. The magnetic field is generated through magnets located in line with the cathode. A disadvantage of a magnetic field-assisted sputtering process is that the material erosion is not uniform and there is a large wastage of material. This is due to the fact that the sputtering of target is more intense where the magnetic field lines are parallel to the surface of the cathode.

2.3.5. Sputtering experimental set-up

The RF-magnetron sputtering system used for the development of this thesis consists of a mechanical vacuum pump, a turbo-molecular vacuum pump with its respective controller, two Lesker's Torus magnetron guns with 3 inches in diameter each, a micro-Pirani vacuum sensor, a radiofrequency voltage source, a matching network to control de amount of power and charge supplied to the system, control valves for the gases employed, a cooling system for the magnetron, a substrate holder with its respective shutter and a glass vacuum chamber. Pictures of the RF-magnetron sputtering system employed for the development of this thesis is shown in Figure 2.11.

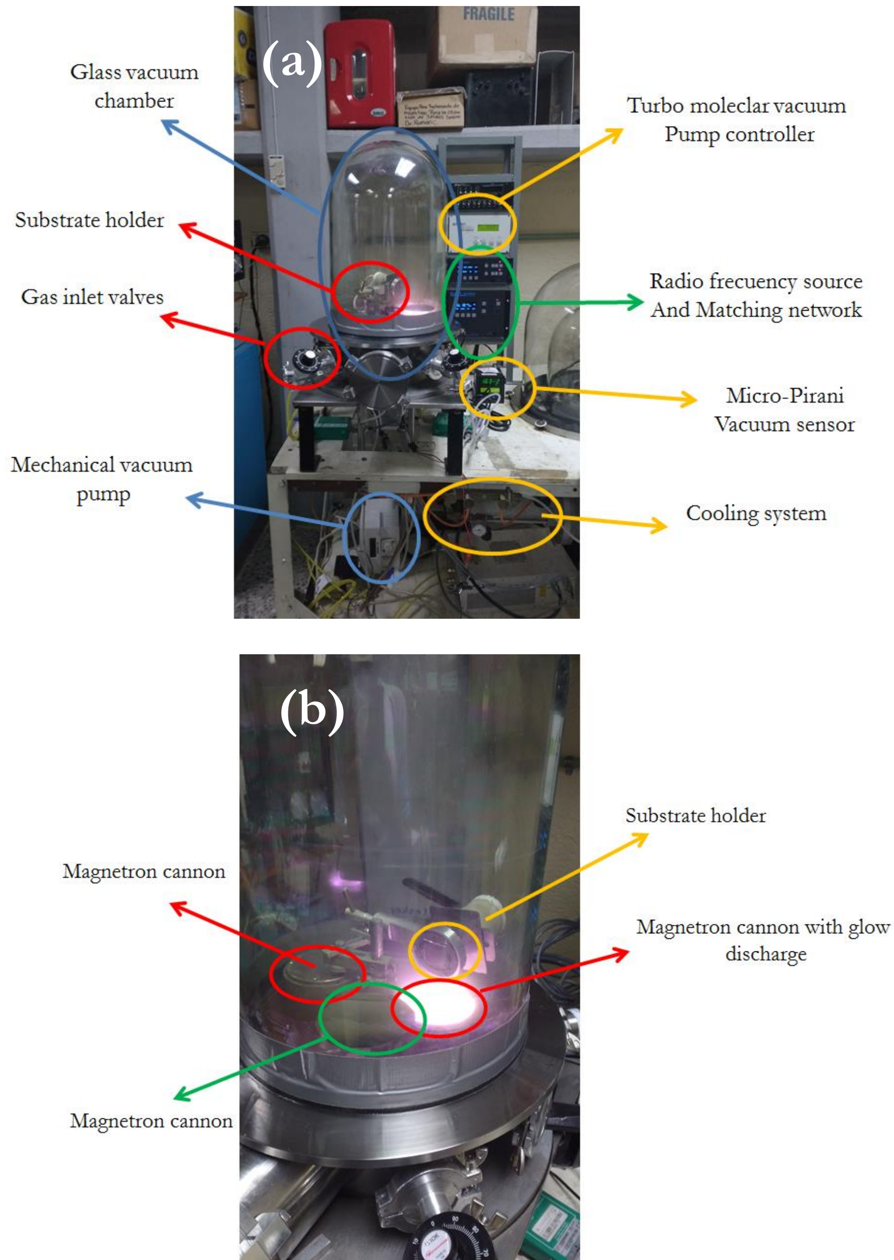

Figure 2.11 RF-magnetron sputtering employed in this work (a) front view (b) top view.

2.4 References

[1] María Dalmira Rodríguez Martín, Depósito del óxido ternario Cd-Te-O por láser pulsado, Master's Thesis, Centro de Investigación y de Estudios Avanzados del Instituto Politécnico Nacional Unidad Mérida, 2003

[2] L. I. Maissel and R. Glang, Handbook of Thin film technology, Mc Graw Hill Book Company, 1983

[3] A.Goswami, Thin Film Fundamentals, New Age International (P) Limited, New Delhi, 1996

[4] José Guadalupe Quiñones Galván, Síntesis y caracterización de películas delgadas de la aleación $Si_{1-x-y}Ge_xC_y$ depositadas mediante ablación láser, Master's Thesis, Centro de Investigación y de Estudios Avanzados del Instituto Politécnico Nacional, 2008

[5] G.W. Martin, L.A. Doyle, A. Al-Kateeb, I. Weaver, D. Riley, M.J. Lamb, T. Morrow, C.L.S. Lewis, Three-dimensional number density mapping in the plume of a low-temperature laser-ablated magnesium plasma, Applied Surface Science 710 (1998) 127–129

[6] K. Ellmer , A. Klein., Transparent Conductive Zinc Oxide Basics and Applications in Thin Film Solar Cells, Springer, Berlin Heidelberg New York, 2008.

[7] A. Kühle, J. L. Skov, S. Hjorth, I. Rasmussen, J. Bindslev Hansena, Smooth $YBa_2Cu_30_{7-x}$ thin films prepared by pulsed laser deposition in 0_2/Ar atmosphere, Applied Physics Letters 64 (1994) 3178-3180

[8] D. Dijkkamp, T. Venkatesan, X. D. Wu, S. A. Shareen, N. Jiswari, Y. H. Min-Lee, W. L. McLean, and M. Croft, Preparation of Y-Ba-Cu Oxide Superconductor Thin Films Using Pulsed Laser Evaporation from high Tc Bulk Materials, Applied Physics Letters 51 (1987) 619-621.

[9] H.M. Smith and A.F. Tuner, Vacuum Deposited Thin Films Using a Ruby Laser, Applied Optics 4 (1965) 147-148.

[10] A. Husmann, Pulsed Laser Deposition mittels gütegeschalteter CO_2-Laser. PhD Thesis, RWTH Aachen, 1999

[11] D. Bäuerle, Laser Processing and Chemistry, 3rd edn. Springer, Berlin Heidelberg New York, 2000.

[12] G.W. Martin, L.A. Doyle, A. Al-Kateeb, I. Weaver, D. Riley, M.J. Lamb, T. Morrow, C.L.S. Lewis, Three-dimensional number density mapping in the plume of a low-temperature laser-ablated magnesium plasma , Applied Surface Science (1998) 710-715

[13] A. Ohtomo, A. Tsukazaki, Pulsed laser deposition of thin films and superlattices based on ZnO, Semiconductor Science and Technology 20 (2005) S1

[14] Juan Manuel Camacho Pérez. Synthesis and characterization of transparent and conductive CdTe- and Te doped In_2O_3 by pulsed laser deposition, PhD Thesis, Centro de Investigación y de Estudios Avanzados del Instituto Politécnico Nacional Unidad Mérida, 2008

[15] R. Kelly, A. Miotello, Mechanisms of Pulsed Laser Sputtering. In: Pulsed Laser Deposition of Thin Films, ed. by D.B. Chrisey, G.H. Hubler, Wiley, New York Chichester Brisbane Toronto Singapore, 1994

[16] H. Hügel, F. Dausinger, Laser Physics and Applications, Springer, Berlin Heidelberg New York , 2004

[17] L.C. Chen, Particulates Generated by Pulsed Laser Ablation. In: Pulsed Laser Deposition of Thin Films, Wiley, New York, 1994

[18] J. Gottmann, Dynamik der Schichtabscheidung von Keramiken mit KrF Excimer- Laser strahlung. PhD Thesis, RWTH Aachen, 2001

[19] S.R. Foltyn, Surface Modification of Materials by Cumulative Laser Irradiation. In: Pulsed Laser Deposition of Thin Films, Wiley, New York, 1994

[20] D.B. Chrisey, G.K. Hubler, Pulsed laser deposition of thin films, Wiley, New York, 1994.

[21] C. Manzano García, Nanoestructuras de CdS depositadas por la técnica de Ablación Láser, Master's Thesis, Centro de Investigación y de Estudios Avanzados del Instituto Politécnico Nacional Unidad Mérida, 2000.

[22] J.A. Greer, M.D. Tabat, Large area pulsed laser deposition: techniques and applications, Journal of Vacuum Science & Technology A: Vacuum, Surfaces, and Films 13 (1995) 1175.

[23] R. S. Myong, Theoretical description of the gaseous Knudsen layer in Couette flow based on the second-order constitutive and slip-jump models, Physics of Fluids 28 (2016) 012002

[24] Rajiv K. Singh and J. Narayan, Pulsed-laser evaporation technique for deposition of thin films: physics and theoretical model, Physical Review B 41 (1990) 8843

[25] M. Herrera, R. Castro-Rodriguez, O. Gomez, V. Rejón, P. Bartolo-Perez, S. Barkun, A. Martel, J.L. Peña, Multitarget system for growth of thin films by pulsed laser deposition, Revista Mexicana de Fisica 48 (2002) 61-66

[26] J.S. Horwitz, Film Nucleation and Film Growth in Pulsed Laser Deposition of Ceramics. In: Pulsed Laser Deposition of Thin Films, Wiley, New York, 1994

[27] U. Madhu, N. Mukherjee, N. R. Bandyop, A. Mondal, Properties of CdS and CdTe thin films deposited by an electrochemical technique, Indian Journal of Pure & Applied Physics 45 (2007) 226-230

[28] T. Venkatesan, Pulsed Laser Deposition - Future Trends. In: Pulsed Laser Deposition of Thin Films, Wiley, New York, 1994

[29] D.Bauerle, Laser Chemical Processing. In: Landolt-Bornstein New Series, Group VIII Advanced Materials and Technologies, Laser Physics and Applications, Springer, Berlin Heidelberg New York, 2004.

[30] K. Werner, K. Schuegraf, Handbook of Thin-Film Deposition Processes and Techniques; Principles, Methods, Equipment and Applications, Noyes Publications, United States of America, 2002.

[31] Heungsoo Kim. Pulsed Laser deposition of thin films applications-LED growth of functional materials. John Wiley & Sons, Inc. Hoboken, New Jersey, 1907.

[32] M. Frumar, B. Frumarova, P. Nemec, T. Wagner, J. Jedelsky, M. Hrdlicka, Thin chalcogenide films prepared by pulsed laser deposition – new amorphous materials applicable in optoelectronics and chemical sensors, Journal of Non-Crystalline Solids 352 (2006) 544–561.

[33] David Reyes Coronado. Correlación entre la distancia target-sustrato y la presión de oxígeno en el crecimiento de películas delgadas de óxidos complejos por PLD, Masther's Thesis, Centro de Investigación y de Estudios Avanzados del Instituto Politécnico Nacional Unidad Mérida, 2003.

[34] Chapman B. N., Glow Discharges Process; Sputtering and plasma etching, Wiley, New York 1980

[35] Kiyotaka W., Makoto K., Hideaki A. Thin Film Materials Technology; Sputtering of Compound Materials, Springer, Berlin Heidelberg New York, 2004

[36] S. M. Rossnagel, Sputter deposition for semiconductor manufacturing, IBM Journal of Research and Development 43 (1999) 163 - 179

[37] José Montero Amenedo, Óxido de estaño dopado con antimonio y otros materiales relacionados con la conversión y ahorro de energía, Universidad Complutense de Madrid Facultad de Ciencias, PhD Thesis 2013

[38] Zhiyun Zhang, Chonggao Bao , Wenjing Yao, Shengqiang Ma, Lili Zhang, Shuzeng Hou, Influence of deposition temperature on the crystallinity of Al-doped ZnO thin films at glass substrates prepared by RF magnetron sputtering method, Superlattices and Microstructures 49 (2011) 644–653

[39] S. A. Campbell, The science and engineering of microelectronic fabrication, Oxford University Press, New York, 2001.

[40] Werner K., Schuegraf K. Handbook of Thin-Film Deposition Processes and Techniques; Principles, Methods, Equipment and Applications, Noyes Publications, Santa Barbara California, 2002

[41] K. Seshan. Handbook of Thin-Film Deposition Processes and Techniques - Principles, Methods, Equipment and Applications (2nd Edition), William Andrew Publishing/Noyes, Santa Barbara California, 2002.

[42] Ohring, M. Materials science of thin films Deposition & structure, Academic Press, Orlando Florida, 2002

[43] Luis German Daza Casiano, Películas delgadas de óxido de zinc dopadas con aluminio (AZO) sobre substratos flexibles obtenidas por RF sputtering no reactivo, Master's Thesis, Centro de Investigación y de Estudios Avanzados del Instituto Politécnico Nacional Unidad Mérida, 2014.

[44] Golan G., Axelevitch A. Ring etching zones on magnetron sputtering targets, Thin Solid Films, 300 (1997) 72-77.

Chapter 3 Characterization techniques

This chapter briefly describes the characterization methods employed throughout the development of this thesis. The present work focused in the characterization of the structural, morphological, optical, chemical and electrical properties for the deposited thin films. X-ray diffraction (XRD), atomic force microscope (AFM), scanning electron microscopy (SEM), Profilometry, UV-Vis spectroscopy, X-ray photoelectron spectroscopy (XPS) and the Van der Pauw method were the techniques chosen for this purpose. For further information regarding the experimental set-up on the specific studies the reader is advised to look in the experimental sections in each individual chapter of this thesis.

3.1 X-ray Diffraction (XRD)

The structural characterization of the obtained samples was done by XRD. Like visible light, X-rays are electromagnetic radiation, however, they possess a much shorter wavelength (in the range of 0.1 to 10 nm), which is comparable to the interatomic distances in solids. When an X-ray beam hits a solid, they are dispersed in all directions. Most of the radiation scattered by one atom cancels the radiation scattered by other atoms. However, some X-rays reach certain crystallographic planes at specific angles; this reinforces the incident radiation rather than destroy it. This phenomenon is called diffraction. X-rays are diffracted, i.e., the beam is reinforced, if there is an orderly arrangement of atoms and if the conditions given by Bragg's law are fulfilled [1]:

$$n\lambda = 2dSin\theta \qquad n = 1,2,3\ldots\ldots\ldots \tag{3.1}$$

Where θ is the grazing angle of the incident X-ray, n is an integer number, d the crystal plane separation distance and λ is X-ray wavelength. Figure 3.1 shows a schematic of all the elements presented in a diffraction phenomenon. If Bragg's law conditions are not met, the interference is of a non-constructive nature and diffracted beam is of a very low intensity.

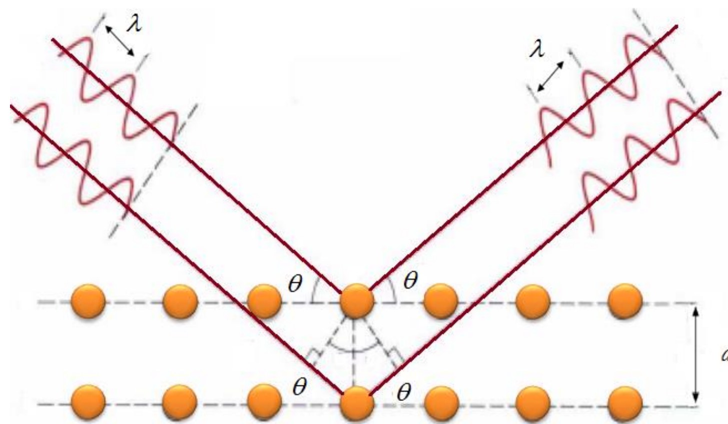

Figure 3.1 Schematic of the X-ray diffraction phenomenon.

The diffractometer is an apparatus used to determine the angles at which diffraction occurs in a given sample. It consists of a source and a detector, which are subsequently titled at angles of 0° and 180° respectively, afterwards the source is rotated around the sample while the detector is rotated in the opposite direction at the same speed. A schematic of an X-ray diffractometer is shown in Figure 3.2.

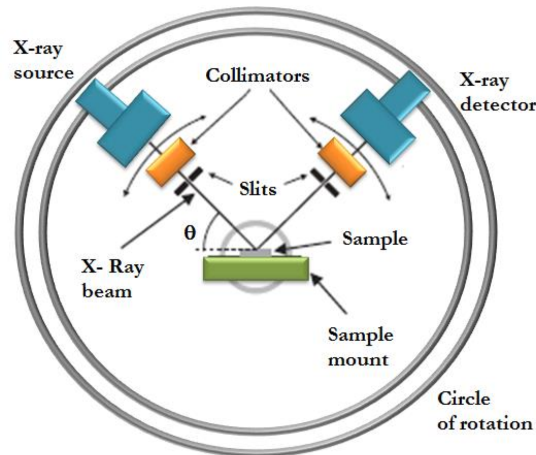

Figure 3.2 Schematic of the X-ray diffractometer.

The detector records the 2θ angles at with which the beam is diffracted and its respective X-ray yield (counts), thus producing characteristic diffraction pattern, this pattern is presented in a graph, known as "diffractogram", which is used to determine the crystalline properties of studied material (number of diffracted crystallographic planes, preferential orientation, grain size, induced stress in the film as well as possible structural defects). A crystalline material will produce a characteristic diffraction pattern. In a sample whose structure is formed by a set of phases of different materials, the corresponding diagram will show the individual diffraction patterns of each one of them. In this work, a Siemens D-500 X-ray diffractometer was used at CINVESTAV-IPN in Merida. The employed source of radiation was Cu-Kα (λ=1.5418 Angstrom) in the grazing incidence angle mode. This geometry increases the effective X-ray path through the film, while the diffracted intensity of the substrate is reduced. In general, the thin film signal-to-noise ratio increases significantly.

3.2 Atomic force microscopy (AFM)

The atomic force microscope (AFM) is a mechanical-optical instrument that allows obtaining topographic images with high spatial resolution for a given surface. The AFM consists of a cantilever with a sharpened tip (probe) at its end, which has a conical or pyramidal shape; this tip is used to scan the surface of the sample. When the tip is brought close to the surface of the sample, the forces presented between the former and the latter deflect the cantilever according to Hooke's law. Depending on the situation, the forces measured in this type of microscopy include: mechanical contact forces, Van der Waals forces, capillary forces, electrostatic forces, etc. How much the cantilever is deflected is measured by a laser beam, which is reflected in a photo-detector, this is done in order to calculate the force applied to the cantilever. Two scanning modes are typically used in AFM measurements: keeping the tip at

constant height or at constant force. In the first case, when the tip and the atomic surface atoms approach to each other, the forces caused by their interaction increase and when they are moved apart decrease so the height between them remains constant. In the second case, the tip will approached or move apart from the surface of the sample depending on morphology, so that the force between the tip and the sample is kept constant. These movements are captured by the photo-detector registers and are subsequently transfer into computer software as a topographic image of the sample. The obtained images are then used to estimate the grain size and roughness of the deposited film [2]. The importance of the AFM technique lies in the fact that it is useful to determine the surface quality of the studied samples, which is important for many applications where the morphology of the material plays a key role [3]. All the measurements for this thesis were performed at atmospheric pressure and room temperature in the constant force mode; 2D and 3D images were obtained with different dimensions. Figure 3.3 shows a schematic of an AFM system.

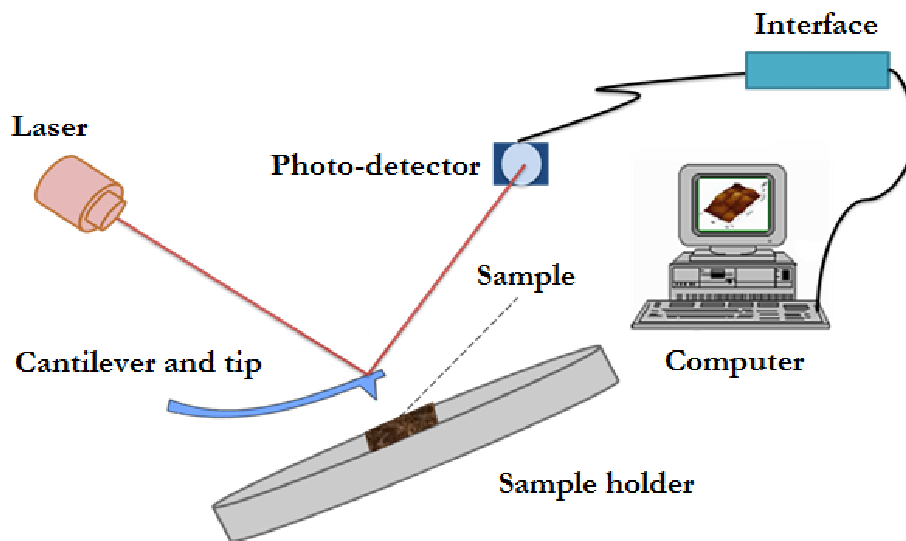

Figure 3.3 Schematic of an AFM device.

3.3 Thin film thickness

Unlike bulk materials the thickness is parameter that plays a key role in films, this is due to the fact that reproducible properties are only achieved when the film thickness and deposition parameters remain constant. In this thesis the profilometry technique was employed for film thickness determination. In a profilometer a moving tip is brought into contact with the surface of a given material. This tip scans the surface of the sample applying a constant force on it. It is possible to adjust both the sweep length and the magnitude of the applied force depending on particular characteristics of the film. The tip is connected to a measuring system that records its vertical displacements along the studied surface, thus determining the changes in thickness.

A Veeco profilometer model Dektak 8 Stylus Profiler, owned by the CINVESTAV-IPN Mérida Unit, was employed to carry out most thicknesses measurements in this work. The aforementioned apparatus can analyze samples with a maximum length and height of 200 and 75 nm, respectively. There is region of the deposited film that has to be covered with some kind of mask or tape; this creates a step on

its surface so the thickness can be accurately measured by the vertical motion of the stylus tip over the step. A schematic of the profilometry technique is shown in Figure 3.4.

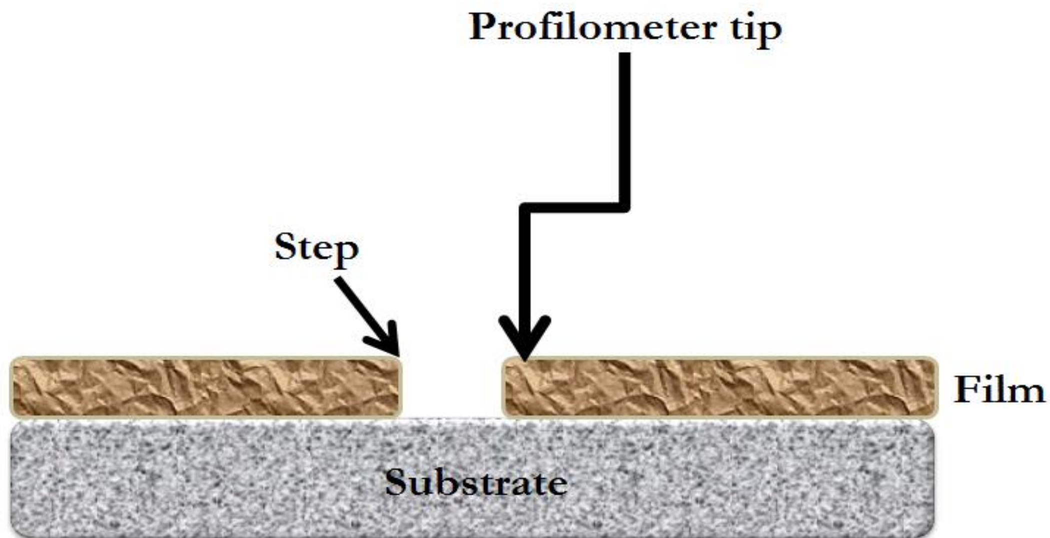

Figure 3.4 Schematic of the thickness measurement carried out by a profilometer.

3.4 X-ray photoelectron spectroscopy (XPS)

X-ray Photoelectron Spectroscopy (XPS), also known as Electron Spectroscopy for Chemical Analysis (ESCA) is surface characterization technique employed to analyze the chemical composition and oxidation states from the surface of a solid material [4]. Its functioning is based in the photoelectric effect, where the electrons are ejected from the surface of a material due to photonic irradiation [5]. When X-rays of known energy hν (generally Al Kα or Mg Kα at 1486.7 eV and 1253.6 eV, respectively) interact with an atom, a photoelectron can be emitted, as is shown in Figure 3.5.

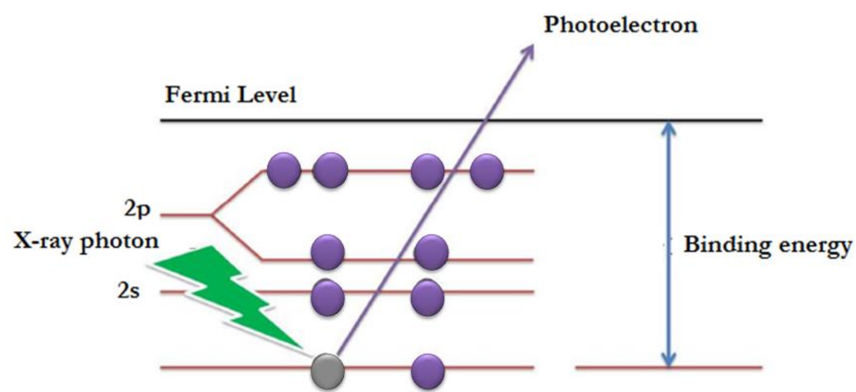

Figure 3.5 A Scheme of X- ray photoelectron spectroscopy process.

Afterwards, the kinetic energy of the emitted electron (KE) is measured and atomic core level binding energy (BE) relative to the Fermi level (E_f) is determined using the following equation:

$$(BE) = hv - (KE) - \varphi_{sp} \tag{3.2}$$

Where φ_{sp} is the work function of the spectrometer. A typical XPS spectrum is a plot of the number of electrons detected (Y axis) versus their respective binding energy (X axis). Each element produces a

characteristic set of XPS peaks at different binding energy values that are used to identify each constituent element of the surface of the material being analyzed. Almost every element from the periodic table can be identified using the various core binding energies obtained in a XPS spectrum, with the exception of hydrogen and helium [6]. Due to the fact that the binding energies are sensitive to the atomic chemical environment, other useful information such as the chemical states of the constituent elements can be obtained from an XPS analysis, this information is obtained by relating every peak plotted in the XPS spectrum to its respective chemical element, there is a wide variety of tables and manuals where the particular spectrums of known elements and compounds are reported [7]. To carry out a quantitative analysis of the obtained XPS spectrum the relative concentrations C_x are estimated using the following expression:

$$C_x = \frac{I_x / S_x}{\sum_i \left(I_i / S_i \right)} \qquad (3.3)$$

Where I_x is the height or area for the element x, S_x is the relative sensitivity of the photoelectron peak, the sum is made over all the present elements.

3.5 Scanning Electron Microscope (SEM)

The scanning electron microscope (SEM) is a type of electron microscope that employs electrons rather than light to form an image. This characterization method is widely used to study inorganic and organic materials an presents many advantages over a conventional optical microscope [8]. In this technique the surface of the sample is scanned with a high-energy beam of electrons, thereby producing high-resolution images of the studied material.

Different types of signals are generated by the interaction of the electron beam (which is normally generated by a tungsten filament [9]) and the surface of the sample, which are subsequently collected by electronic detectors to construct a high resolution image of the latter. Secondary electrons (SE) and backscattered electrons (BSE) are most commonly used to generate the aforementioned images. The secondary electrons are classified as low energy electrons (<50 eV) and are produced by the inelastic scattering between primary electrons and electrons of atoms in the sample (they are normally used in the morphological investigation), while the backscattered electrons have energies above 50 eV, and are generated by elastic scattering. Any measurement carried out by a SEM device must be carried out under a vacuum environment; this prevents the scattering of the electrons by air molecules. Electromagnetic lenses are used to focus the incoming electronic beam on the sample; afterwards the studied area in the sample is scanned and the scattered signals are recorded to construct a high resolution image. The resulting images are useful to study superficial properties at high magnification, to evaluate morphological features, such as grain sizes and local structures, among others. Figure 3.6 shows and schematic of a SEM apparatus.

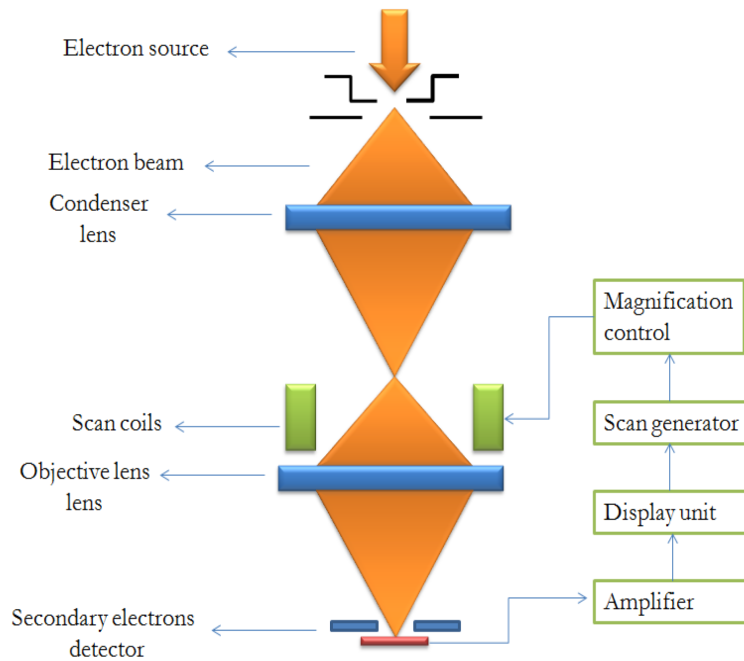

Figure 3.6 Schematic diagram of a Scanning Electron Microscope (SEM) General Setup.

A scanning electron microscope is also employed to carry out an energy dispersive X-ray spectroscopy (EDS) analysis. This technique is used to identify the elemental composition of the studied sample. To generated and EDS spectra, the sample is exposed to an electron beam inside a SEM apparatus. These electrons collide with the electrons within the sample and knock them out from their orbits. The higher energy electrons come to the evacuated positions and emit X-rays, which are in turn used to determine the elemental composition of the studied sample.

3.6 Optical characterization

When electromagnetic waves interact with matter they can be dispersed, transmitted, or absorbed, spectroscopy studies the way in which these interactions take place. This gives rise to the three main branches of spectroscopy. Emission spectroscopy studies the emitted light by atoms produced by radiation-matter interactions, Raman spectroscopy studies the light scattered by molecules, lastly, absorption spectroscopy deals with research of absorbed radiation at various wavelengths.

In the present work, the optical absorption spectroscopy technique was employed to characterize the resulting optical properties of the ZnO thin films. This technique allows to measure the optical absorption spectrum of a material and thus to study its band structure. When an absorption process takes place, a photon of known energy excites an electron from state of low energy to one of higher energy, i.e., the electron moves from a state in the valence band to another one in the conduction band, this is achieved by providing energy from an external source such as: heat, a magnetic field or electromagnetic radiation.

The optical transmittance is the fraction of incident light at a specific wavelength which passes via a sample, it measurement is carried out by impinging a monochromatic beam on the studied material using a UV-Vis spectrophotometer; it is expressed in a percentage [10]. This technique is considered very useful

to characterize many of the optical properties in many materials: the possible electronic transitions, the optical band gap (E_g), the distribution of energy , among others.

An Agilent 8453 ChemStation UV-Visible spectrophotometer was used to carry out the optical measurements for this work. The spectrophotometer consisted of three fundamental blocks:

1. Light Source: Usually consists of tungsten or xenon lamps.
2. Mono-chromator: Selects any specific wavelength of the incident light.
3. Photo-detection system: Collects the detected light signals that go through the sample and sends them into a computer.

3.6.1 Determination of the optical band gap

The transmittance spectrum is often used to derive optical parameters like absorption coefficient (α) and band gap (E_g) of studied material. When electromagnetic radiation impinges the surface of a solid, part of it will be absorbed. The fraction of absorbed radiation (without considering losses due to energy dissipation and reflections) depends on the nature and thickness of the material. For a semiconductor, this interaction is defined in terms of the absorption coefficient (α), which is a measure of the amount of incident energy that is absorbed as it is propagated in a medium. It characterizes the absorption properties of the material and is defined is defined as follows: I_0 is the intensity of the incident light, I the intensity of the transmitted light beam and the thickness of the sample is denoted by d. Figure 3.7 shows these terms with a scheme that represents the change of intensity of the incident radiation when it goes through a thin film.

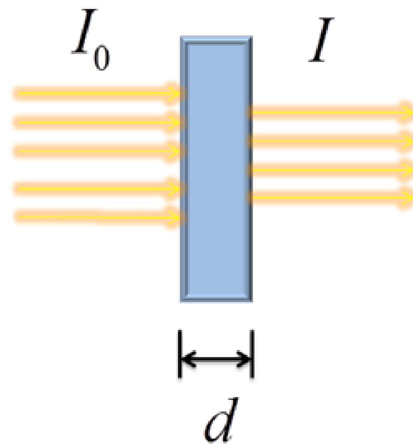

Figure 3.7 Schematic diagram of the optical transmission in a thin film.

The intensity of the transmitted radiation I is proportional to the incident beam intensity and thickness of the material:

$$dI' = -\alpha I_0 dx \tag{3.4}$$

By integrating (3.4) from I_0 to I, and taking into account the thickness of the sample:

$$\int_{I_0}^{I} \frac{dI'}{I} = -\int_0^d \alpha dx \tag{3.5}$$

Thereby the following expression will be obtained:

$$\frac{I}{I_0} = e^{-\alpha d} \tag{3.6}$$

The expression (3.6) is known as the Beer-Lambert law, which establishes the relation between the absorption coefficient and the transmittance spectra [10]. The previous relation can be rearranged into:

$$\alpha(\lambda) = \frac{1}{d} ln \frac{I_0}{I} \tag{3.7}$$

The previous expression is used to plot the absorption coefficient versus the wavelength of the incident radiation. To make a proper analysis of the fundamental absorption it is necessary to make two considerations:

1. The momentum of the photon is smaller than the momentum of the lattice. This means that is that in the process of absorption of a photon, the momentum of the electron involved must be conserved, that is why when an electron passes from a state in the valence band to another in the conduction band its energy increases, but not its momentum.
2. The material is assumed to be pure, and thus the absorption coefficient will exhibit the following behavior:

$$\alpha(\lambda) = \begin{cases} 0 \; if \; hv < E_g \\ \neq 0 \; if \; hv \geq E_g \end{cases} \tag{3.8}$$

Where h is the Planck's constant and ν is the frequency of the incident photon. In addition to previous considerations there are two types of transitions between bands that take place the fundamental absorption process:

a) Direct transition: The maximum and minimum of the valence and conduction band, respectively, coincide at the wave vector $\vec{k}$.
b) Indirect transition: The maximum and minimum of the valence and conduction band, respectively, does not coincide at the wave vector $\vec{k}$.

Figure 3.8 shows the absorption spectrum for a material with direct and indirect transitions.

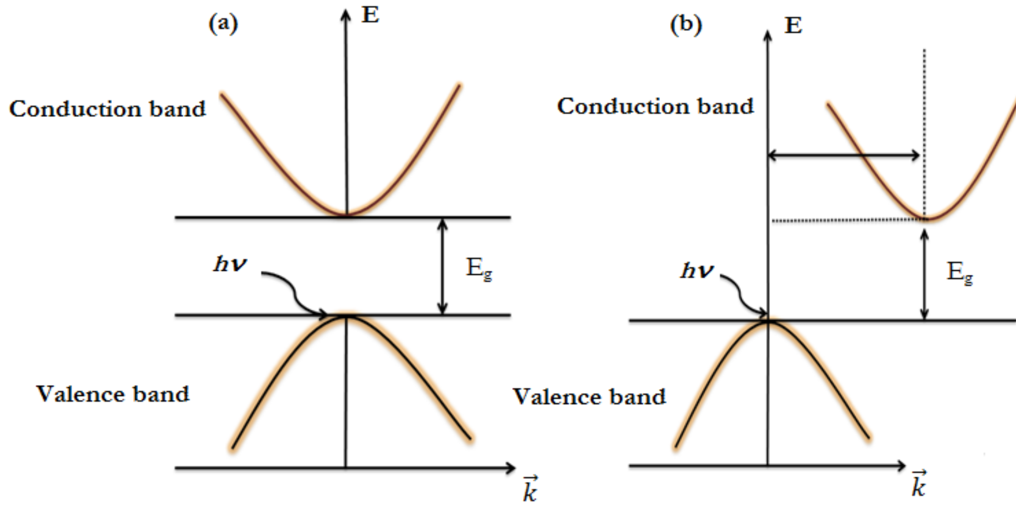

Figure 3.8 Scheme of a (a) direct and (b) indirect transition in a material.

The E_g value is obtained by extrapolating the linear portion of the α^2 graph against the energy of the incident photon. The following relations express the dependence of α with respect to the energy ($h\nu$) of the incident photonic radiation [1]:

$$\alpha(h\nu) = \begin{cases} A(h\nu - E_g)^{1/2} \\ A(h\nu - E_g)^2 \end{cases} \tag{3.9}$$

The first and second expressions in (3.9) apply for direct and indirect transitions, respectively. In both expressions α is the absorption coefficient, $h\nu$ is the energy of the incident photon, E_g the band gap energy and A is a constant that varies from material to material. It was previously mentioned that ZnO presented direct transitions; therefore the first expression in (3.9) will be used for the rest of this work.

By squaring the relation used for direct transitions a linear dependence of α^2 with respect to $h\nu$ is obtained:

$$\alpha^2(h\nu) = A^2(h\nu - E_g)^2 \tag{3.10}$$

The optical gap is obtained by extrapolating the linear portion of the curve described in the previous relation by finding the value of $h\nu$ where the condition $\alpha^2(h\nu) = 0$ is fulfilled.

3.7 Electrical characterization

The electrical properties of a material are as important as its optical ones; their characterization determines whether the studied material is a suitable candidate for a specific application, e.g., if a thin films has the enough conductivity to be used as an electrode, while more complex measurements can give further understanding of its electrical behavior. In this thesis the electrical characterization of the obtained thin films was carried out using the Van der Pauw and Hall Effect techniques, the former to measure the electrical resistivity and the latter to measure the carrier type, their density and mobility thereof. The aforementioned methods will be discussed in the following sections.

3.7.1 The Van Der Pauw technique

The van der Pauw technique measures both the volume resistivity (ρ) and sheet resistance (R_{PS}) of homogeneous planar materials, with an isotropic behavior and uniform thickness. To properly apply the Van Der Pauw technique four theoretically point-like ohmic (linear) contacts are placed on the periphery of the studied sample [11, 12] , as is shown in Figure 3.9. These points will be used to measure current and voltage values, therefore their delimitation is of high importance to carry out the measurement in a proper way.

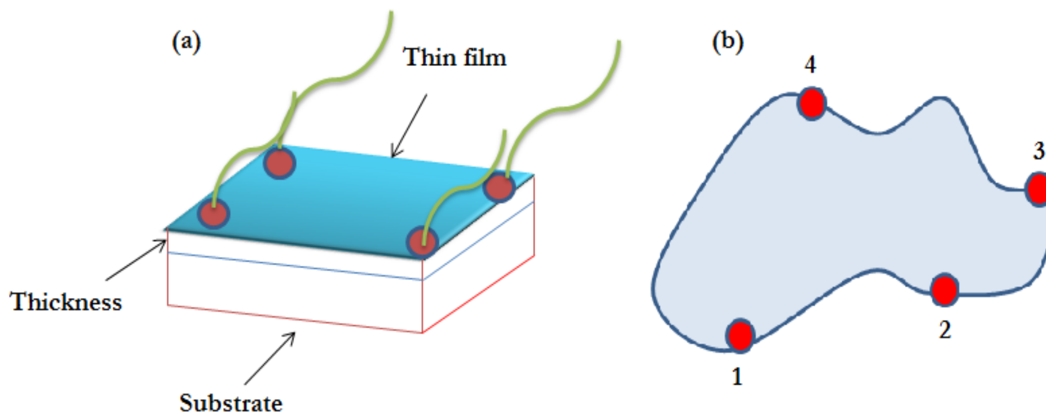

Figure 3.9 Two possible set-ups for the contacts on the Van der Pauw technique.

The electrical resistivity determination is as follows: the thin film is considered as a flat sheet free of imperfections and provided with 4 small contacts, 1, 2, 3 and 4, located in an arbitrary way. A current I_{12} will be applied at the periphery of the sample (Figure 3.9 b) on contacts 1 and 2, after this, the voltage between points 3 and 4 (V_4- V_3) is then measured. With the previous measurements a resistance value is defined as:

$$R_{12,34} = \frac{V_4 - V_3}{I_{12}} \quad (3.11)$$

In a similar way, another resistance value can be defined as:

$$R_{23,41} = \frac{V_1 - V_4}{I_{23}} \quad (3.12)$$

The Van Der Pauw theoretical background states that there is a relationship between the resistance values defined in (3.11) and (3.12) which is given by [11]:

$$exp\left(-\frac{\pi t}{\rho}R_{12,34}\right) + exp\left(-\frac{\pi t}{\rho}R_{23,41}\right) = 1 \tag{3.13}$$

Where t and ρ are the thickness and resistivity of the thin film, respectively. There are eight possible configurations that depend on the current direction and combination of contacts; this is shown in Figure 3.10.

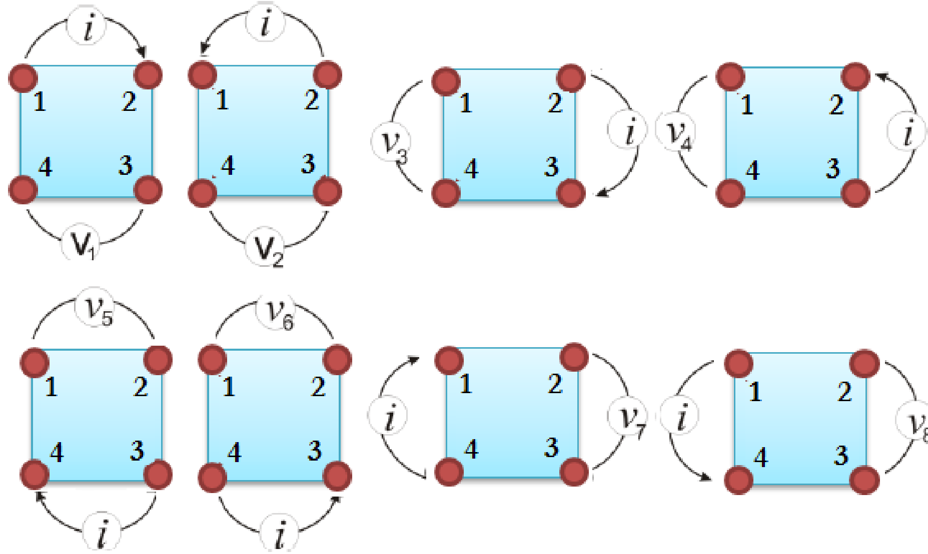

Figure 3.10 The eight possible configurations to measure resistivity.

Additionally, considering the symmetries between the contacts, with the measurement of the 8 voltages (V_1 to V_8) and with an average current value, two electrical resistivities can be determined for these configurations:

$$\boldsymbol{\rho_A = \frac{\pi f_A t}{4\, I \ln(2)}(V_2 + V_4 - V_1 - V_3)} \tag{3.14}$$

$$\boldsymbol{\rho_B = \frac{\pi f_B t}{4\, I \ln(2)}(V_6 + V_8 - V_5 - V_7)} \tag{3.15}$$

Where ρ_A and ρ_B are the resistivities in Ω cm, I is the applied average current, f_A and f_B are geometric factors that depend on the symmetry of the sample and are related by the two resistances (f_A = f_B = 1, for perfect symmetry). Finally, when ρ_A and ρ_B are known, the resistivity of the films can be determined as follows:

$$\boldsymbol{\rho = \frac{\rho_A + \rho_B}{2}} \tag{3.16}$$

3.7.2 Hall Effect technique

In order to measure the other electrical properties in thin films, i.e., carrier concentration n and its mobility μ the Hall Effect technique is employed. The basic physical principle underlying the Hall Effect

is the Lorentz force on the free charges. When an electric current circulates through conductive or semiconductor material while at the same time is placed perpendicularly to an external magnetic field B, the former exerts a transverse force on the charge carriers so that it makes them go towards a certain direction, resulting in an excess surface electrical charge on the side of the sample. As a result it is an electric field is generated, which compensates the influence of the Lorentz force [13, 14]. This leads to a potential difference between the two sides of the sample that can be measured as the Hall voltage V_H. If this magnetic field is variable, the slope of the magnetic field plotted against V_H can be obtained to determine carrier density as follows:

$$\boldsymbol{n = \frac{I}{et}\left(\frac{B}{V_{Hall}}\right)} \quad (3.17)$$

Where e is the fundamental electronic charge and t is the thickness of the sample. The quotient B/V_H is obtained by measuring the Hall voltage as a function of magnetic field and by determining the slope by linear regression between B and V_H. Furthermore, there is a simple relation between the mobility and electrical conductivity, which is:

$$\boldsymbol{\mu = \frac{1}{en\rho}} \quad (3.18)$$

Finally, the type of the electrical carriers (n or p), is obtained, depending on the resulting sign of the Hall's resistance R_H, which is [15]:

$$\boldsymbol{R_{Hall} = \frac{1}{ne} = \mu\rho} \quad (3.19)$$

3.8 References

[1] C. Kittel, Introduction to Solid State Physics 7th edn, John Wiley and Sons, New York, 1996.
[2] Seizo Morita, Franz J Giessibl, Ernst Meyer, Roland Wiesendanger, Meyer E. Noncontact Atomic Force Microscopy, Springer, Berlin Heidelberg New York, 1995.
[3] Fan Yang Max Shtein[a)] Stephen R. Forrest, Morphology control and material mixing by high-temperature organic vapor-phase deposition and its application to thin-film solar cells, Journal of Applied Physics 98 (2005) 014906.
[4] Joseph D. Andrade, X-ray Photoelectron Spectroscopy (XPS), Surface and Interfacial Aspects of Biomedical Polymers Volume 1 Surface Chemistry and Physics, Springer, New York, 1985.
[5] Sears F., Zemansky M., Young H., Freedman H., University Physics 6th ed., Addison-Wesley, United States, 1986.
[6] Briggs D., Grant J., Surface Analysis by Auger and X-ray Photoelectron Spectroscopy, IM-Publications, United Kingdom, 2003.
[7] J. H Scofield, Hartree-Slater subshell photoionization cross-sections at 1254 and 1487 eV, Journal of Electron Spectroscopy and Related Phenomena 8 (1976) 129-137.

[8] D. K. Schroder Semiconductor material and device characterization, second edition, A Wiley-Interscience publications, New York, 1998.

[9] Mariely Isabel Loeza Poot, Fabricación de celdas solares de CdTe usando una capa de CdS oxigenado (CdS:O), Master's Thesis, Centro de Investigación y de Estudios Avanzados del Instituto Politécnico Nacional Unidad Mérida, 2015.

[10] Hecht E., Optics 3rd edition, Addison Wesley, United States, 2000.

[11] L. J. Van der Pauw, A Method of Measuring Specific Resistivity and Hall Effect of Discs of Arbitrary Shapes, Philips Research Reports 13 (1958) 1-9

[12] L. J. Van der Pauw, A Method of Measuring the Resistivity and Hall Coefficient on Lamellae of Arbitrary Shape, Philips Research Reports 20 (1958) 220-224.

[13] E. H. Hall, On a New Action of the Magnet on Electrical Current, American Journal of Mathematics (1879) 287-292.

[14] S. C. Moulzolf, D. J. Frankel, R. J. Lad, In situ four-point conductivity and Hall Effect apparatus for vacuum and controlled atmosphere measurements of thin film materials, Review of Scientific Instruments 73 (2002) 2325.

[15] José Alfredo Marín Romero, Crecimiento por depósito de láser pulsado y caracterización de películas de ZnO no dopadas y dopadas con Al, Tesis Maestría Físico-Química, CINVESTAV IPN Mérida, 2012.

Chapter 4 Isoelectronic co-doping of Te and Cd in ZnO

This chapter describes the results obtained through an isoelectronic doping of ZnO thin films deposited by the pulsed laser technique (PLD), using pure a ZnO powder target mixed with CdTe. An analysis of the structural, morphological, and chemical properties is made. X-ray diffraction shows a single-phase hexagonal of ZnO wurtzite structure. The films showed a high transparency with an average range value between 70-80% in the visible region and a band gap value of ≈3.28 eV. X-ray photoelectron spectroscopy shows the formation of Zn–Te bonds, which demonstrates the occupation of O vacancies by Te atoms in the ZnO lattice, although Cd–Te and Te–O bonds were also present. Elemental analysis of the films gave Cd concentration lower than 2% in the ZnO film, likely due to low Cd solid solubility in ZnO. Crystallite size, film thickness, chemical concentrations and morphologic characteristics are also reported.

4.1 Isoelectronic impurities

Semiconductor materials are often fabricated by doping their crystal lattice with a small amount of a different element that belongs to another column of the periodic table, since elements that are located in different columns of the periodic table have different conduction number or outer shell electrons; this will cause their original electrical behavior to be changed [1]. For example, silicon which is an element of group IV is regularly doped with boron from group III material in order to make it suitable for its application in electronic devices. Alloys are often used to form a semiconductor material, i.e., substitutions on lattices sites by elements of the same group in the periodic table, to obtain any desire property for the semiconductor material, e.g., crystal lattice parameters, band gap, carrier mobility, among others [2]. Many technological devices based in semiconductor materials such as solar cells and light emitting diodes require materials with a direct band gap, since it facilities the absorption and conversion of light to electricity [3], therefore it is desired to use silicon to open the possibility of combining the advantages of the silicon integrated circuits with the benefits and capabilities of light, however, due to its indirect bang gap this has proven be a difficult task with limited success. As it was mentioned before solar cells are often elaborated using semiconductors of direct band gap, such materials are made of elements or combination of elements belonging to III and V groups of the periodic table, e.g., gallium (Ga), Indium (In), Arsenic (As) and Phosphorus (P), this elements are used to create junctions which become part of the solar cells, i.e., GaAs or InGaP. Other elements such as germanium (Ge), which belongs to group IV on the periodic table, are also integrated in other parts of the solar cells such as substrates; this is because in spite of its indirect band gap, the substrate can be made thick enough in order to absorb the adequate amount of light [2]. However, finding the suitable semiconductor materials for making a solar cell is a challenging question because there are not many acceptable materials that have the required properties, such as carrier mobility, carrier concentration, optical bang gap and lattice parameters that could be properly match to the other cell junctions based in the materials mentioned above, that is GaAs and Ge. One way to overcome this is by doping the semiconductor materials by adding small amounts of a different element, which in turn will attune the desired properties for its implementation in a solar cell or into another technological device.

Pure semiconductor materials, such as germanium and silicon have a tendency to be electrically intrinsic; this can be modified by adding an extrinsic element that acts as a dopant, for example, boron and phosphorus, which would incorporate into the semiconductor to make it either *n* or *p* type. The doping mechanisms in each of these processes are well understood, and are easy to control. Furthermore, there are several methods to achieve a successful doping, to name a few: diffusion [4], ion implantation [5], and in situ doping with epitaxial growth [6]. In spite of all aforementioned advantages, the doping processes in semiconductors based on compounds present many difficulties, one of them is the amphoteric nature of the dopants; which means that the electrical behavior in a semiconductor is determined by the position that doping materials occupy in the lattice site. In addition to this, compound semiconductor materials always present small imbalances in their stoichiometry between their constituent ions, which causes the electrical natures of one of the present materials to be more prevalent than the other, even before the incorporation of an external dopant [7]. This natural tendency to act either as an *n*-type or *p*-type semiconductor as grown makes it difficult for the doping process to produce a material with an opposite electrical behavior.

In the case of ZnO its crystals usually have oxygen deficiencies; this is because the oxygen atom is lighter than the zinc atom, besides having a higher vapor pressure during crystal growth. ZnO is partially ionic, this means that a material rich in zinc would have a natural n-type behavior. This is shown in Figure 4.1 (a) where the charge balance in a ZnO crystal produces a perfect stoichiometry; this would result in an intrinsic material in its electrical behavior. Figure 4.1 (b) shows a crystal where oxygen atom is removed from the crystalline lattice. The requirement for the crystal to be charge-balanced must still be met, thus, because the oxygen has a negative charge when it is in the ZnO crystal, the same negative charge must be left behind when the oxygen leaves the crystal. The left-behind negative charge does not have a localized state that confines it, and will end up in the conduction band, resulting in an *n*-type crystal.

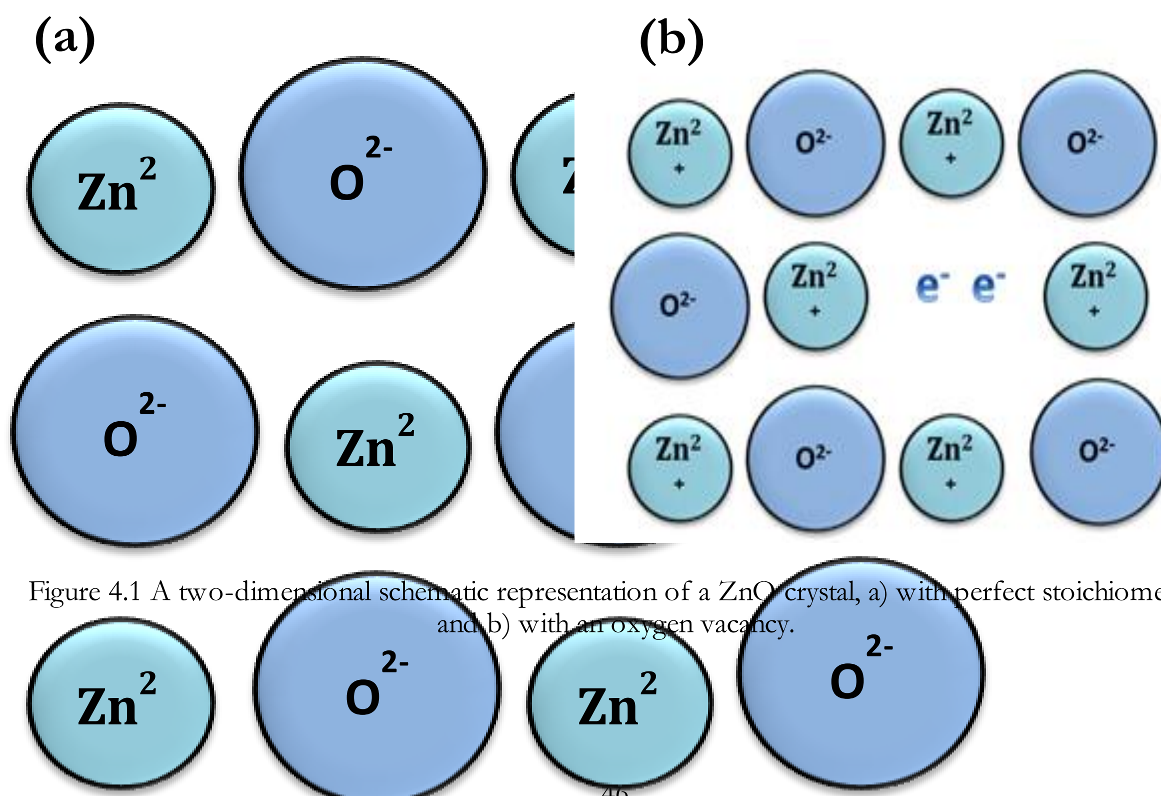

Figure 4.1 A two-dimensional schematic representation of a ZnO crystal, a) with perfect stoichiometry, and b) with an oxygen vacancy.

Other defects present in a ZnO crystal in addition to oxygen vacancies, are interstitial Zn atoms [8]; such defects make it difficult to prepare *p*-type ZnO, because they enhance an *n*-type electrical nature. One way of trying to passivate these defects is by isoelectronic doping, this means that the material that acts as a dopant impurity comes from the same column of the periodic table as the material to be doped, and as such, does not act with the same mechanism as a traditional dopant agent, therefore, it can be considered as a method for reducing the defect concentration. In many materials, people have shown that isoelectronic doping has definite effects of improving the crystalline quality in typical III–V and II–VI semiconductors such that deep levels, unintentional doping concentration, and dislocation density can be greatly reduced [9] recognized examples are nitrogen in GaP, indium in GaAs and Cd dichalcogenides.[9–12]. Group III-V compounds and alloys such as GaAs and GaP, are even isoelectronically co-doped with two different elements, for example N and Bi, in order to decrease their bandgaps, or modify their electrical properties such as their carrier concentration and mobility to customize many technological devices such as solar cells, light emitting diodes, photodetectors, lasers among others [13]. Additionally there are previous works in which it is reported that through an isoelectronic codoping of two different elements it is possible to achieve a *p*-type ZnO [14]. Regarding ZnO, several elements have been used for isoelectronic doping, but few works has been carried out using Te atoms [8,15,16]. Tellurium and cadmium atoms have the advantages of being isovalent respect O and Zn, respectively; this makes them candidates to be considered as passivating atoms that can also change the bandgap [17, 18] and the conductivity [19] in ZnO. The effect of Cd and Te doping can constitute an intermediate or parallel method for attaining *p*-type ZnO using other co-dopant element as nitrogen [19].

4.2 Experimental details

4.2.1 Target preparation

Two types of targets were prepared; the first target consisted of a mixture of CdTe with pure ZnO and the second one was made only with ZnO powder. The CdTe doped target was a solid disk with dimensions of 4.65 mm thick and 8.05 mm diameter, with an area of 50.3 mm^2, made up of a mixture of ZnO nanoparticles (99.99% Aldrich) with addition of 30 wt.% of CdTe (99.99% Aldrich). The target made of pure ZnO was prepared from ZnO powder had the same dimensions and was made from same ZnO nanoparticles. Both targets were milled, pressed to 10 tons for 5 minutes and sintered at 600 ºC for 2 hours.

4.2.2 Pulsed laser deposition and growth conditions

ZnO thin films were deposited on ITO/glass substrates using a Nd: YAG-laser operating in the Q-switch mode with λ = 1064 nm and 10 ns full width at half maximum at a repetition rate of 5 Hz. The Pulse energy was of ~300 mJ/pulse and the laser beam diameter was reduced to ~1.3 mm by means of a spherical quartz lens. The energy density of the beam on the target surface was ~2 Jcm^{-2}. During laser irradiation, the target was rotated at 30 rpm in order to avoid pitting of target at any given spot and to obtain uniform thin films. The laser was focused through a 50 cm focal length lens onto a rotating target at angle of incidence of 45º. The films were deposited at a substrate temperature of T_s= 300 ºC in a

vacuum of ~2.3×10^{-7} Pa. The film deposition is achieved with 3000 laser shots. Finally the target-substrate distance was kept at 50 mm.

4.2.3 Substrate preparation

The ITO/glass substrates were carefully cleaned in an ultrasonic bath for 10 minutes with acetone and methanol, rinsed in deionized water, and subsequently dried in air. Before deposition the substrate was maintained at T_s for 30 minutes and after deposition, the film was cooled to room temperature at a rate of 5 ºC min^{-1}.

4.2.4 Characterization techniques

The structural properties were determined using a D5000 Siemens X-ray diffractometer. The thickness of the films was measured by a Surface Profilometer Dektak-8, Veeco. The superficial morphology of the thin films was analyzed by atomic force microscopy (AFM) using a Park Scientific Instruments auto probe in the topography contact mode, with Si tips. The Elemental analysis of the films was carried out by energy dispersive spectroscopy (EDS) with a JEOL JSM 7600F scanning electron microscope. X-ray photo- electron spectroscopy (XPS) analyses were performed in a K- ALPHA Thermo Scientific System.

4.3 Results and discussions

4.3.1 X ray diffraction and profilometry results

Figure 4.2 shows X-ray diffractograms (XRD) for ZnO thin films grown from CdTe doped and undoped targets. The CdTe-doped ZnO films had thickness of ~112nm, similar to those of undoped ZnO. The observed diffraction peaks for both films are wurtzite ZnO phase [20], with preferential orientation in the plane (002). All the peaks are shifted to the left with respect to the position of the ZnO powder standard pattern, which indicates tensile stress [21]. From (100), (002) and (101) peaks, the average crystallite size was calculated from the Scherrer's formula [22], both calculations yield to similar results, namely, $D \approx (14 \text{ nm} \pm 1 \text{ nm})$ for undoped ZnO sample and $D \approx (12 \text{ nm} \pm 1 \text{ nm})$ for CdTe-doped ZnO sample. These results suggest that the introduction of Cd and Te had no significantly influence on the crystallite size.

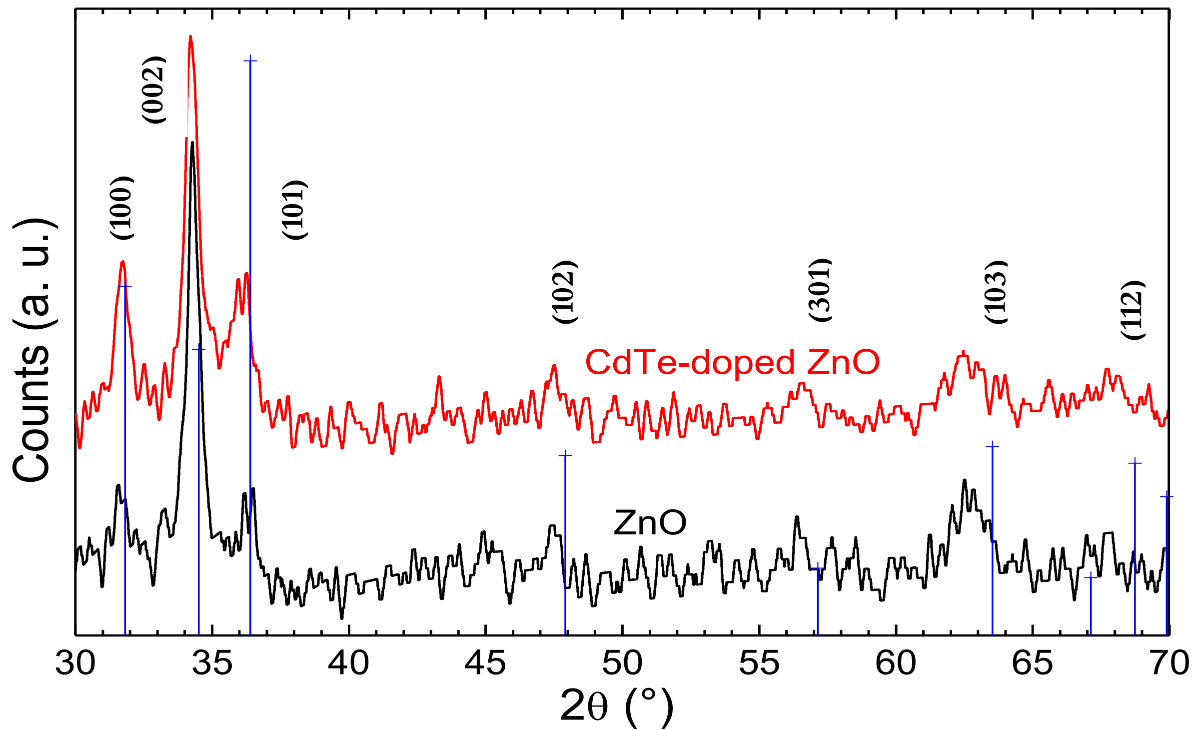

Figure 4.2 Diffractograms of the CdTe-doped (upper) and undoped ZnO (lower) thin films, respectively. The blue lines correspond to the standard pattern peaks.

4.3.2 Morphological analysis

Figure 4.3 displays 2D and 3D AFM images for the CdTe-doped ZnO films. The 2D images show big spheroidal grains in the surface with about 120 nm in diameter. The 2D AFM phase images display that below the big-grain layer there are grains of about 60 nm and smaller. The grain sizes observed in the AFM images are bigger than the calculated crystallite sizes obtained from the XRD data; this indicates that the grains are formed by nano domains. In the 3D AFM image, the spheroidal grains can also be observed, although it shows protruding grains, which break the surface regularity.

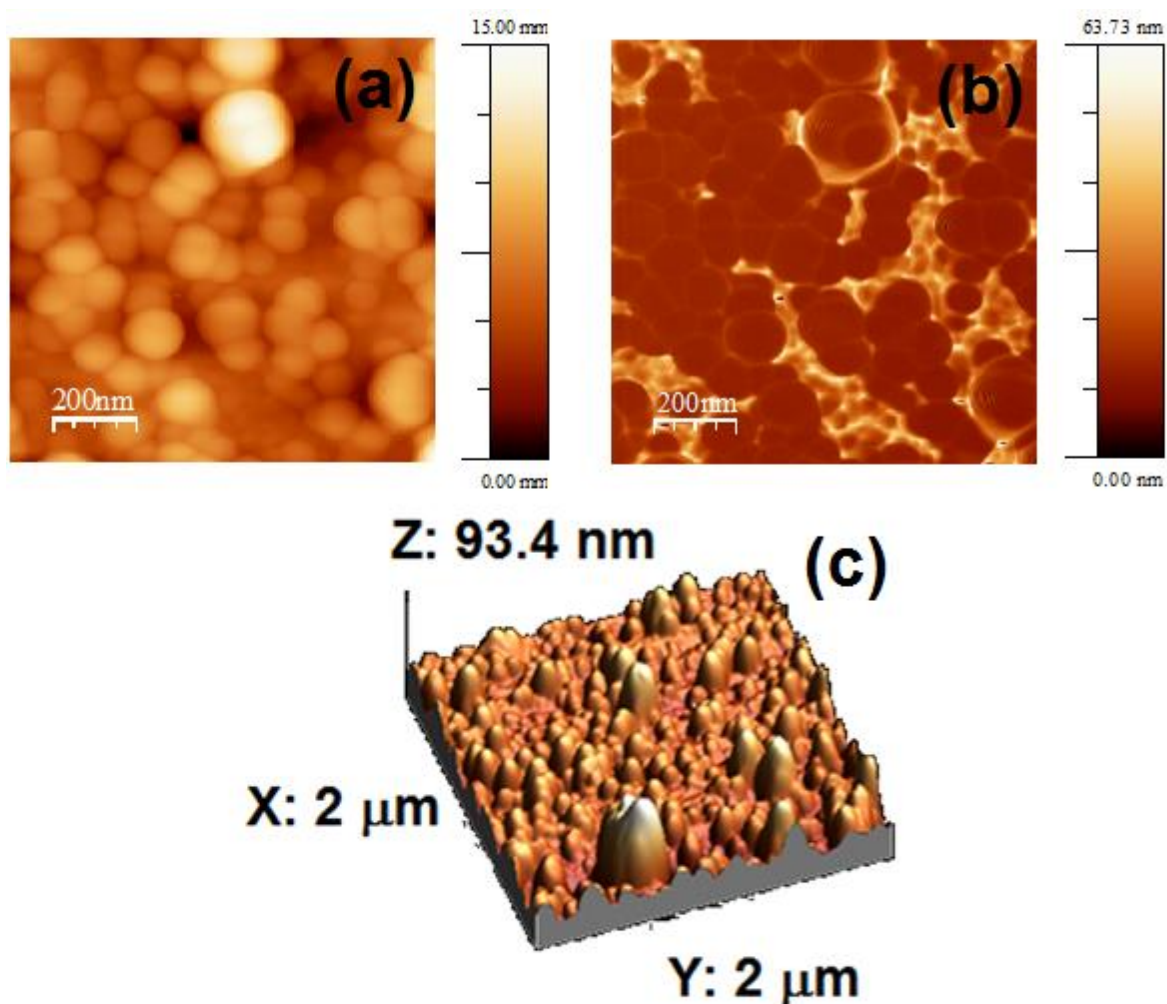

Figure 4.3 (a) 2D AFM image, (b) 2D AFM phase image and (c) 3D AFM image of the CdTe-doped ZnO film.

4.3.3 Chemical studies and bonding properties

The elemental composition of the samples such as Zn, Cd and Te was examined using EDS measurements. The EDS spectra for the CdTe-doped ZnO films are shown in Figure 4.4. The estimation of the quantitative weight and atomic percentage is presented in figure inset. The EDS measurements confirm the presence of Cd and Te in the ZnO, showing that in the surface the ratio Cd/Zn in at. % is around 2.5 % in contrast with a ratio Te/Zn of 10 %. The ratio Cd/Te in the film was about 25%. Taking into account that the target had stoichiometric CdTe, it means that a significant amount of Cd did not incorporate to the ZnO lattice. It is likely due to the low solid solubility of CdO in ZnO, reported to be about 2 at.% [23], which agrees with our experiment and to the Cd evaporation.

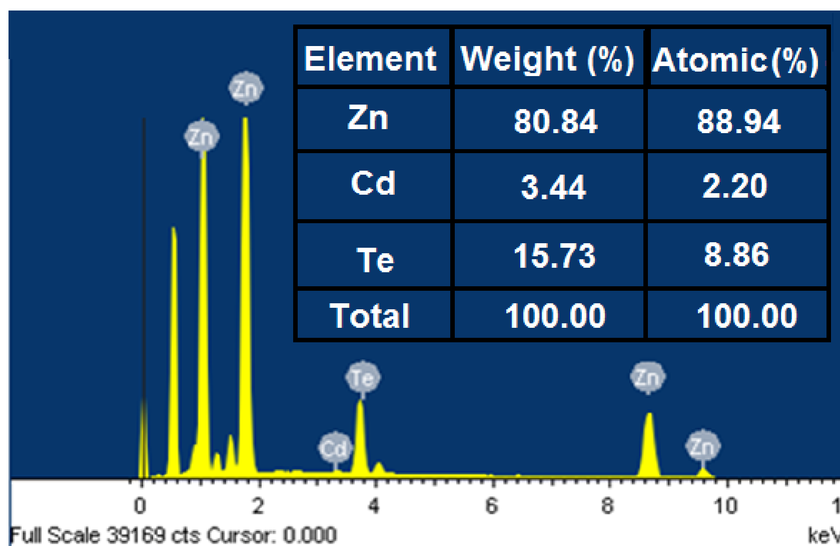

Element	Weight (%)	Atomic(%)
Zn	80.84	88.94
Cd	3.44	2.20
Te	15.73	8.86
Total	100.00	100.00

Figure 4.4 EDS results of the CdTe-doped ZnO thin films.

Figure 4.5 presents XPS survey spectra for the CdTe doped thin film. The C1s (284.6 eV) peak was employed as reference to calibrate the binding energies of all the examined elements, it shows the presence of Zn, O, Cd, Te and C, no other peaks corresponding to additional elements were observed, the typical peaks of ZnO are present [24, 25], the presence of the C1s peak in Figure 4.5 could be explained by the impurities originated due to the oils of the vacuum pumps employed in XPS measurement. The Zn: O ratio on the sample surface in atom% was 60: 40. Figure 4.6 (a) presents the Zn 2p core level XPS scan, using a higher resolution and a smaller energy window. The Zn 2p core level XPS spectrum shows the presence of two sharp peaks at 1021.7 eV (Zn $2p_{3/2}$) and 1045.2 eV (Zn $2p_{1/2}$) and correspond to zinc present as ZnO [26].

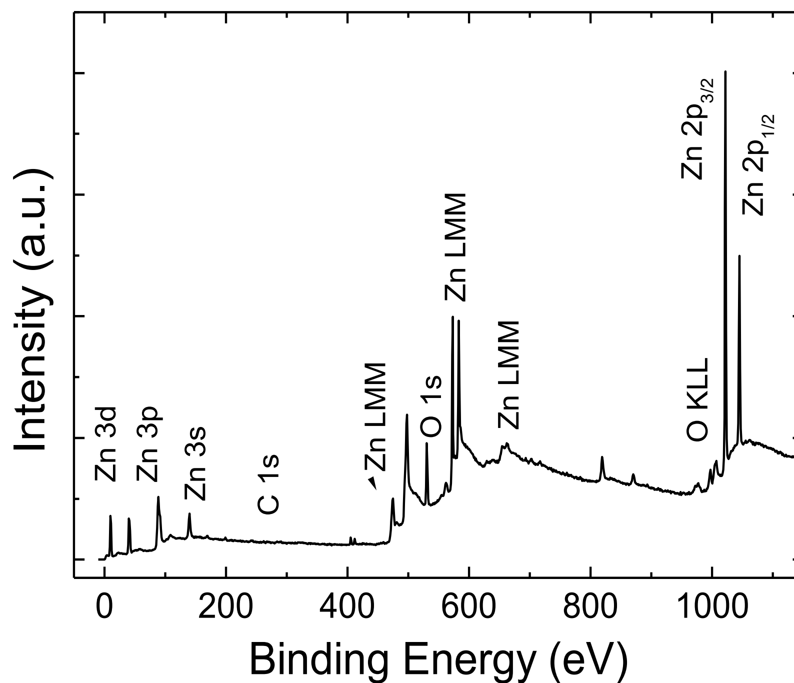

Figure 4.5 XPS survey spectrum of the CdTe doped ZnO thin films.

Figure 4.6 (b) shows the O 1s core level scan. The O 1s peaks have a shoulder at higher binding energies; these two peaks were fitted into two peaks by a Lorentzian distribution adjustment. The peak with low binding energy (530.30 eV) corresponds to O^{2-} on normal wurtzite structure of ZnO single crystal [27]. Another peak centered at 532.01 eV is attributed to O^{2-} in the oxygen deficient regions within the matrix of ZnO [28]. Other small peaks different from those belonging to the ZnO, can be also observed, as shown in Figure 4.6 (c), in the region from 36 to 46 eV, some lines corresponding to the binding energies of Te $4d_{5/2}$ in ZnTe (40.1 eV) and CdTe (41.9 eV) are shown, which were fitted using a Gaussian deconvolution adjustment. In the region between 565 and 590 eV, the Te–Zn and Te–O binding energy peaks are present, as shown in Figure 4.6 (d), Te $3d_{5/2}$ and Te $3d_{3/2}$ peaks in ZnTe for the sample appear at the binding energies of 572.7 and 583.1eV, respectively. The same peaks in tellurium oxide, TeO_x, appear at 575.1 and 585.4 eV.

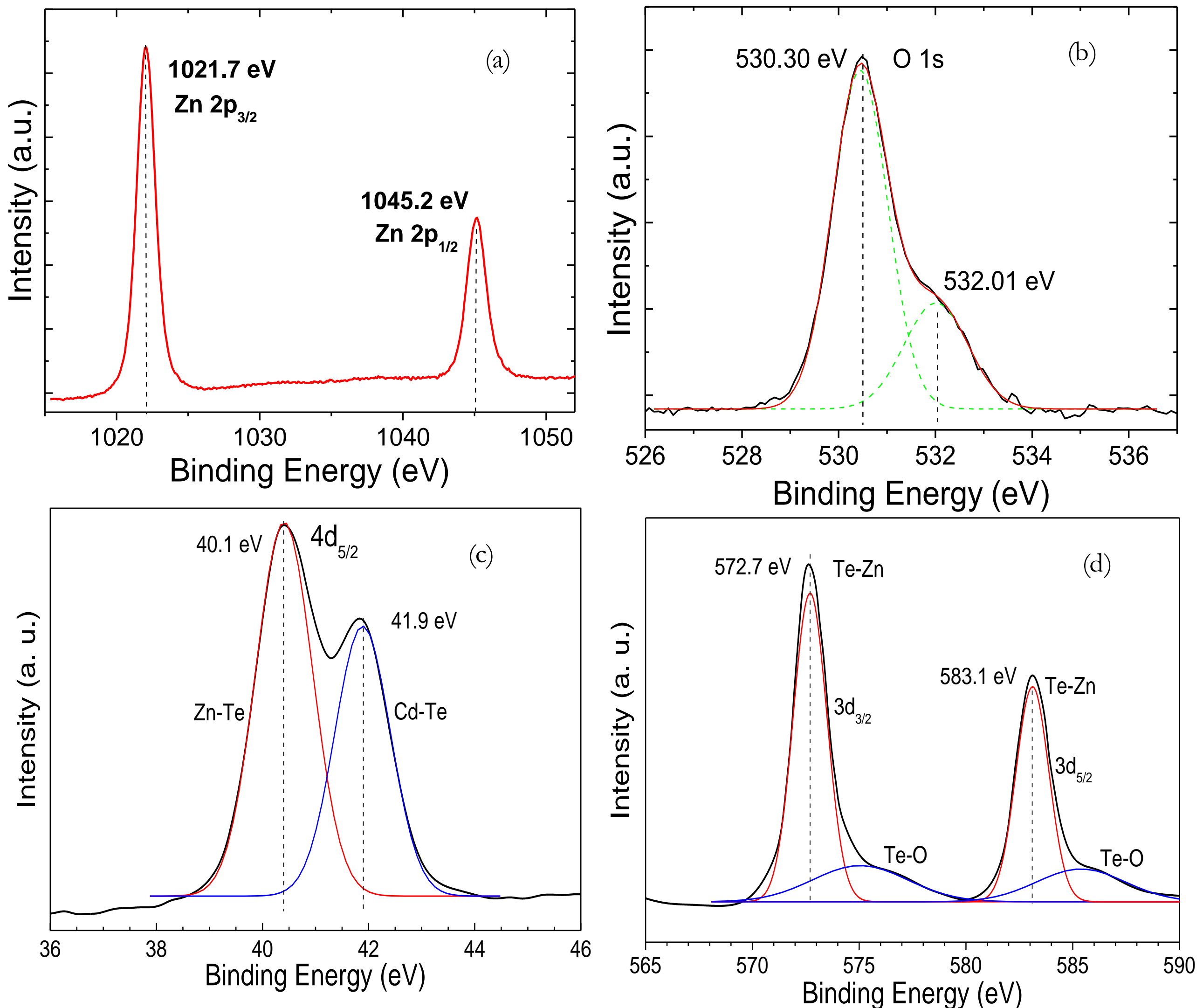

Figure 4.6 XPS spectrum of the CdTe doped ZnO thin films. Binding energy spectrum of (a) Zn 2p, (b) O 1s, (c) Te $4d_{5/2}$ and 3d (d).

Using the ratio between the XPS spectrum areas and associating all the values we calculated that the concentrations of the compounds other than ZnO are 48–49% of ZnTe, 33–34% of CdTe and 16–20% of TeO_x. No Cd–O bonds could be discriminated from XPS measurements likely due to the small

amount of Cd incorporated to the ZnO lattice. Our results evidence that most of the Te atoms incorporate into the O sites in the ZnO lattice, a significant part of Te remains as residual CdTe or in a $Cd_xZn_{1-x}O_{1-y}Te_y$ compound, and a lower amount of Te forms oxides.

4.3.4 Optical analysis

The optical properties of the CdTe-doped ZnO films were determined with optical transmission measurements in the range of 300 to 900 nm; these are shown in Figure 4.7. All samples presented a high transparency in the visible region (400-800 nm), with the average transmission value being in the range of 70-80%, which agrees with previous works where it is reported that films with similar transmittance values are considered of good optical quality [29].

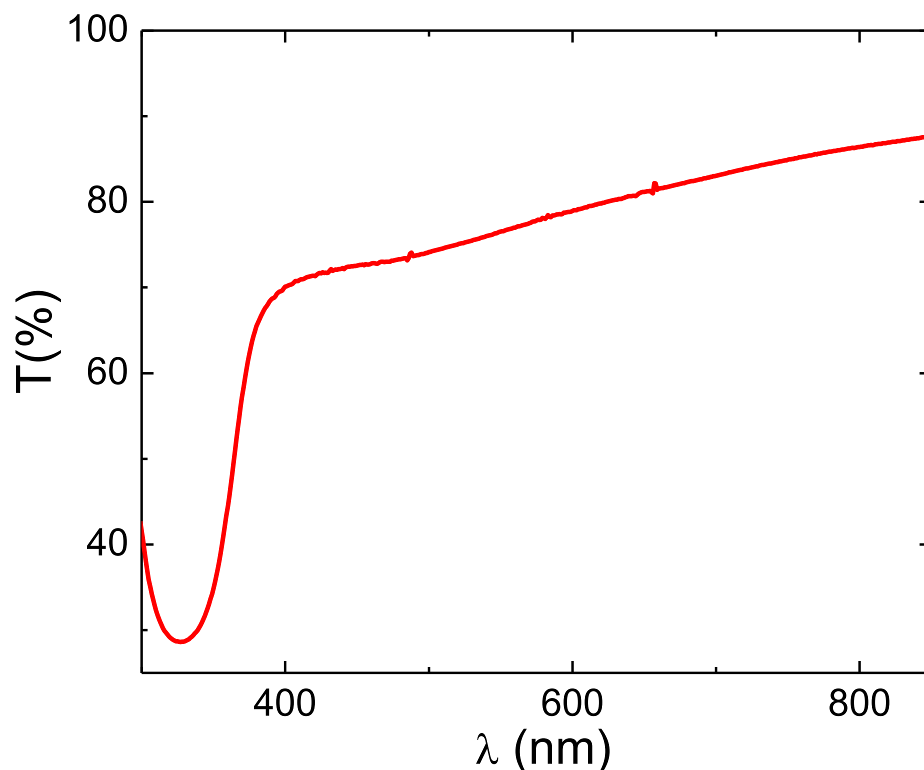

Figure 4.7 Optical transmittance spectra of the CdTe-doped ZnO thin films.

The optical transmittance was used to calculate the absorption coefficient (α) for the deposited films. The following equation was employed to carry out the calculation [30].

$$\alpha = -\left(\frac{1}{d}\right)\ln(T) \qquad (4.1)$$

Where T is the normalized transmittance and d is the sample thickness. Once the absorption coefficient is obtained, it can be used to determine the optical band gap. The band gap (E_g) was determined assuming direct transitions between the conduction and valence band using an extrapolation of the linear portion of the α^2 versus hv plot in the following equation: [31]

$$(\alpha hv) = A\left(hv - E_g\right)^{1/2} \qquad (4.2)$$

Where A is a constant, $h\nu$ is the photon energy and E_g the optical band-gap energy. The $(\alpha h\nu)^2$ versus $h\nu$ plot is shown in Fig. 4.8.

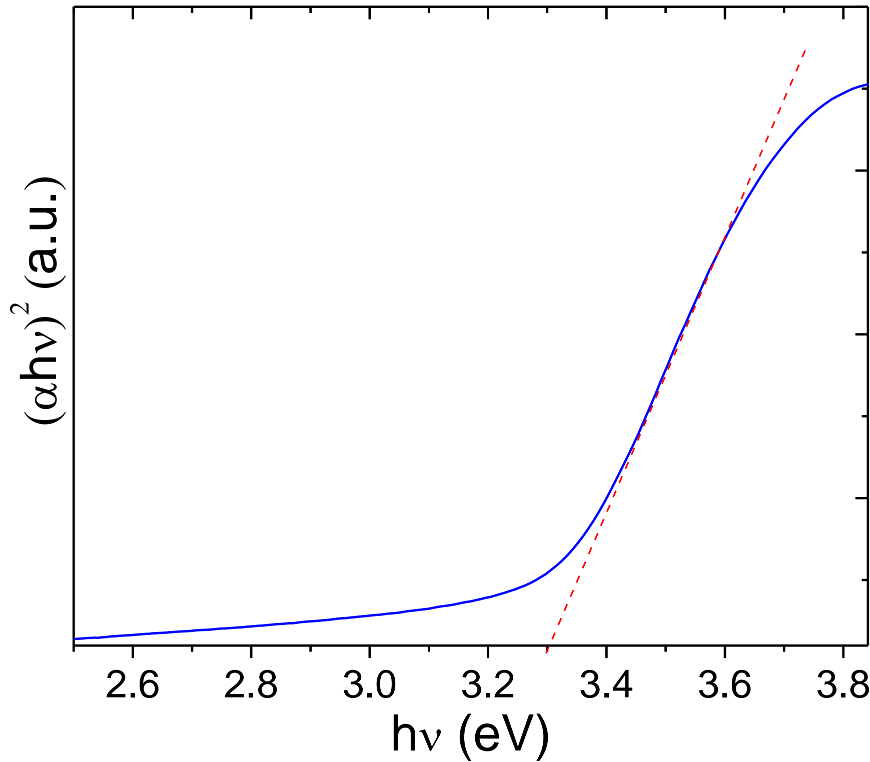

Figure 4.8 $(\alpha h\nu)^2$ vs. $h\nu$ curves of the CdTe-doped ZnO thin films.

The calculated optical band gap value for the CdTe-doped ZnO thin films was approximately ~3.28 eV, which is very close to the band gap of intrinsic ZnO powder and is in good agreement with the literature reports. [32]

4.4 Partial conclusions

Hexagonal ZnO single-phase polycrystalline films with variable, but spheroidal grains were grown by the PLD technique from sintered target made from mixed powders of CdTe and ZnO. The presence of Zn–Te bonds confirms the isoelectronic doping of Te atoms in O sites. The presence of Cd–Te bonds can indicate the existence of residual CdTe clusters or the formation of the solid solution of $Cd_xZn_{1-x}O_{1-y}Te_y$. The presence of Te–O bonds reveals Te oxidation. Cd in the film was found in amount much lower than Te likely due to its low solid solubility and evaporation.

4.5 References

[1] Kittel Charles, Introduction to Solid State Physics. 8a edition, John Wiley & Sons, 2005.

[2] Mascarenhas, Angelo, Isoelectronic Co-doping. Midwest Research Institute, assignee. Patent US 6815736B2. 9 Nov. 2004.

[3] Olson, Jerry, Sarah Kurtz, and Daniel Friedman. Multi-junction, Monolithic Solar Cell Using Low-band-gap Materials Lattice Matched to GaAs or Ge. Midwest Research Institute, assignee. Patent US6281426 B1. 28 Aug. 2001.

[4] C Y Ouyang, S Q Shi, Z X Wang, H Li, X J Huang and L Q Chen. The effect of Cr doping on Li ion diffusion in $LiFePO_4$ from first principles investigations and Monte Carlo simulations, Journal of Physics: Condensed Matter 16 (2004) 2265-2272

[5] Andrei Ghicov , Jan M.Macak , Hiroaki Tsuchiya , Julia Kunze , Volker Haeublein , Lothar Frey , and Patrik Schmuki , Ion Implantation and Annealing for an Efficient N-Doping of TiO_2 Nanotubes, Nano Letters 6 (2006) 1080–1082.

[6] B. Vincent, F. Gencarelli, H. Bender, C. Merckling, B. Douhard, Undoped and in-situ B doped GeSn epitaxial growth on Ge by atmospheric pressure-chemical vapor deposition, Applied Physics Letters 99 (2016) 152103.

[7] N. K. Abrikosov, V. F. Bankina, L. V. Poretskaya, L. E. Sheliova, and E. V. Skudnova, Semiconducting II-VI, IV-VI, and V-VI Compounds, 1st ed. New York: Plenum Press, 1969.

[8] Iribarren A, Fernández P, Piqueras J. Cathodoluminescence characterization of ZnO:Te microstructures obtained with ZnTe and TeO_2 doping precursors. Superlattice and Microstructures 43 (2008); 600–604.

[9] C. K. Shu, J. Ou, H. C. Lin, W. K. Chen, and M. C. Lee, Isoelectronic In-doping effect in GaN films grown by metalorganic chemical vapor deposition, Applied Physics Letters 73 (1998) 641-643.

[10] D. R. Scifres, N. Holonyak, Jr., C. B. Duke, G. G. Kleiman, A. B. Kunz, M. G. Craford, W. O. Groves, and A. H. Herzog, Photoluminescence Associated with Multivalley Resonant Impurity States above the Fundamental Band Edge: N Isoelectronic Traps in GaAs1-xPx, Physical Review Letters 27, (1971) 192-194.

[11] K. Akimoto, H. Okuyama, M. Ikeda, and Y. Mori, Isoelectronic oxygen in II-VI semiconductors, Applied Physics Letters 60 (1992) 91-93.

[12] H. Beneking, P. Narozny, and N. Emeis, High quality epitaxial GaAs and InP wafers by isoelectronic doping, Applied Physics Letters 47 (1985) 828-830.

[13] S. Francoeur, M.-J. Seong, A. Mascarenhas, S. Tixier, M. Adamcyk, T. Tiedje, Band gap of $GaAs_{1-x}Bi_x$, $0<x<3.6\%$. Applied Physics Letters 82 (2003) 3874-3876.

[14] Seung-Hwan Park, Tsutomu Minegishi, Dong-Cheol Oh, Dong-Jin Kim, Ji-Ho Chang, Takafumi Yao, Toshinori Taishi, and Ichiro Yonenaga, Influence of Isoelectronic Te Doping on the Physical Properties of ZnO Films Grown by Molecular-Beam Epitaxy, Japanese Journal of Applied Physics 52 (2013)5-8.

[15] Seung-Hwan Park, Minegishi Tsutomu, Oh Dong-Cheol, Chang Ji-Ho, Yao Takafumi, Taishi Toshinori, Yonenaga Ichiro. P-type conductivity control of hetero epitaxially grown ZnO films by N and Te codoping and thermal annealing. Journal of Crystal Growth 363 (2013) 190–194.

[16] Farid Jamali-Sheini Ramin Yousefi, Mahmoudian MR, Bakr Nabeel Ali.Abdolhossein Saaedi, Nay Ming Huang, Facile synthesis of different morphologies of Te-doped ZnO nanostructures. Ceramics International 40 (2014) 7737–7743.

[17] Gondek E, Djaoued Y, Priya S, Balaji S, Robichaud J, Karasiński P, Organic hybrid solar cells—Influence of ZnO nano-particles on the photovoltaic efficiency. Material Letters 131 (2014) 259–261.

[18] Debbichi M, Souissi M, Fouzri A, Schmerber G, Said M, Alouani M., Room temperature ferromagnetism in Cd-doped ZnO thin films through defect engineering, Journal of Alloy and Compounds 598 (2014)120–125.
[19] Xin Tang Haifeng Lü, Zhang Qingyu, Zhao Jijun, Lin Yuyuan. Study on interactions between Cadmium and defects in Cd-doped ZnO by first-principle calculations, Solid State Science 13 (2011) 384–387.
[20] 2003 JCPDS-International Centre for Diffraction Data. PCPDF WIN v.2.4.Chart No. 36-1451.
[21] Zak A K, Majid W H A, Abrishami M E, Yousefi R. X-ray analysis of ZnO nanoparticles by Williamson-Hall and size-strain plot methods, Solid State Sciences 13 (2011) 251-256.
[22] Cullity BD. Elements of x-ray diffraction. Reading, MA: Addison Wesley Publishing Inc; 1956.
[23] Karunakaran C, Vijayabalan A, Manikandan G. Photocatalytic and bactericidal activities of hydrothermally synthesized nanocrystalline Cd-doped ZnO. Superlattice and Microstructures 51 (2012) 443–453.
[24] NISTX-ray Photoelectron Spectroscopy Database,Version4.1 (National Institute of Standards and Technology, Gaithersburg (2012), ⟨http://srdata.nist.gov/xps/⟩.
[25] Jianting He Boxue Tan, Wei Qinqin, Su Yuanbin, Yang Shulian. Growth and characterization of ZnO thin films grown by pulsed laser deposition. Advanced Material Research 383(2012) 6289–6292.
[26] Xuebin Wang, Kaifu Huo, Fan Zhang, Zheng Hu, Paul K. Chu, Haisheng Tao, Qiang Wu, Yemin Hu, Jianmin Zhu, Structural Regulation and Optical Properties of One-Dimensional ZnO Nanomaterials in Situ Grown from and on Brass Substrates , Journal of Physical Chemistry C 113 (2009) 170–173.
[27] B.J. Coppa, R.F. Davis, R.J. Nemanich, Gold Schottky contacts on oxygen plasma-treated, n-type ZnO (0001), Applied Physics Letters 82 (2003) 400-402
[28] M. Chen, X. Wang, Y.H. Yu, Z.L. Pei, X.D. Bei, C. Sun, R.F. Huang, L.S. Wen, -ray photoelectron spectroscopy and auger electron spectroscopy studies of Al-doped ZnO films, Applied Surface Science 158 (2000)134-140.
[29] Liwei Wang, Lijian Meng, Vasco Teixeira, Shigeng Song, Zheng Xu, Xurong Xu, Structure and optical properties of ZnO:V thin films with different doping concentrations, Thin Solid Films 517 (2009) 3721–3725.
[30] S. T. Tan, B. J. Chen, X. W. Sun, W. J. Fan, H. S. Kwok, X. H. Zhang and S. J. Chua, Blue shift of optical band gap in ZnO thin films grown by metal-organic chemical-vapor deposition, Journal of Applied Physics 98 (2005) 013505.
[31] Davood Raoufi,Taha Raoufi, The effect of heat treatment on the physical properties of sol–gel derived ZnO thin films, Applied Surface Science 255 (2009) 5812–5817.
[32] Satish C. Rai, Kai Wang, Yong Ding, Jason K. Marmon, Manish Bhatt, Yong Zhang, Weilie Zhou, and Zhong Lin Wang, Piezo-phototronic Effect Enhanced UV/Visible Photodetector Based on Fully Wide Band Gap Type-II ZnO/ZnS Core/Shell Nanowire Array, ACS Nano 9 (2015) 6419–6427.

Chapter 5 Nitrogen doped ZnO thin films grown from hybrid target by the laser ablation technique

ZnO thin films were deposited on glass substrates by the pulsed laser deposition (PLD) technique using two different kinds of targets. One of the targets was made of pure ZnO powder and the other one was a hybrid target which consisted of a mixture of ZnO powder embedded into a polyethyl cyanoacrylate matrix. The resulting thin films were polycrystalline and presented a ZnO wurtzite structure with very low stress having preferential orientations in the planes (100) and (101); also the obtained diffractograms were very similar to those of the standard powder pattern. From comparing with ZnO thin films grown from traditional sintered target, it is suggested that the use of this hybrid target with a soft matrix led to ejection of ZnO clusters that conveniently disposed and adhered to substrate and previous deposited layers. Chemical measurements showed the presence of Zn–N bonds, besides Zn–O ones. Regarding their optoelectronic properties, the films deposited with the mixture powder target had a high transmittance in the range of 70-90% in the 540 to 850 nm wavelength region and showed a high resistivity of $\sim 10^5\ \Omega$ cm. The Optical absorption profile confirmed the presence of low-polymerized zinc oxynitride molecular subunits, besides ZnO. The structural and morphological properties of the films obtained using both targets were compared in order to determine which one produces samples with properties more suitable for their use as buffer and antireflective layer in CdTe based solar cells.

5.1 Strategies to modify the conductivity of ZnO thin films

5.1.1 The problem of p-doping ZnO

In optoelectronics and photovoltaics applications, ZnO can be used as transparent conductor oxide (TCOs) as a low cost alternative to tin-doped indium oxide (ITO) and as a buffer and antireflective layer within the glass/ITO/ZnO/CdS/CdTe solar cell heterostructure [1]. Even in hybrid photovoltaics [2], ZnO can act as an efficient electron acceptor [3]. Additionally the semiconductors based on ZnO have drawn much attention because of the many multifunctional properties that the ZnO offers, those properties could lead to the development of great amount technological devices, such as high-temperature electronics, transparent electronics, and blue to UV optoelectronics [4].

In the aforementioned applications it is mandatory to achieve both a high quality *n*-type and *p*-type doping, which is required for the construction of *p–n* based ZnO homojunctions. However there are many complications which make the *p*-type doping for the ZnO troublesome to accomplish, this avoids the successful development of electronic and photonic applications based on ZnO [5–7]. There are numerous reasons behind this doping difficulty, namely the self-compensation effect due to the presence of native defects such as oxygen vacancies and zinc interstitials [7]. Also many dopants present very low carrier concentration because of their low solubility and deep acceptor levels; this makes fabricating a *p*-type ZnO even harder [8]. Many researcher groups have tried to grow ZnO with reproducible and good quality *p*-type doping, some of them have reported successfully employing V group elements, such as N [9, 10], P [11, 12], As [13] and Sb [8]) and other elements such as Li [14] as *p*-type dopants. There are works where a dual-doping method is employed which consists in using two acceptor agents (e.g., Li–

N [15, 16] or N–As [17]). Among these many elements and methods, the doping using N is considered the best candidate for an effective *p*-type doping of the ZnO, since the O and N ionic radius are similar, thereby leading to the elimination of the self-compensation effect caused by the O vacancies and zinc interstitials [7]. Moreover results of first-principles total-energy calculations predict that N is the best candidate for *p*-type ZnO doping because of the small strain effects and shallow acceptor levels of substitution of N for O [18].

5.1.2 Nitrogen doping of ZnO by cyanoacrylate glue using laser ablation

Although a reproducible low resistance and high mobility *p*-type ZnO film has not been successfully obtained and also the effective incorporation of nitrogen in substitution of oxygen remains difficult, there are a lot of deposition techniques for obtaining *p*-type doping in ZnO thin films. To name a few: molecular beam epitaxy [8, 9], radio-frequency magnetron sputtering [19], ion-implantation [20], wet chemical deposition [4], chemical vapor deposition [21], thermal oxidation [7], pulsed laser deposition [6, 13, 22] and many others. All of previous mentioned techniques present a varied degree of success in obtaining the desired *p*-type doping, among them, the PLD method is widely employed to obtain ZnO thin films; this is due to the fact that it presents the advantages of allowing to deposit at a relatively low substrate temperature, deposition in controlled reactive gas pressure and high deposition rates. All these properties taken together enable sufficient control of film composition, and film properties [23]. One of the recent applications of the PLD technique is its using with hybrid and organic targets [24]. Organic and hybrid materials suffer the disadvantage of decomposition during ablation due to the high energy that is liberated during the deposition process, to solve this issue there are new laser techniques being developed, to name a few: matrix assisted pulsed laser evaporation (MAPLE), resonant infra-red (RIR) PLD, and other techniques where sometimes freezing the target is required [25, 26]. However, it's still possible to employ conventional PLD with hybrid and organic targets [27].

Cyanoacrylate based compounds (CA's) are a group of very strong organic glues employed in many industrial applications, such as sealants, coatings, and adhesives for gluing a variety of substrates [28]. CA's are very suitable for bonding applications in high-throughput and fast cycle manufacturing and have low toxicity. One of the CAs is the ethyl-2-cyanoacrylate ($C_5H_5NO_2$), ECA, commonly called "Super Glue," which polymerizes very fast in the presence of moisture. The ECA 2D structure is shown in Figure 5.1. The ECA boiling point is at 54–56 °C, its flash point is at 75 °C, and it softens at temperature above 150 °C after it cures. Under heating, ECA can decompose emitting vapors of CO_2 and nitrogen oxides, formaldehydes and could likely include some hydrogen cyanide [29, 30]. ECA has been used as adhesive matrix in applications other than individual gluing surfaces [31]. Taking into account the ECA properties, its nitrogen content, its capacity of agglutinating, affordability, and cost, it is a suitable material for preparing targets to be used in the PLD technique and attaining N doping. There are other compounds with higher N content. However, they do not have all the ECA advantages, being the aforementioned properties the reasons to select ECA as our choice for making the hybrid target.

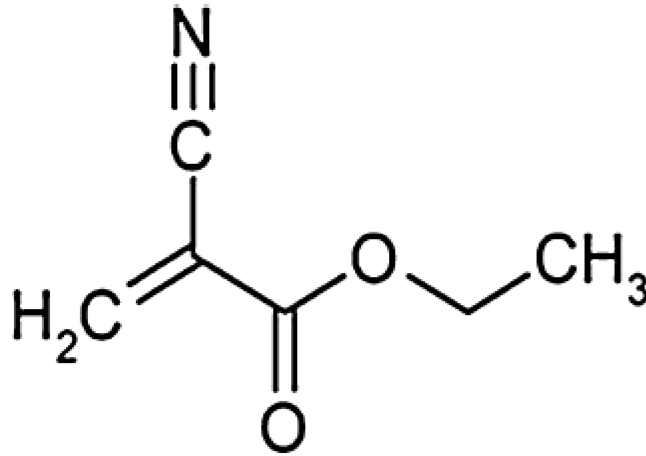

Figure 5.1 Chemical structure of the Ethyl 2- Cyanoacrylate.

In this chapter we study the structural, morphological, chemical, electrical, and optical properties of ZnO thin films deposited by the Nd: YAG-laser ablation technique using a hybrid target (HT) made of ZnO nanoparticles embedded into ECA Super Glue. We compare the HT results with those of the ZnO thin films deposited using a traditional sintered target made of ZnO powder. With this procedure we found that nitrogen from the ECA decomposition reacts with ZnO to achieve the formation of zinc oxynitride. Subsequently we found that the thin films grown with the cyanoacrylate glue target had superior properties that made them more suitable to be potentially used in CdTe solar cells as a buffer and antireflective layer than the thin films from a traditional target.

5.2 Experimental details

5.2.1 Target preparation

The mixed target (hybrid target) was made up of ZnO powder (99.999% Cerac) nanoparticles with a size less than 100 nm mixed with commercial Loctite 495 CA Super Glue, mainly composed by ethyl 2-cyanoacrylate (ECA). The mixture of ECA and ZnO powder (mixed target) was made with nominal ratio of 70:30 wt%, (being the ZnO the compound which was present in a greater proportion) and dried during 72 hours at room temperature. The target made of pure ZnO was prepared from ZnO powder, which was subjected to a pressure of ten tons during 5 minutes and after that was placed in a furnace at 600 °C during 2 hours; this process is called sintering (Sintered target). The targets were shaped as solid disks of 5 mm thick and 15 mm diameter

5.2.2 Pulsed laser deposition and growth conditions

ZnO thin films were deposited on ITO/glass substrates using a Nd: YAG-laser operating in the Q-switch mode with λ = 1064 nm and 10 ns full width at half maximum at a repetition rate of 5 Hz. The pulse energy was of ~300 mJ/pulse and the laser beam diameter was reduced to ~1.3 mm by means of a spherical quartz lens. The energy density of the beam on the target surface was ~2 Jcm^{-2}. During laser irradiation, the target was rotated at 30 rpm. The laser was focused through a 50 cm focal length lens onto a rotating target at angle of incidence of 45°. The films were deposited at a substrate temperature of T_s=

300 ºC in a vacuum of ~1.3×10^{-7} Pa. The film deposition is achieved with 3000 laser shots. Finally the target-substrate distance was 40 mm.

5.2.3 Substrate preparation

The ITO/glass substrates were cleaned in an ultrasonic bath for 10 minutes with acetone and finally with methanol. Before deposition the substrate was maintained at T_s for 30 minutes and after deposition, the film was cooled to room temperature at a rate of 5 ºCmin^{-1}.

5.2.4 Characterization techniques

The structural properties were determined by measurements in the grazing incidence geometry using a D5000 Siemens X-ray Diffractometer with CuKα filtered monochromatic radiation (λ =0.15418 nm) at 40 kV with 35 mA and aperture diaphragm of 0.2 mm. The diffractograms were registered in the step scan mode with a beam incidence angle of 1º and recorded in 2θ = 0.02º steps with a step time of 10 seconds in a 2θ range of 30-70º. The superficial morphology of the thin films was analyzed by atomic force microscopy (AFM) using a Park Scientific Instruments auto probe in the topography contact mode, with Si tips. The cross sectional morphology and surface of the obtained samples were studied by using a field emission scanning electron microscope (FESEM) JEOL 7600F instrument. The thicknesses of the films were measured by a surface Profilometer Dektak-Veeco. A K-ALPHA Thermo Scientific System was used for performing X-ray photo-electron spectroscopy (XPS) analyses. Optical transmittance measurements in the range of 350–800 nm were performed with an Agilent 8453 UV-visible Spectroscopy System, the optical band gap was calculated taking into account only direct transitions. The Resistivity values were obtained with an Ecopia HMS-5000 Van der Pauw Measurement System at room temperature.

5.3 Results and discussions

5.3.1 Structural studies

Figure 5.2 shows X-ray diffractograms (XRD) for ZnO thin films grown from hybrid and sintered targets. The XRD measurements indicate that a single-phase hexagonal and only ZnO wurtzite structure peaks are present [32]. The diffractogram of the HT sample obtained shows preferential orientation in the planes (100) and (101) parallel to substrate and at least for the three main peaks (100), (002), and (101), it agrees with those of ZnO pattern. The diffractogram of the ST sample shows preferential orientation in the (002) plane.

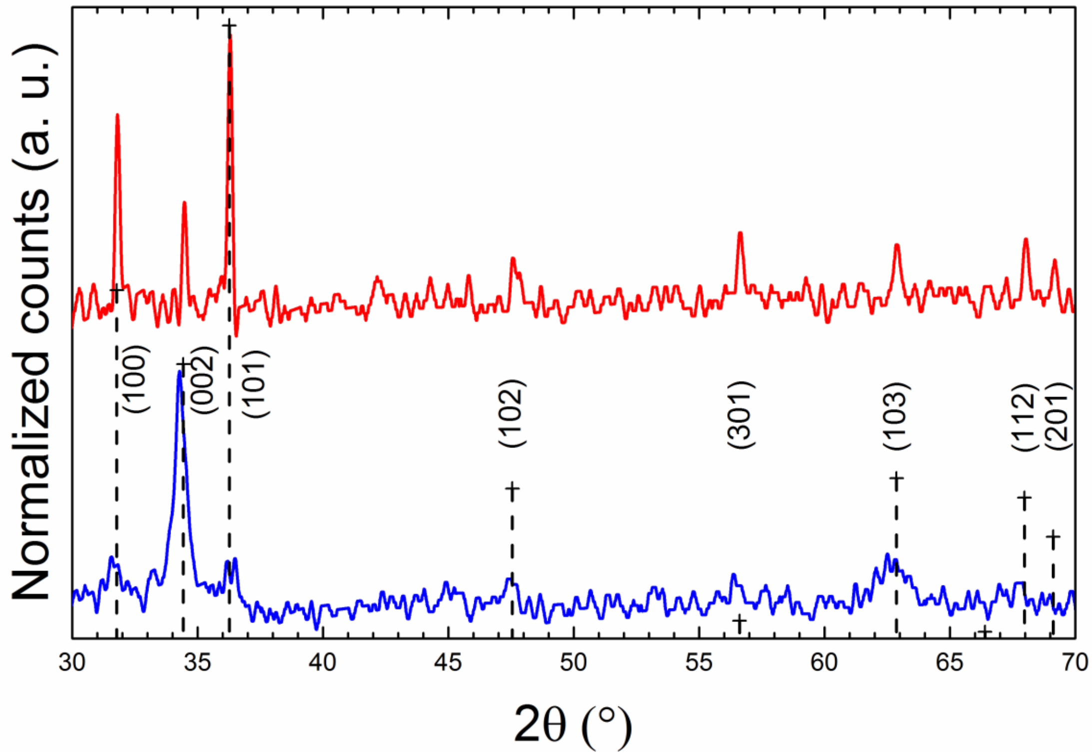

Figure 5.2 Diffractograms of the films grown from the hybrid (upper) and sintered (lower) targets, respectively. Dashed lines correspond to the standard pattern peaks.

The peaks of the ST films shift toward angles smaller than those of ZnO powder pattern as exemplified with the (002) peak angular position (2θ) in Table 5.1. This is proper of lattice expansion, due to inward relaxation, which has been associated with O vacancies in the ZnO lattice. On the other hand, all the peaks corresponding to HT films are slightly shifted to angular positions higher than those of the standard ZnO pattern as observed in the (002) peak angular position in Table 5.1. This peak shift indicates lattice shrinkage. Taking into account that N has a bigger atomic size than that of O, the introduction of N into the O sites of the ZnO lattice, besides passivating O vacancies, induces outward relaxation and consequently lattice shrinkage. Table 5.1 also shows the full width at half maximum of the (002) peak and some other lattice data obtained from diffractograms.

Table 5.1 Structural parameters obtained from diffractograms.

Parameter	Standard Pattern	HT film	ST film
$2\theta_{(002)}$ (°)	34.43	34.48	34.31
$FWHM_{(002)}$ (°)	-	0.174	0.544
a (nm)	0.3248	0.3248	0.3262
$\Delta a/a_0$ (%)	-	0	0.7
c (nm)	0.5205	0.5202	0.5227
$\Delta c/c_0$ (%)	-	0.06	0.04
c/a	1.602	1.602	1.602
D (nm)	-	48	12
η (%)	-	0.67	-0.96
V ($\times 10^{-3}$ nm^3)	47.554	47.532	48.175
$\Delta V/V_0$ (%)	-	-0.02	1.0
$d_{Zn\text{-}O}$ (nm)	4.252	4.250	4.270

Using the Williamson–Hall method [33], the crystallite size (D) and strain (ε) were found to be $D \approx 48$ nm (±1 nm) and $\varepsilon \approx 0.6$ % for HT films, while for ST films $D \approx 12$ nm (±1 nm) and $\varepsilon \approx -1.0$ %. Using the standard lattice geometry equations [34,35], from the angle position of (100) and (002) peaks we obtained the data presented in Table 5.1, where a and c are the lattice parameters, $\Delta a/a_0$ and $\Delta c/c_0$ are the lattice distortion on the a- and c-axis with respect to the lattice parameter of the pattern a_0 and c_0, D is the crystallite grain size, $\Delta V/V_0$ is the unit cell volume distortion, and $d_{Zn\text{–}O}$ is the Zn–O distance in the lattice. The strain over the c-axis was found to be one order lower than other one reported, even for ZnO grown by several techniques and annealed with the aim of reducing the strain [36-39]. The strain over a-axis was found almost null, and the unit cell volume in the HT film was not significantly different from that of the pattern. Observation of sample diffractograms shows that the ST film has preferential growth over the (002) plane. However, in the HT films the (101) peak is the most intense, although the (100) is also intense. This feature is similar to the ZnO pattern. For a better comparison of the sample diffractograms with the ZnO pattern, we used a simplified expression that relates the intensity of a specific peak to all the peaks observed in the diffractograms [38]. The expression, given by:

$$Ip_{hkl} = \frac{I_{hkl}}{\sum_n I_{hkl}} \tag{5.1}$$

will be used with the same peaks and allows us to compare the experimental diffractogram with the pattern. In our case, we considered n = 6 peaks. It is evident that all the HT film peaks have relative intensities very close to those of pattern as shown in Table 5.2. Conversely, the ST film peaks are quite different.

Table 5.2 Comparison of the relative peak intensity of pattern, Hybrid Target (HT) thin film and Sintered Target (ST) thin film.

N	Peak	Pattern		HT film		ST film	
		Intensity	Ip	Intensity	Ip	Intensity	Ip
1	(100)	0.570	0.207	0.747	0.258	0.236	0.117
2	(002)	0.414	0.150	0.426	0.147	1.000	0.496
3	(101)	0.999	0.362	1.000	0.346	0.220	0.109
4	(102)	0.210	0.076	0.172	0.059	0.149	0.074
5	(110)	0.301	0.109	0.230	0.080	0.165	0.082
6	(103)	0.264	0.096	0.318	0.110	0.248	0.123

5.3.2 Profilometry results

The measured film thicknesses were ~101 nm for the film grown from an ECA + ZnO hybrid target (HT film) and ~111 nm for the film grown from sintered ZnO target (ST film), respectively. At glance, HT films look light beige, which could indicate some absorption mainly in the blue–violet region.

5.3.3 Morphological analysis

The film roughness has been focus of attention of researchers because of its influence on devices performance, and in special in solar cells both inorganic and organic [40]. The morphological characteristics greatly affect the electrical properties of several devices as solar cells. The increase in the roughness ameliorates properties of the organic devices, since it increases the specific contact surface and improves light harvest, which redounds into higher photogenerated current density and device's efficiency [41–44]. However, in inorganic or conventional solar cells it is desirable low roughness in the transparent conductor oxide [45]. In the case of CdS/CdTe solar cells, previous reports [46–49] have demonstrated that the conversion efficiency strongly depends on the small roughness of the films surfaces; a reduction of surface roughness tends to increase the conversion efficiency of these solar cells. The roughness comparison of our films suggests that this component of a solar cell can be improved with ZnO made from a hybrid target.

However, SEM images show that the HT films are not flat, but present formation of micrometric surface clusters as observed in Figure 5.3(a), Figure 5.3(b) displays one of those surface accumulations in a transversal view. We associate such behavior to poor nucleation or adherence effect in the substrate surface presumably by residual presence of elemental or compound carbon arriving from the ECA decomposition.

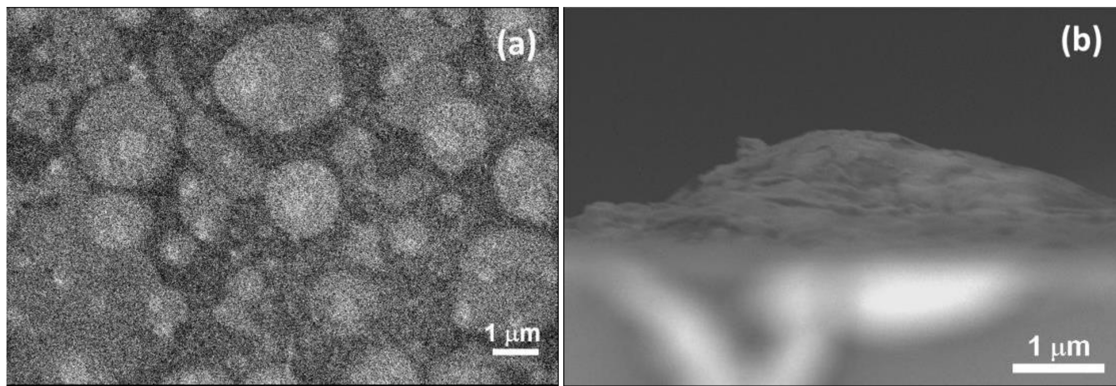

Figure 5.3 Surface (a) and cross-sectional (b) images of the HT film.

Figure 5.4 shows 3D AFM images of the ZnO HT and ST films. The surface roughnesses were 6.50 and 17.8 nm root-mean-squared (rms), respectively. Surface uniformity, film surface roughness, grain shape, and uniformity of grain size obtained in ZnO HT films indicate that they are better than ZnO ST thin films at nanoscale. 2D AFM images in Figure 5.5 show that the HT film has surface grains of about 50 nm, which agrees very well with the grain size calculated from X-ray diffraction, from where it is possible to affirm that the grain size coincides with the crystallite size. However, the observed grains in the 2D AFM image of the ST film have greater size, which contrasts with the smaller size estimated from X-ray diffraction and it is sign that the grains are formed by several crystallites. Besides, the grain size distribution looks uniform for the HT films, while they present a dispersed size distribution for the ST films.

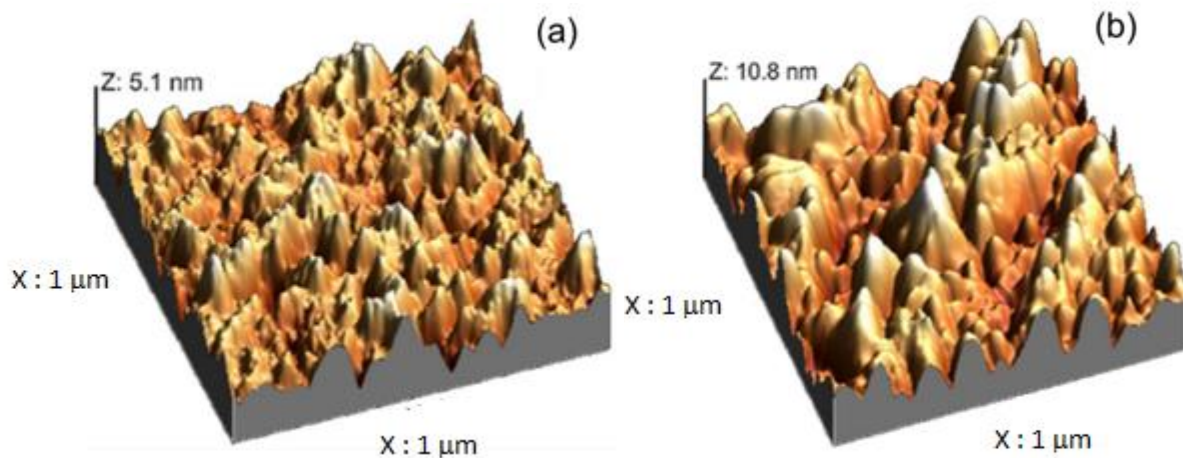

Figure 5.4 3D AFM images of the ZnO HT (a) and ST (b) films.

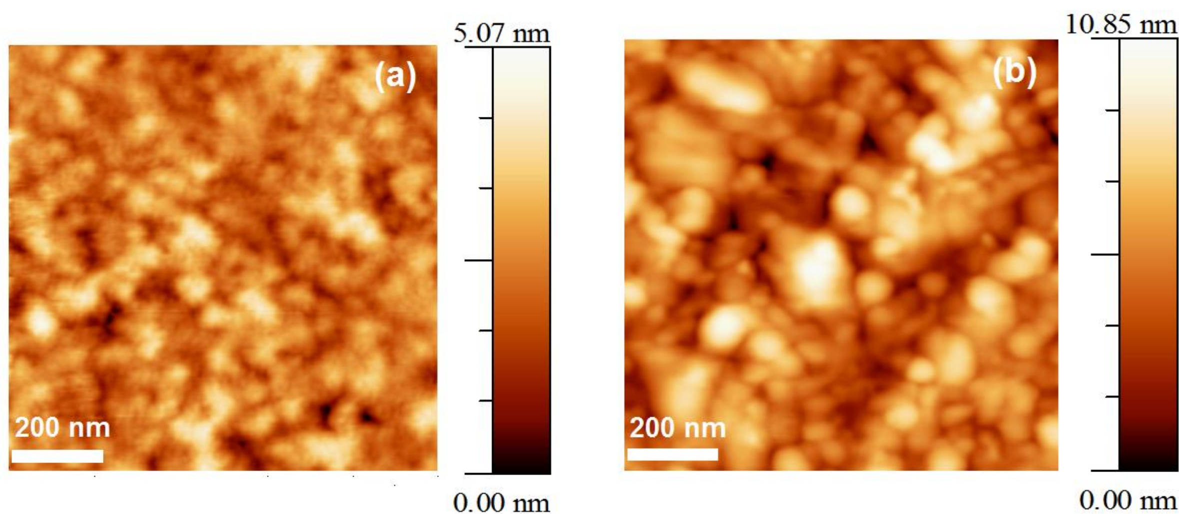

Figure 5.5 (a) 2D AFM image for the HT ZnO thin film (b) 2D AFM image for the ST ZnO thin film.

5.3.4 Chemical studies and bonding properties

The stoichiometry and chemical state of each constituent element from the obtained HT films is characterized using an X-ray photoelectron (XPS) analysis, the corresponding results are shown in Figure 5.6. The C1s (284.6 eV) peak was employed as reference to calibrate the binding energies of all the examined elements. A wide scan spectrum for the HT film is depicted in Figure 5.6(a). The pholoelectron and auger lines in the binding energy scale identified each constituent element for the resulting HT sample, so all peaks in the survey curve reveal the presence of C, O, Zn and N elements; no other peaks corresponding to additional elements were observed. The strong presence of the C1s peak in Figure 5.6(a) could be explained taking into account the use of carbon tape which is usually used in the XPS characterization of powder samples [50] and the carbon presence in the ECA glue. Figure 5.6(b) displays the XPS high resolution spectrum of oxygen. The spectrum of O1s indicated the presence of one single chemical state and it was fitted with a single peak using a Gaussian adjustment. The peak was located approximatly at 531.5 eV and it can be adscribed to the O-Zn binding [51]. The two peaks appearing in Figure 5.6(c) centered at the binding energies of 1021.9 and 1044.7 eV in the spectra of the Zn2p correspond to the Zn^{2+} $2p_{3/2}$ and Zn^{2+} $2p_{1/2}$ respectively. The lone and sharp peak at 1021.9 for the Zn^{2+} $2p_{3/2}$ core level is associated with the Zn species in the completely oxidized state [52]. Ultimately in Figure 5.6(d) the binding energy on the Zn Auger $L_3M_{4,5}M_{4,5}$ region of the surface spectrum is presented and agrees with previous reports [53]. Contributions of Zn–O (499.7 eV) and Zn–N (496.9 eV) bindings can be observed. No other contributions were perceived. Using the ratio between the XPS spectrum areas for Zn–O and Zn–N bonds, we found that Zn has 53 % of its bindings to O and 47 % to N.

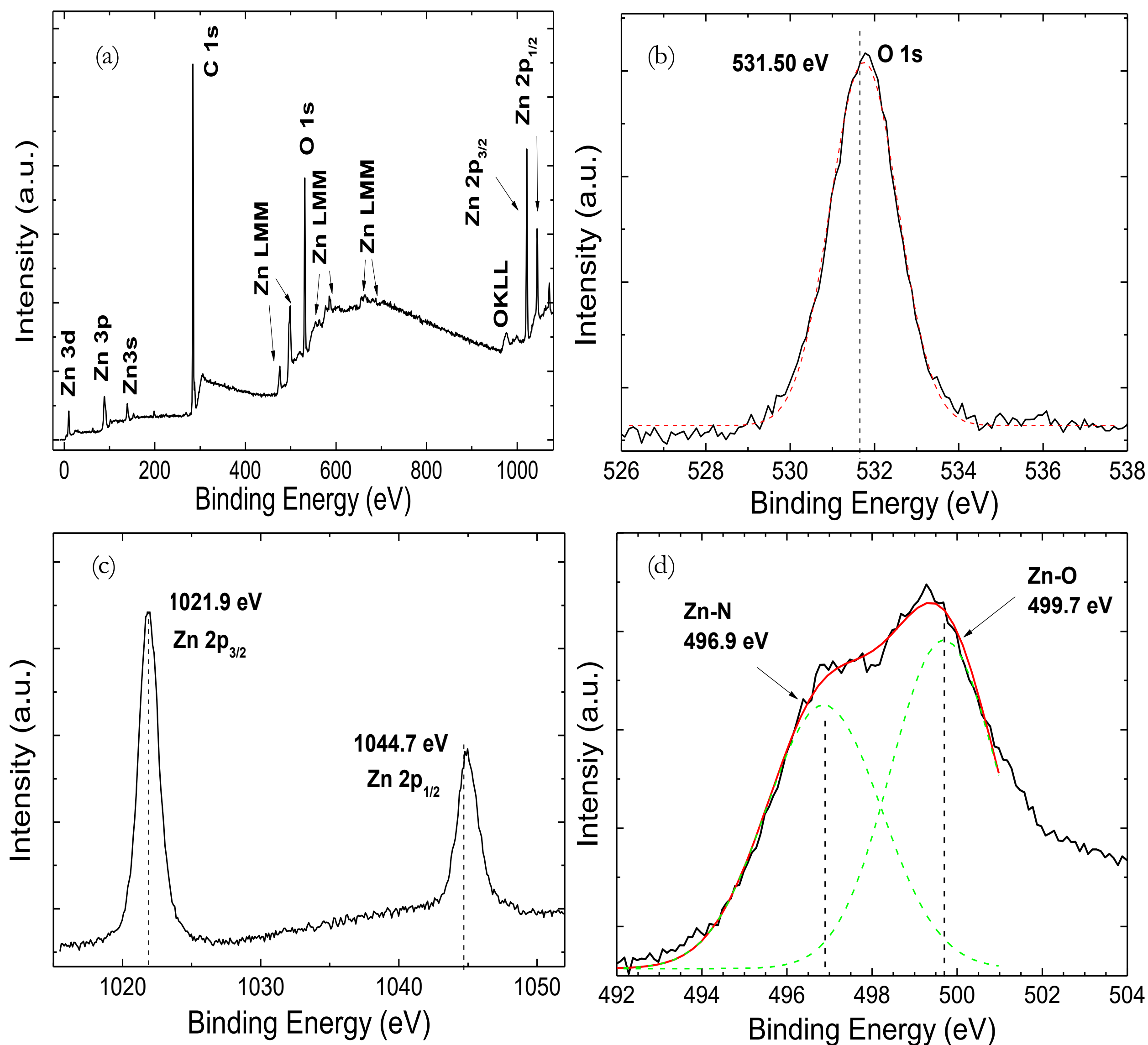

Figure 5.6 XPS spectra of HT films: (a) wide scan and high resolution spectra of the (b) O 1s; (c) Zn 2p; and (d) Zn Auger L3M4,5M4,5 regions.

5.3.5 Optical and electrical analysis

Absorption profile obtained from the transmission spectrum is presented in Figure 5.7. The profile displays two shoulders, which is indicative of the presence of two overlapped absorbing profiles corresponding to two compounds. A careful processing of the absorption profile leads to obtaining that the band gap energy of the highest energy shoulder is at Eg ≈ 3.20–3.23 eV, which was identified as corresponding to ZnO. The processing of the other shoulder gives an intercept at 2.35 eV, which was associated with the band gap energy of zinc oxynitride. Thus, taking into account the XPS results, we can infer that the films are formed of ZnO molecular units with formation of $Zn_xO_yN_z$ [54] molecular subunits. However, the slope of the zinc oxynitride absorption edge is relatively low, which can be related to different combinations of x, y, and z of the $Zn_xO_yN_z$ molecular subunits as has been proposed in other ternary compounds [55]. The absence of peaks other than those of ZnO wurtzite in the diffractograms can be explained from considering low degree of polymerization of the oxynitride. The film absorption begins at about 2.5 eV, i.e., the film absorbs in the blue–violet region, which agrees with the sample color.

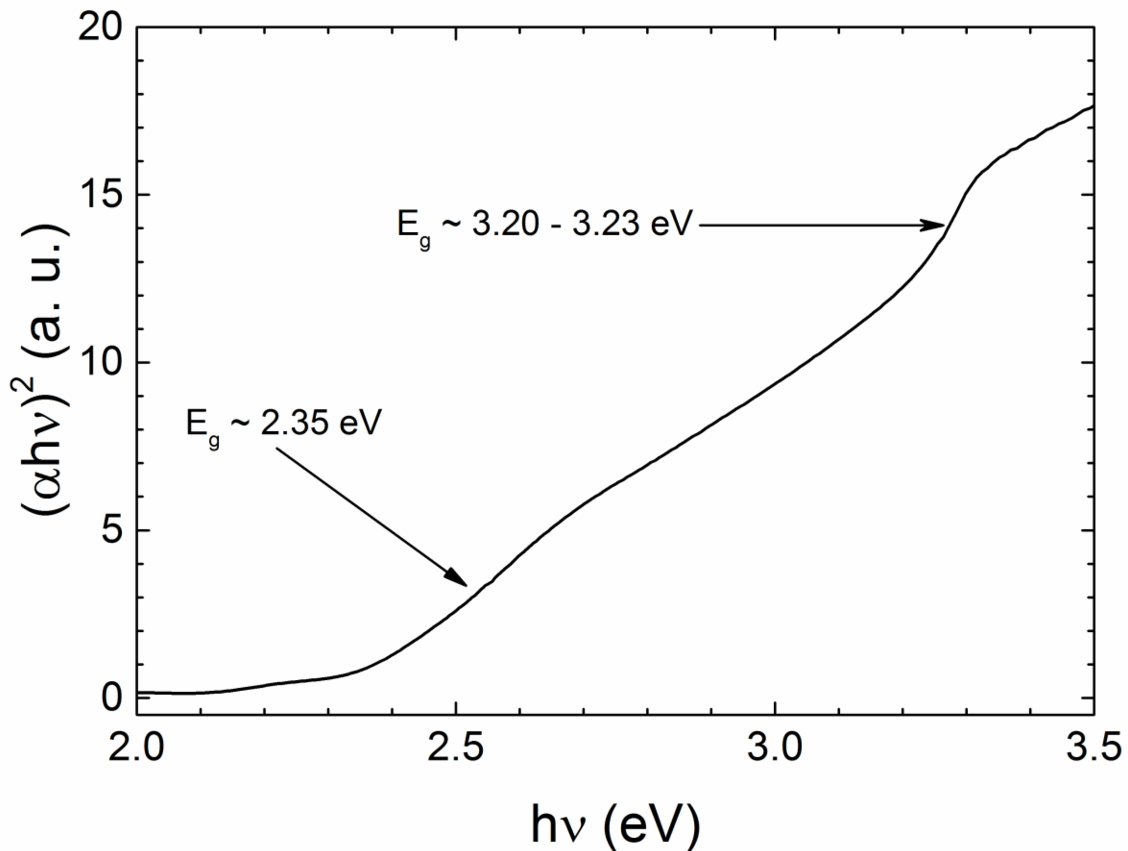

Figure 5.7 Tauc plot of $(\alpha h\nu)^2$ vs. hν calculated from the transmission spectra.

Considering a linear variation among Zn_3N_2 [56] and ZnO band gaps in a $(Zn_3N_2)_r$-$(ZnO)_s$ pseudobinary alloy, we can approximately estimate that E_g ≈ 2.35 eV corresponds to s = 0.58, which is close that determined from XPS measurement for Zn-O. Following the same procedure, from the data of Zn_3N_2 band gap energy, E_g ≅ 0.9 eV and electron affinity χ ≅-3.1 eV [56], and from the measured band gap energy it is possible to estimate that the conduction band minimum is at CBM ≈-0.87 eV and the valence band maximum is at VBM ≈-6.1 eV respect to the vacuum level, both linear approximations are

shown in Figure 5.8. Zinc nitride and oxynitrides have been proposed with potential as a precursor in the fabrication of *p*-type ZnO:N [53]. The heterojunction of Zn_3N_2 with ZnO forms a type-III heterostructures with broken band gaps according to the band alignment [56]. However, it can change to type-II heterostructure for $Zn_xO_yN_z$ with staggered band gaps, which could occur even for low N concentration in ZnO. This fact, although local, favours the extraction of photogenerated electrons from $Zn_xO_yN_z$ towards ZnO.

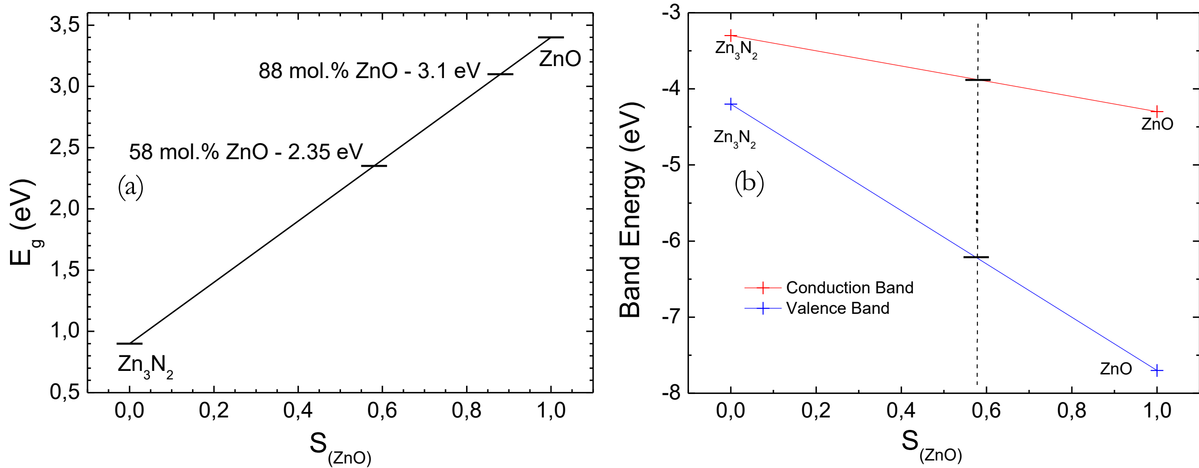

Figure 5.8 Linear approximation of the Zn_3N_2 and ZnO (a) band gaps and (b) CBM and VBM in a $(Zn_3N_2)r$-$(ZnO)s$ pseudobinary alloy.

The resistivity for both HT and ST films were higher than 10^5 Ω cm, which is the effective experimental detection limit of the Hall system. Thus, both samples can be considered as very good buffer layer. The basis of these attained almost-ideal low-stressed ZnO films can be explained from considering a growth by deposition of ZnO clusters. The high-energy impact of the clusters with kinetical energies higher than that of atoms or species as was discussed from the multiscale computational approach for laser ablation cluster generation and deposition. Thus this energy can transform into thermal energy and leads to recrystallization of the clusters in the film growth surface as in an epitaxial growth [57]. We consider that such cluster ejection takes place due to the low cohesion of the polymeric matrix that practically explodes abruptly under the action of the incident laser high-energy, which triggers the ZnO cluster ejection toward the substrate. Moreover, in our case, highly reactive N species could form from the poly(ECA) decomposition. This experiment lays the groundwork for the use of polymers, like ECA, as binder matrix of inorganic compounds in the preparation of targets for film growth by the PLD technique. In practice, although polymer cannot re-assemble from isolated atomic species as the inorganic materials, its decomposition products can be used for doping and for forming other compounds. Thus, special attention must be put on the organic decomposition products, which could have controversially effects according the prospective use of the grown film. Although a part of the ECA decomposition products can vaporize and be evacuated by the vacuum system, another part of the polymer decomposition can acts as dopant. In our samples we found that N reacts with ZnO to form a $Zn_xO_yN_z$ compound, which will be object of future further studies.

5.4 Partial conclusions

In this chapter we studied ZnO films grown by the Nd:YAG-pulsed laser deposition method from a hybrid target formed with ZnO powder nanoparticles embedded into poly(ethyl cyanoacrylate). With the aim of comparing ZnO films were grown from a typical sintered target. XRD diffractograms showed that the films grew in the hexagonal wurtzite structure and the HT films presented a practically unstressed structure similar to that of powder pattern. The grain sizes were estimated to be ~48 nm and ~12 nm for HT and ST films respectively. AFM images showed that the film surfaces of the ST film are almost three times rougher than HT film. XPS measurement showed the existence of Zn-N and Zn-O bonds. Optical absorption profile confirmed the presence of zinc oxynitride besides ZnO. Thus, the relevant results of this work were that with the use of a hybrid target formed by the mixture of a polymer and an inorganic material as ZnO in the pulsed laser deposition technique, low-stressed ZnO thin films were grown and the possibility of using the decomposition product of the polymer either as dopant or in the formation of a new compound. In this case the compound was zinc oxynitride, which can form type-II heterostructures and be prospectively useful in photovoltaics and sensors.

5.5 References

[1] Y. Segawa, H. D. Sun, T. Makino, M. Kawasaki, and H. Koinuma, Exciton Related Stimulated Emission in ZnO-Based Multiple-Quantum Wells, Physica Status Solidi A 192 (2002) 14-20.

[2] F. Tan, Sh. Qu, P. Yu, F. Li, Ch. Chen, W. Zhang, Zh. Wang, Hybrid bulk-heterojunction solar cells based on all inorganic nanoparticles, Solar Energy Materials & Solar Cells 120 (2014) 231–237.

[3] D. Duché, F. Bencheikh, S. Ben Dkhil, M. Gaceur, N. Berton, O. Margeat, J. Ackermann, J.J. Simon, L. Escoubas, Optical performance and color investigations of hybrid solar cells based on P3HT:ZnO, PCPDTBT:ZnO, PTB7:ZnO and DTS(PTTh$_2$)$_2$:ZnO, Solar Energy Materials & Solar Cells 126 (2014) 197–204.

[4] Y. Zhao, X. Peng, Zh. Li, M. Zhou, X. Liang, J. Wang, J. Min, L. Wang, W. Shi, The photoluminescence characterization of the N-doped ZnO films produced by wet chemical deposition , Applied Physics A 107 (2012) 959–963.

[5] A. Jain, P. Sagar, R.M. Mehra, Solid-State Electronics, Band gap widening and narrowing in moderately and heavily doped n-ZnO films, Solid-State Electronics 50 (2006) 1420–1424.

[6] Y.Z. Zhang, J.G. Lu, Z.Z. Ye, H.P. He, L.P. Zhu, B.H. Zhao, L. Wang, Effects of growth temperature on Li–N dual-doped p-type ZnO thin films prepared by pulsed laser deposition, Applied Surface Science 254 (2008) 1993–1996.

[7] Y. Nakano, T. Morikawa, T. Ohwaki, Y. Taga, Electrical characterization of pp-type N-doped ZnO films prepared by thermal oxidation of sputtered $Zn_3N_2Zn_3N_2$ films, Applied Physics Letters 88 (2006) 172103.

[8] F. X. Xiu, Z. Yang, L. J. Mandalapu, D. T. Zhao, and J. L. Liua, High-mobility Sb-doped pp-type ZnO by molecular-beam epitaxy, Applied Physics Letters 87 (2005 152101

[9] D.C. Look, D.C. Reynolds, C.W. Litton, R.L. Jones, D.B. Eason, G. Cantwell , Characterization of homoepitaxial *p*-type ZnO grown by molecular beam epitaxy, Applied Physics Letters 81 (2002) 1830.

[10] Z.Z. Ye, J.G. Lu, H.H. Chen, Y.Z. Zhang, L. Wang, B.H. Zhao, J.Y. Huan, Preparation and characteristics of p-type ZnO films by DC reactive magnetron sputtering , Journal of Crystal Growth 253 (2003) 258–264.

[11] K.K. Kim, H.S. Kim, D.K. Hwang, J.H. Lim, S.J. Park, Realization of p-type ZnO thin films via phosphorus doping and thermal activation of the dopant, Applied Physics Letters, 83 (2003) 63.

[12] F.G. Chen, Z.Z. Ye, W.Z. Xu, B.H. Zhao, L.P. Zhu, J.G. Lu, Fabrication of p-type ZnO thin films via MOCVD method by using phosphorus as dopant source, Journal of Crystal Growth 281 (2005) 458–462.

[13] Y.R. Ryu, S. Zhu, D.C. Look, J.M. Wrobel, H.M. Jeong, H.W. White, Synthesis of p-type ZnO films, Journal of Crystal Growth 216 (2000) 330-334.

[14] J.G. Lu, Y.Z. Zhang, Z.Z. Ye, Y.J. Zeng, H.P. He, L.P. Zhu, J.Y. Huang, L. Wang, J. Yuan, B.H. Zhao, X.H. Li, Control of p- and n-type conductivities in Li-doped ZnO thin films, Applied Physics Letters 89 (2006) 112113.

[15] J.G. Lu, Y.Z. Zhang, Z.Z. Ye, L.P. Zhu, L. Wang, B.H. Zhao, Q.L. Liang, Low-resistivity, stable p-type ZnO thin films realized using a Li–N dual-acceptor doping method, Applied Physics Letters 88 (2006) 222114.

[16] X.H. Wang, B. Yao, Z.P. Wei, D.Z. Shen, Z.Z. Zhang, B.H. Li, Y.M. Lu, D.X. Zhao, J.Y. Zhang, X.W. Fan, L.X. Guan, C.X. Cong, Acceptor formation mechanisms determination from electrical and optical properties of p-type ZnO doped with lithium and nitrogen, Journal of Physics D: Applied Physics39 (2006) 4568.

[17] A. Krtschil, A. Dadgar, N. Oleynik, J. Bläsing, A. Diez, A. Krost, Local pp-type conductivity in zinc oxide dual-doped with nitrogen and arsenic, Applied Physics Letters 87 (2005) 262105.

[18] C. H. Park, S. B. Zhang, Su-Huai Wei, Origin of *p*-type doping difficulty in ZnO: The impurity perspective, Physical Review B 66 (2002) 073202.

[19] Don Klaitabtim , Sirapat Pratontep, Jiti Nukeaw, Growth and Characterization of Zinc Oxynitride Thin Films by Reactive Gas-Timing RF Magnetron Sputtering, Japanese Journal of Applied Physics 47 (2008) 653–656.

[20] G. Braunstein, A. Muraviev, H. Saxena, N. Dhere, V. Richter, R. Kalish, p type doping of zinc oxide by arsenic ion implantation, Applied Physics Letters 87 (2005) 192103 .

[21] Kazunori Minegishi, Yasushi Koiwai, Yukinobu Kikuchi, Koji Yano, Masanobu Kasuga and Azu ma Shimizu, Growth of p-type Zinc Oxide Films by Chemical Vapor Deposition, Japanese Journal of Applied Physics 36 (1997) 1453-1455.

[22] Tamiko Ohshima , Tomoaki Ikegami , Kenji Ebihara , Jes Asmussen , RajK.Thareja, Synthesis of p-type ZnO thin films using co-doping techniques based on KrF excimer laser deposition, Thin Solid Films 435 (2003) 49–55.

[23] Tsoutsouva M.G., Panagopoulos C.N., Papadimitriou D., Fasaki I., Kompitsas M., ZnO thin films prepared by pulsed laser deposition, Materials Science and Engineering B 176 (2011) 480-483

[24] V. Serbezov, Pulsed Laser Deposition: The Road to Hybrid Nanocomposites Coatings and Novel Pulsed Laser Adaptive Technique, Recent Patents on Nanotechnology 7 (2013) 26-40.

[25] P. Caricato, V. Arima, M. Catalano, M. Cesaria, P.D. Cozzoli, M. Martino, A. Taurino, R. Rella, R. Scarfiello, T. Tunno, A. Zacheo, MAPLE deposition of nanomaterials, Applied Surface Science 302 (2014) 92–98.

[26] R. D. Torres, S. L. Johnson , R. F. Haglund Jr. , J. Hwang , P. L. Burn, and P. H. Holloway, Mechanisms of Resonant Infrared Matrix-Assisted Pulsed Laser Evaporation, Critical Reviews in Solid State and Materials Sciences 36 (2011) 16–45.

[27] K. Grochowska, S. Majumdar, P. Laukkanen, H. S. Majumdard M. Sawczak and G. Śliwiński, Pulsed laser deposition of organic semiconductor rubrene thin films, Proceedings SPIE 9447 (2015) 94470F-1.

[28] H. V. Coover, D. W. Dreifus, J. T. O. Conner, Cyanoacrylate adhesives, in: I. Skeist (Ed.), Handbook of Adhesives, 3rd ed., Van Nostrand Reinhold, New York, 1990.

[29] R. J. Lewis, Sr. (ed) Sax's Dangerous Properties of Industrial Materials. 11th Edition. Wiley-Interscience, Wiley & Sons, Inc. Hoboken, NJ. 2004, p. 1645.

[30] American Conference of Governmental Industrial Hygienists. Documentation of the TLV's and BEI's with Other World Wide Occupational Exposure Values. CD-ROM Cincinnati, OH 45240-4148, 2010.

[31] Y. Liu and Sh. Sh. Fan, Enhancement of field emission properties of cyanoacrylate–carbon nanotube arrays by laser treatment, Nanotechnology 15 (2004) 1033–1037.

[32] 2003 JCPDS-International Centre for Diffraction Data. PCPDFWIN v. 2.4. Chart No. 89- 0510.

[33] G. K. Williamson, W. H. Hall, X-ray line broadening from filed aluminium and wolfram, Acta Metallurgica 1 (1953) 22–31.

[34] A. Iribarren, E. Hernández-Rodríguez, L. Maqueira, Structural, Chemical and optical evaluation of Cu-doped ZnO nanoparticles synthesized by an aqueous solution method, Materials Research Bulletin 60 (2014) 376–381.

[35] Jasmeet Kaur, Praveen Kumar, Thangaiah Stephen Sathiaraj and Rengasamy Thangaraj, Structural, optical and fluorescence properties of wet chemically synthesized ZnO: Pd^{2+} nanocrystals, International nanoletters (2013) 3:4.

[36] P. Ghosh, A. K. Sharma, Pulsed laser deposition and characterization of ZnO nanopores, Applied Physics A 122 (2016) 122:357.

[37] P. K. Jain, M. Salim, D. Kaur, Structural and optical properties of pulsed laser deposited ZnO/TiO_2 and TiO_2/ZnO thin films, Optik 126 (2015) 3260-3262.

[38] M. F. Malek, M. H. Mamat, M. Z. Musa, Z. Khusaimi, M. Z. Sahdan, A. B. Suriani, A. Ishak, I. Saurdi, S. A. Rahman, M. Rusop, Thermal annealing-induced formation of ZnO nanoparticles:

Minimum strain and stress ameliorate preferred *c*-axis orientation and crystal-growth properties, Journal of Alloys and Compounds 610 (2014) 575–578.

[39] T. Liu, X. Fei, L. Hu, H. Zhang, Y. Li, Sh. Duo, Effect of substrate surface pretreatment and annealing treatment on morphology, structure, optical and electrical properties of sputtered ZnO films, Superlattices Microstructures 83 (2015) 604–617.

[40] M. Richter, P. Saint-Cast, T. Dannenberg, M. Zimmer, J. Rentsch, Impact of Rear Side Roughness on Optical and Electrical Properties of a High-efficiency Solar Cell, Energy Procedia 77 (2015) 832-839.

[41] M. Berginski, J. Hüpkes, M. Schulte, G. Schöpe, H. Stiebig, and B. Rech, J. Appl. Phys. 101, 074903 (2007).

[42] M. Zeman, R. A. C. M. M. van Swaaij, and J. W. Metselaar, R. E. I. Schropp, The effect of front ZnO:Al surface texture and optical transparency on efficient light trapping in silicon thin-film solar cells, Journal of Applied Physics 88 (2000) 6436.

[43] G. Li, V. Shrotriya, Y. Yao, and Y. Yang, Investigation of annealing effects and film thickness dependence of polymer solar cells based on poly(3-hexylthiophene), Journal of Applied Physics 98 (2005) 043704.

[44] M. Fathy, Sh. Elyamny, S. Mahmoud and A. El-H. B. Kashyout, Effect of Thermal and Chemical Treatment on Electrodeposited CdTe Thin Films for Solar Cell Applications, International Journal of Electrochemical Science 10 (2015) 6030-6043.

[45] F. Dimroth, M. Grave, P. Beutel, U. Fiedeler, Ch. Karcher, T. N. D. Tibbits, E. Oliva, G. Siefer, M. Schachtner, A. Wekkeli, A. W. Bett, R. Krause, M. Piccin, N. Blanc, Ch. Drazek, E. Guiot, B. Ghyselen, Th. Salvetat, A. Tauzin, T. Signamarcheix, A. Dobrich, T. Hannappel and K. Schwarzburg, Wafer bonded four-junction GaInP/GaAs//GaInAsP/GaInAs concentrator solar cells with 44.7% efficiency, Progress in Photovolt: Resesearch and Applications 22 (2014) 277-282.

[46] M. Tsuji, T. Aramoto, H. Ohyama, T. Hibino, K. Omura, Characterization of CdS Thin-Film in High Efficient CdS/CdTe Solar Cells, Japanese Journal of Applied Physics 39 (2000) 3902–3906.

[47] L. Grenet, S. Bernardi, D. Kohen, Ch. Lepoittevin, S. Noël, N. Karst, A. Brioude, S. Perraud, H. Mariette, $Cu_2ZnSn(S_{1-x}Se_x)_4$ based solar cell produced by selenization of vacuum deposited precursors, Solar Energy Materials and Solar Cells 101 (2012) 11–14.

[48] E. Colegrove, R. Banai, C. Blissett, C. Buurma, J. Ellsworth, M. Morley, S. Barnes, C. Gilmore, J. D. Bergeson, R. Dhere, M. Scott, T. Gessert, and S. Sivananthan, High-Efficiency Polycrystalline CdS/CdTe Solar Cells on Buffered Commercial TCO-Coated Glass, Journal of Electronic Materials 41 (2012) 2833-2837.

[49] M. Dharmadasa, Review of the $CdCl_2$ Treatment Used in CdS/CdTe Thin Film Solar Cell Development and New Evidence towards Improved Understanding ,Coatings 4 (2014) 282-307.

[50] Yingying Lv, Leshu Yu, Heyong Huang, Yuying Feng, Dongzhen Chen, Xin Xie, Application of the soluble salt-assisted route to scalable synthesis of ZnO nanopowder with repeated photocatalytic activity, Nanotechnology 23 (2012) 065402.

[51] Cheng Chao Li, Xiao Ming Yin, Qiu Hong Li, Tai Hong Wang, Enhanced gas sensing properties of ZnO/SnO_2hierarchical architectures by glucose-induced attachment, CrystEngComm 13 (2011) 1557-1563.

[52] Xuebin Wang, Kaifu Huo, Fan Zhang, Zheng Hu, Paul K. Chu, Haisheng Tao, Qiang Wu, Yemin Hu, Jianmin Zhu, Structural Regulation and Optical Properties of One-Dimensional ZnO Nanomaterials in Situ Grown from and on Brass Substrates, The Journal of Physicalchemistry C 113 (2009) 170–173.

[53] N. Jiang, D. G. Georgiev, A. H. Jayatissa, R. W. Collins, J. Chen, E. McCullen, J. Phys. D: Appl. Phys. 45, 135101 (2012).

[54] D. Li, H. Haneda, Synthesis of nitrogen-containing ZnO powders by spray pyrolysis and their visible-light photocatalysis in gas-phase acetaldehyde decomposition, Journal of Photochemistry and Photobiology A: Chemistry 155 (2003) 171–178.

[55] A. Iribarren, E. Menéndez-Proupin, F. Caballero-Briones, R. Castro-Rodríguez, J. L. Peña, Composition mixture probabilistic model in the formation of semiconductor materials obtained by random growth technique, Moder Physics Letters B 15 (2001) 643-646.

[56] S.-H. Yoo, A. Walsh, D. O. Scanlon, A. Soon, Electronic structure and band alignment of zinc nitride, Zn_3N_2, RSC Adv. 4 (2014) 3306-3311.

[57] L. V. Zhigilei and A. M. Dongare, Multiscale Modeling of Laser Ablation: Applications to Nanotechnology, CMES-Computer Modeling in Engineering 3 (2002) 539-555.

Chapter 6 Effect of substrate rotation speed on the structure and properties of Al-doped ZnO thin films prepared by RF-Sputtering

In present chapter the effect of the substrate rotation speed (ω_S) on the morphological, structural, optical and electrical of properties of Al-doped ZnO (AZO) thin films deposited by RF-sputtering is reported. SEM transversal images showed that the substrate rotation produces dense columnar structures which were absent for the samples under no rotation. AFM images show that the surface particles of the samples formed under substrate rotation are smaller in size and denser than those of a stationary one, leading to smaller grain sizes. XRD results showed that all films have hexagonal wurtzite structure and a preferred c-axis orientation with a tensile stress along aforementioned axis. The average optical transmittance for all samples was above 90% in UV-vis region. The substrate rotation induced changes in the carrier concentration and hall mobility which resulted in the increasing of electrical resistivity, being the resistivity value for the sample deposited at ω_S = 0 rpm (8.5 x 10^{-3} Ω cm) the lowest of the obtained films.

6.1 Transparent conductive oxides

A transparent material (TC), which includes transparent conductive oxides (TCO's) is a semiconductor material with two main properties, namely a high transparency in the visible region and a high electrical conductivity; these characteristics are mainly caused by their wide band gap and their relatively high concentration of free electrons in their conduction band, these properties are caused by intrinsic defects of the material or due to extrinsic materials which act as dopants. A TCO material requires a balance between its optical transmittance and its electrical conductivity, the adequate properties will depend of the specific application in which the TCO material would be implemented.

6.1.1 Optical properties

When light impinges in the surface of any material there are several interactions that could take place between its photons and the surface of the material. An impinging photon can be absorbed, reflected or transmitted. A TCO absorbs some portion of the incident light upon it, corresponding to its bandgap. The energy/wavelength of the incident photons determine many of the phenomena that occurs when light travels through the material, e.g., refraction which consists in the modification of the path or speed at which the light moves inside the material, or the scattering due to interaction of light with internal surfaces of the material. Transmittance, as its name implies, measures the effectiveness in transmitting radiant energy through the sample, in other words, it is the fraction of incident electromagnetic power that is transmitted through a sample. Energy conservation yields, at each wavelength, that:

$$T + R + A = 1 \tag{6.1}$$

Where T, R, and A denote transmittance, reflectance, and absorbance, respectively. Figure 6.1 illustrates all the possible interactions (absorption and reflection) that light could have with the surface of a TCO material.

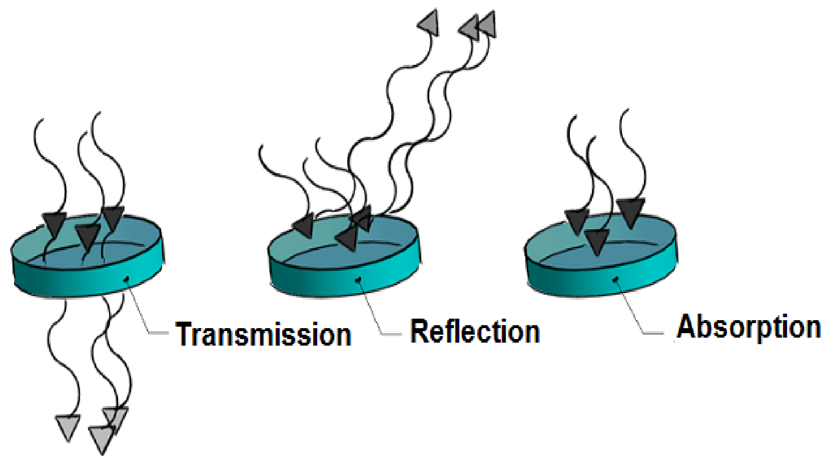

Figure 6.1 Interactions of light photons within a TCO material.

The optical and electrical properties of any material are deeply related to each other, as the electric field component of light is capable of interacting with the electrons in the material, as it is described in the Drude free electron model [1]. Any material with a band gap higher than 3.1 eV would be considered transparent and will be called wide band gap semiconductor. The electrical properties of these materials are enhanced by adding a doping material; this produces a transparent conductor. Figure 6.2 shows a typical optical spectrum for a TCO material, namely, an Al doped ZnO thin film deposited on a glass substrate and is divided into three parts, transmission, reflection, and absorption spectra [2].

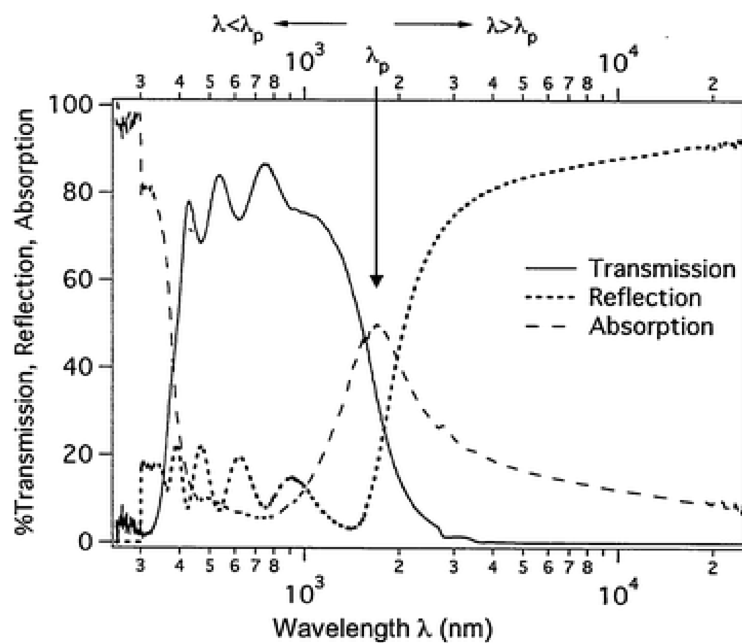

Figure 6.2 Transmission, reflection, and absorption spectra of a typical TCO.

As it was mentioned before, a conductive oxide must be transparent in the visible region, in this case the presented film has a transparency superior to ~80% for the wavelength region of 400-750 nm,

the presence of oscillations for both transmittance and reflectance spectra are also observed. There are two regions where the transmittance spectra is abruptly decreased, the first region comes along with an increase in the absorption spectra, this occurs at shorter wavelengths (<350 nm or 3.5 eV), this is due to the fundamental absorption (optical band gap) of the material where electrons are excited from the valence band to the conduction band, and as it was mentioned above, a typical TCO has a band gap greater than 3 eV. The second region where the transmittance decreases comes along with an increasing in the reflectance spectra, and it is observed at longer wavelengths (>1500 nm) on the other end of the spectra and is due to collective oscillation of electrons in the conduction band called plasma oscillations (plasmons). In this transition region there is a maximum in the absorption spectra which is called plasma wavelength (λ_p), where the frequency of the light is the same as the frequency of the collective oscillation of electrons in the material, this wavelength is dependent on the number of electrons in the conduction band (carrier concentration) and will shift towards lower wavelengths when the carrier concentration is increased. When $\lambda<\lambda_p$ the wavefunction is oscillatory and radiation can propagate, resulting in a transparent material. When $\lambda > \lambda_p$ the wavefunction decays and no radiation can propagate, resulting in reflection, finally when the electrons oscillate in phase with the electric field component of the light will result in absorption [2].

6.1.2 Electrical properties

So far, most of the TCO materials discovered possess *n*-type conductivity, although some have *p*-type conductivity. This native *n*-type behavior arises from the presence of stoichiometric deviations, and many attempts to modify it have been made with limited success. The process of doping (which was described in Chapter 4) is employed to enhance or attune the electrical properties of a TCO material. Going from *p* to *n*-type also has proven to be a difficult task for some materials, due to the formation of defects that compensate the doping. Based on the aforesaid reasons it is seen that there are several factors that need to be taken into account when finding the adequate balance between the electrical conductivity and optical transmittance in a TCO for the desired application. Electrical conductivity (σ) is defined in units of S cm^{-1} as:

$$\sigma = Ne\mu \tag{6.2}$$

Where N is the carrier concentration (cm^{-3}), e is the carrier charge (C) and μ carrier mobility ($cm^2V^{-1}S^{-1}$). In semiconductors, both electrons and holes are carriers and both will contribute to the conductivity. Therefore there are two possible ways to increase the conductivity of a material, namely, by increasing either its carrier concentration (N) or its carrier mobility (μ).

6.1.3 Applications of TCO'S

Transparent conducting oxides (TCOs) possess a wide range of applications in a variety of optoelectronic devices like flat panel displays [3], thin film solar cells [4, 5] or touch screens [6]. Depending on the application there are different requirements that a TCO material must met. For example, transparent electrodes should have a carrier concentration in the order of ~10^{20}-10^{21} cm^{-3}, with a

resistivity value inferior to 10^{-3} Ω cm. Furthermore; the optical transmittance value should be above 80% in the visible range with a band gap value superior to 3 eV [7].

Tin indium oxide (ITO) is regarded as one of the best TCOs because it presents both high electrical conductivity and optical transparency. Many ITO thin films prepared by various techniques report optical transmittances in the visible region of 75-90% with a bang gap between 3.55 and 3.75 eV, with resistivity values below 10^{-4} Ω cm [8]. However it is very scarce and expensive, so there are continuous efforts to find a suitable substitute material. One of the promissory materials is zinc oxide (ZnO) with *n*-type conductivity, wide band gap (Eg ~ 3.4 eV) and large exciton binding energy (60 meV) [9]. Extrinsic dopants are employed to modify and improve the electrical and optical properties of ZnO, aluminum being one of the most commonly used, as it will be discussed below.

6.2 Al-doped zinc oxide as a TCO

Among the many transparent conductive oxides (TCO's), Al-doped ZnO (AZO) is well known for having good electrical conductivity and high transparency which make it a promising candidate to replace other conventional TCO'S [10]; its conduction mechanism which is based in oxygen vacancies and interstitial zinc atoms, as wells as its exciton emissions even at room temperature make it as a promising material for many applications which include photoelectrical devices [11], gas sensors [12], and light-emitting diodes [13].

6.3 RF- Magnetron sputtering technique for the growth of Al-doped zinc oxide thin films

There are many reports about the deposition of AZO thin films using vacuum and solution based techniques such as magnetron sputtering [14], pulsed laser deposition [15], chemical vapor deposition [16], spray pyrolysis [17], sol-gel process [18] to name a few. Among these deposition techniques, magnetron sputtering has characteristics of low deposition temperature, good film adhesion, high reproducibility and easy preparation in large areas [11]. In RF- sputtering the most important deposition parameters that affect the properties of the obtained thin films are substrate-to-target distance, substrate temperature, oxygen flow rate, the RF-power and the working pressure [19].

6.3.1 Substrate rotation in the sputtering process

The substrate rotation velocity is also an important parameter which has been used to control and alter the surface roughness, morphology and structural properties of many deposited materials [20-22]. Previous works reported that rotation of the substrate holder around its normal is employed to achieve a homogeneous deposition and thus it is clear that with the substrate rotation, the distance target substrate is varied from its shortest to the longest value within one rotation cycle [23], and it is known that the substrate-target distance affects the energy of the adatoms arriving to the surface of the substrate [24]. For this reason it is expected that many properties of the deposited coatings are affected by substrate rotation, for instance Wada et al. [25], reported a study on ZrO_2 deposited by electron beam vapor deposition where they found that structural formation of the deposited layers was strongly influenced by substrate rotation, this was made by relating the modification of the morphology, grain structure and coating texture

to the former deposition parameter. However there are not many deep studies regarding the effect of substrate rotation on the growth, properties and structure of sputtered thin films, in particular ZnO or AZO coatings [26, 27]. Therefore, in this chapter the effect of substrate rotation speed on the properties of AZO thin films grown by RF-sputtering is explored, showing that this parameter is meaningful to control the roughness, grain size and to obtain homogeneous AZO films with good and adjustable structural, morphological, optical and electrical properties.

6.4 Experimental details

AZO thin films were deposited on Corning 2947 glass substrates. A 3 inch ZnO: Al target with 2 wt% of Al_2O_3 was used to perform the deposition. The target to substrate distance was 60 mm and the base pressure was 6.66 x 10^{-3} Pa. The samples were prepared under different substrate rotation rates of ω_s = 0, 150, 230, 350 and 475 rpm. The sputtering deposition was performed under an RF-power of 80 W at room temperature during 40 minutes with a sputtering Ar pressure of 1.33 Pa. The cross-sectional morphology of the thin films was characterized using field emission scanning electron microscope (FESEM) JEOL 7600F instrument using a 25 kV electron source. The superficial morphology of the thin film was analyzed by atomic force microscopy (AFM) using a Park Scientific Instruments auto probe in the topography contact mode, with Si tips. Structural analysis was accomplished using X-ray diffraction (XRD) in the grazing incidence geometry with an inclination of 1° with a D5000 Siemens X-ray Diffractometer and CuKα radiation (λ =1.5406 Å) operated at 40 kV and 35 mA and aperture diaphragm of 0.2 mm. Transmittance spectra were recorded with the help of an Agilent 8453 UV-Vis spectrophotometer. Resistivity, carrier concentration and mobility values were obtained with an Ecopia HMS-5000 Van der Pauw Measurement System at 300 K.

6.5 Results and discussions

6.5.1 Morphological and structural characterization

Figure 6.3 illustrates the high resolution SEM transversal images of the deposited AZO thin films. Figure 6.3 (a) shows the sample grown with a static substrate, a dense and compact structure is observed. The thin films deposited under substrate rotation showed a columnar structure through all their thicknesses; also it presented a preferential alignment perpendicular to the substrate. The columnar disposition is observed to be dense and without porosities. The formation of a distinct columnar structure due to substrate rotation has been reported by previous works [23, 25]. On the aforementioned works the authors explain that a stationary substrate receives a larger and more energetic flux of adatoms due to the modification of the target-substrate distance produced by the substrate rotation, as it was explained on the introduction. The formation of columnar structures could be explained taking into account the effect of the substrate rotation on the energy of the sputtered species that arrive into the substrate, as it was described by Panich et al. [23]. The energy of the species that reach the substrate decreases as the target-substrate distance increases; this is due the increment in the number of collisions between the gas molecules and the sputtered species contained in the sputtering chamber [24]. Therefore the sputtered species reaching a substrate under rotation are expected to have a smaller energy than those that arrive to

a stationary substrate; this produces a decreasing in the adatoms mobility and the development of a distinct columnar structure. There is no evidence that the gradual increment of the substrate rotation speed affects the thickness of the thin films: they have a central value of ~384 nm with a standard deviation of ~32 nm, showing no definite trend, however, samples grown under substrate rotation are expected to spend less time in front of the substrate which means they have a greater target-substrate distance, therefore their thickness value is always expected to be smaller than the sample under no rotation, which is the case of our results, since the thickness value for the sample grown at ω_S = 0 rpm is the largest (~437 nm) of all the obtained thin films

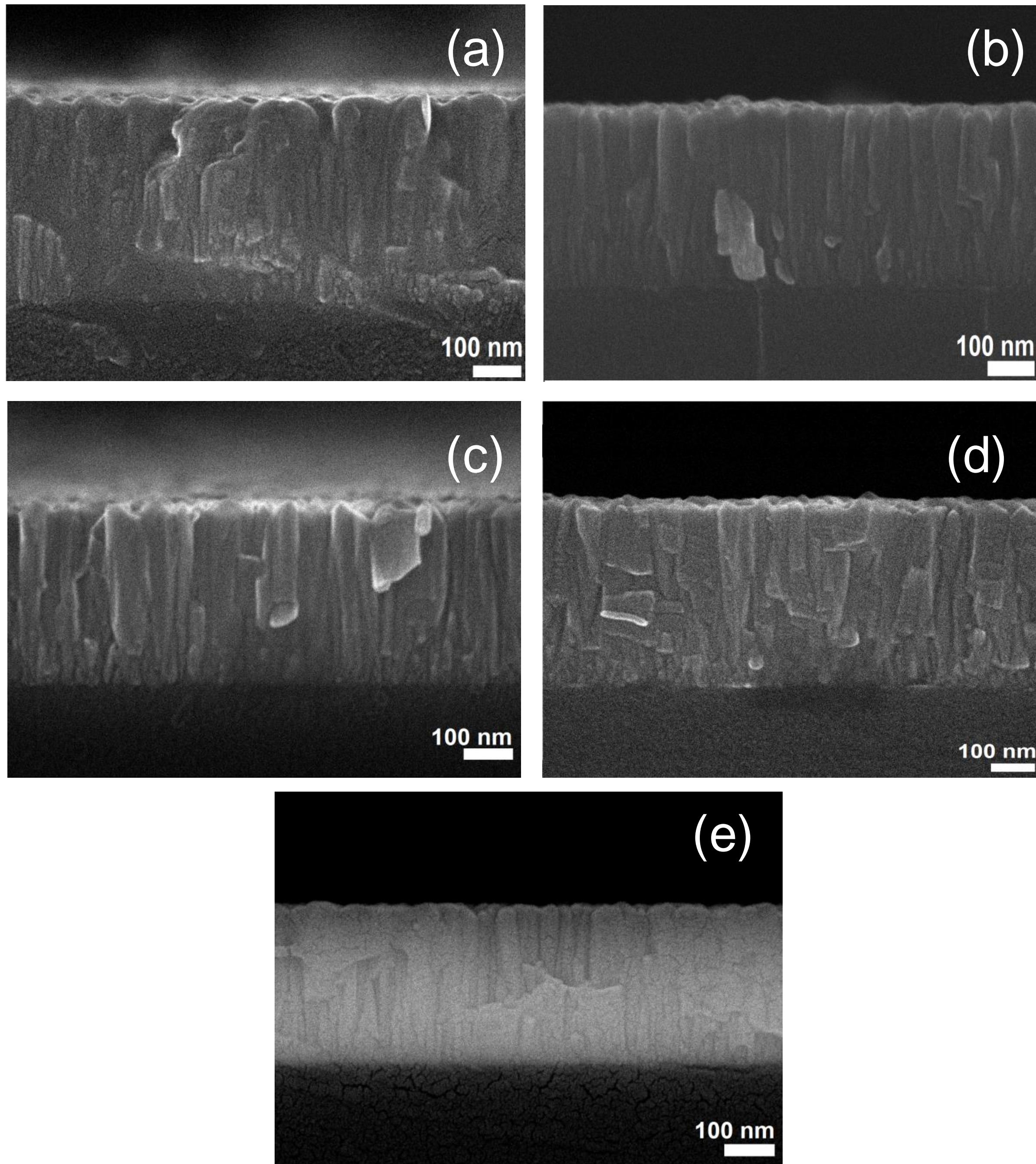

Figure 6.3 Cross-sectional FESEM image of AZO thins films on glass substrate grown at ω_S of (a) 0, (b) 150, (c) 230, (d) 350 and (e) 475 rpm respectively.

Figure 6.4 displays the 2D and 3D AFM images of the AZO thin films obtained in an area of 4 μm^2. The morphology of the samples significantly varied with different substrate rotation velocities. From Figure 6.4 (a) we observed the grain distribution in the film growth with static substrate was not uniform, having large grains in comparison to the samples under substrate rotation, the grains also presented ambigous boundaries, it is also evident that the number of grains is smaller in comparison to the rotationary thin films, higher number of grains means that the average grain size is smaller. When substrate is subjected to rotation, samples deposited at 150 rpm and 230 rpm (Figures 6.4 b-c) confirm noticeable changes, with grains growing with an even distribution of sizes, less scattered and more homogeneous and several large cone-like grains with a structure grown vertical to the substrate surface can be clearly observed, and as the speed increases the grains become denser and more defined. In Figure 6 (d-e) is clear how grains became more structured with cone-like ending features: as ω_S is incremented, the number of observed nanostructures formed (nanocones), seems to rise while becoming more compact in the substrate area, corroborating that the samples have a nanostructured growth but also they become sharper and denser as the substrate speed increases. The explanation for the morphological behaviour of the obtained sample could be explain as follows: The energy of the particles that reach the rotationary substrate is lower than the case of a stationary substrate, resulting in less adatom mobility, this affects the coalescence proceses, making it more kinetically limited than in the case of higher adatom mobility, this leads to the formation of smaller grains. Previous works explained the modification in grain sizes taking into account the energy of particles that arrive to the substrate, presenting a similar diminution in grain size [28, 29].

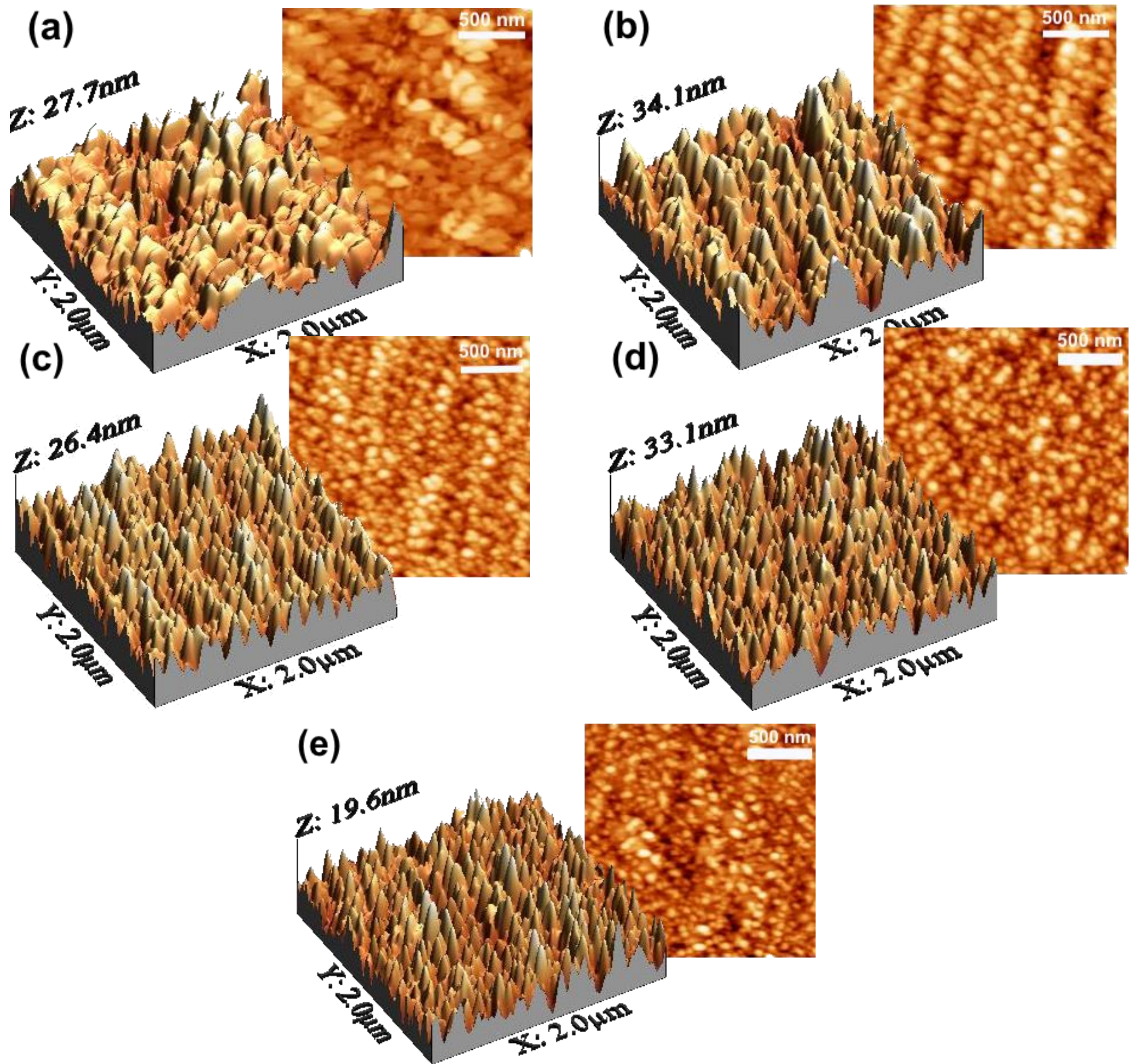

Figure 6.4 AFM images of the AZO thin films with at different ω_s of a) 0, b) 150, c) 230, d) 350 and e) 475 rpm respectively.

In order to carefully study the ending features of the nanostructured grains formed during the deposition of the thin films we employed the Wsxm 5.0 software [30] which possesses a method to calculate statistical quantities from an image. The software mentioned before allowed us to calculate the number of hills (N_h), the first neighbor distances (*FND*) between the nanostructured cones grown on the substrate surface and the root-mean-square surface roughness (RMS) values. The calculated RMS values of the samples were ~3.5, 5.1, 3.6, 4.7 and 2.7 nm, at ω_S of 0, 150, 230, 350 and 475 rpm respectively, these results are presented in Table 6.1. It is noticeable how the rotational speed greatly affects the surface morphology, even if roughness values don't have any defined trend related to ω_S. Figure 6.5 shows the N_h and *FND* plotted against substrate rotation rate; it can be seen that as ω_S increases there is decay tendency in the first hill neighbor distance and an increasing tendency in the number of hills which was tentatively fitted using a Boltzmann sigmoidal curve. These results corroborate that the samples become denser and more packed in the sample area according to the substrate speed and that the number of nanostructures formed increases with the substrate rotation. The roughness value obtained for the thin film grown at ω_S

= 475 rpm was the lowest of all (2.7 nm), which can be explained by its small grain sizes, which were generally the smallest of all the obtained samples, as it is clearly observed in Figure 6.4 (e). This effect has been previously reported by Hyoun et al. and Bortoleto et al. [31, 32], where they both obtained ZnO thin films grown by magnetron sputtering, since their AFM images showed that the RMS value was greater for the samples with larger grain sizes. As explained above, the particles that reach a rotatory substrate will have lower energy than those that reach a stationary one, thus producing smaller grains sizes, resulting in lower RMS values. However, in Figure 6.4 we can clearly observe that even though the grain sizes of the sample grown at ω_S = 0 rpm were generally larger than those of the thin films grown under rotation, the RMS seems to follow no defined trend, rising from 3.5 to reach 5.1 nm and then decreasing to 2.7 nm, presumably due to the different average heights obtained for all the samples, which in turn were employed by the Wsxm 5.0 software to calculate the RMS values using the following equation [32].:

$$\sigma = \sqrt{\frac{1}{N}\sum_{i=1}^{N}(h_i - \langle h \rangle)^2} \tag{6.3}$$

Where N is the number of pixels, h_i the individual heights, and $\langle h \rangle$ the average height. The $\langle h \rangle$ values obtained were ~ 12.6, 16.3, 12.9, 14.4, 7.9 nm for the samples grown at 0, 150, 230, 350 and 475 rpm, respectively, and they are reported in Table 6.1. It is noticeable that the average height value for samples grown at 0 and 230 rpm were similar (both close to 13 nm). This resulted in calculated RMS values that were close i.e. 3.5 and 3.6 nm respectively, which would explain their similar RMS, even though the grain sizes in the former are greater than those in the latter. It is evident that the thin film grown at ω_S = 475 rpm had the smallest average height of all the thin films obtained, in addition with the smallest grain sizes, which would explain the smallest RMS value. As previously mentioned there are minor variations in the thickness of the AZO thin films that follow no defined trend, these differences in thickness would explain the variations on the heights of the surface peaks employed to calculate $\langle h \rangle$, which in turn are used to explain the different RMS values obtained. These results suggest that the average heights along with the grain size are the determinant factors to explain the obtained RMS calculations in our AZO thin films. From the morphological results, we can confirm that ω_S has a major role in the formation and distribution of well-defined nano-grains on the film surface, favoring the formation of a more homogenous films.

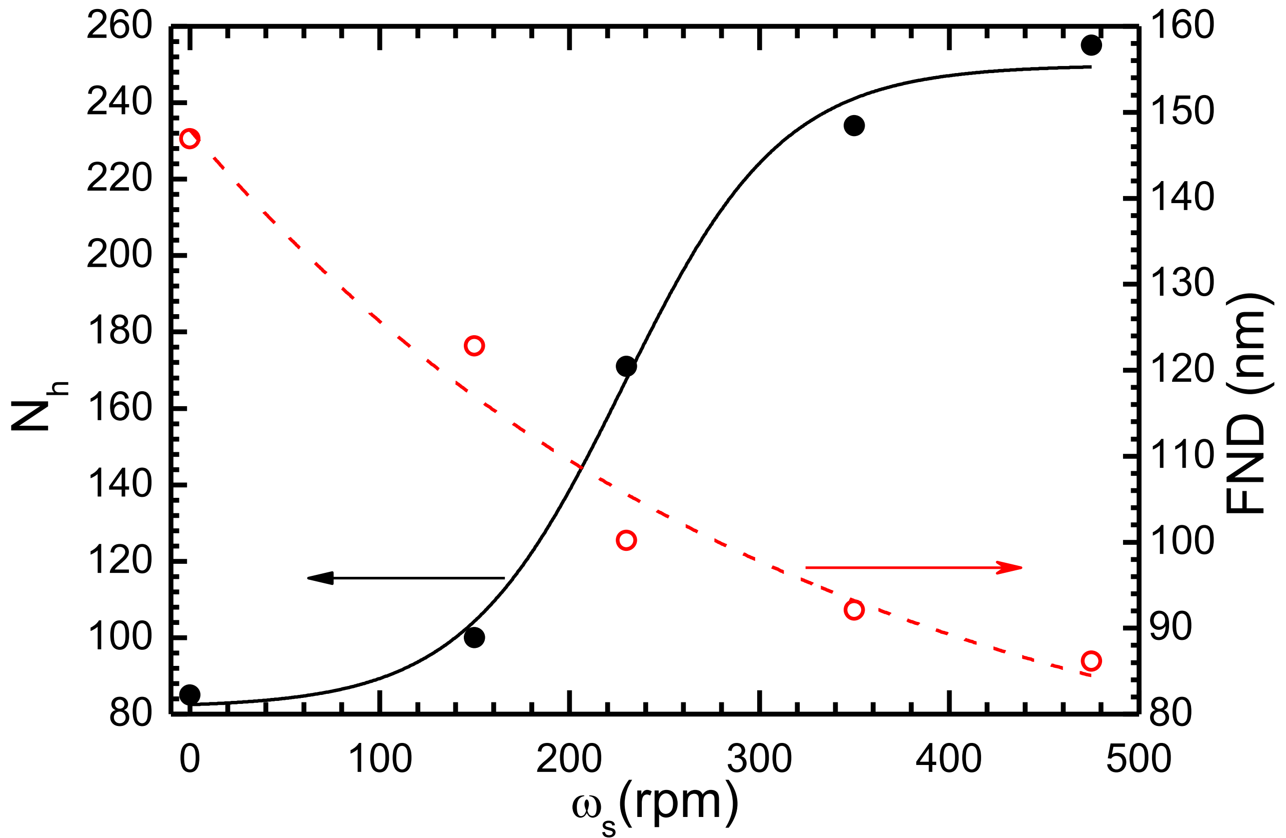

Figure 6.5 Number of hills (Nh) and first neighbor distances (FND) at different substrate velocities.

Figure 6.6 shows the XRD spectra for AZO thin films obtained for different ω_S. The observed diffraction peaks for all samples can be indexed as the ZnO wurtzite structure in the standard data (JCPDS, 36-1451) [33], with preferential orientation in the (002) plane, with the *c*-axis oriented preferentially normal to the substrate surface [34]; all peaks are shifted to the left in their 2θ (002) peak position with respect to the standard value of 34.467° [33] which is evidence of tensile strain [35]. The other peak observed in the XRD patterns can be indexed to the (103) planes. In order to determine crystallite size of the AZO thin films we considered the Scherrer's formula [34], which is given by:

$$D = \frac{0.9\lambda}{\beta Cos\theta} \tag{6.4}$$

Where D is the mean crystallite size, θ the diffraction angle, β is the FWHM and λ is the X-ray wavelength (0.15418 nm). The calculated crystallite sizes, D, of the samples were ~ 24.8, 27.7, 34.7, 31.3 and 29 nm, at ω_S = 0, 150, 230, 350 and 475 rpm respectively, these results are summarized in Table 6.1. There is clear evidence that all the AZO thin films grown under rotation presented bigger crystallite sizes than those films grown on a stationary substrate, meaning that the substrate rotation improves the crystallinity of the thin films. The explanation for this improvement in crystallinity lies in the fact that the species that arrive to a rotating substrate have lower energy than to a stationary one. The time that the substrate spends in front of the target is reduced after increasing the substrate rotation speed; this causes an increasing of the collisions odds between the sputtered particles and the background gas molecules, thus reducing the energy of the sputtered species before reaching the substrate, favoring the energy for

film growth, this produces denser and (002) oriented thin films [27]. The lattice constants were calculated using the following equation [36]:

$$\frac{1}{d_{hkl}^2} = \frac{4}{3}\left(\frac{h^2+hk+k^2}{a^2}\right) + \frac{l^2}{c^2} \tag{6.5}$$

Where a and c are the lattice constants, and d_{hkl} is the crystalline interplanar distance. Using the (002) diffraction peak, this equation becomes $c = 2d_{hkl}$. Furthermore, we calculated the strain ε along the c-axis by using the equation [37]:

$$\varepsilon = \frac{C-C_0}{C_0} \times 100\% \tag{6.6}$$

Where c_0 (0.52069 nm) is the unstrained c lattice parameter of ZnO. Strain and lattice parameters values are shown in Table 6.1. Positive strain values correspond to tensile strain and negative values to compressive strain [37], which agrees with the shifting of the (002) diffractions peaks mentioned before.

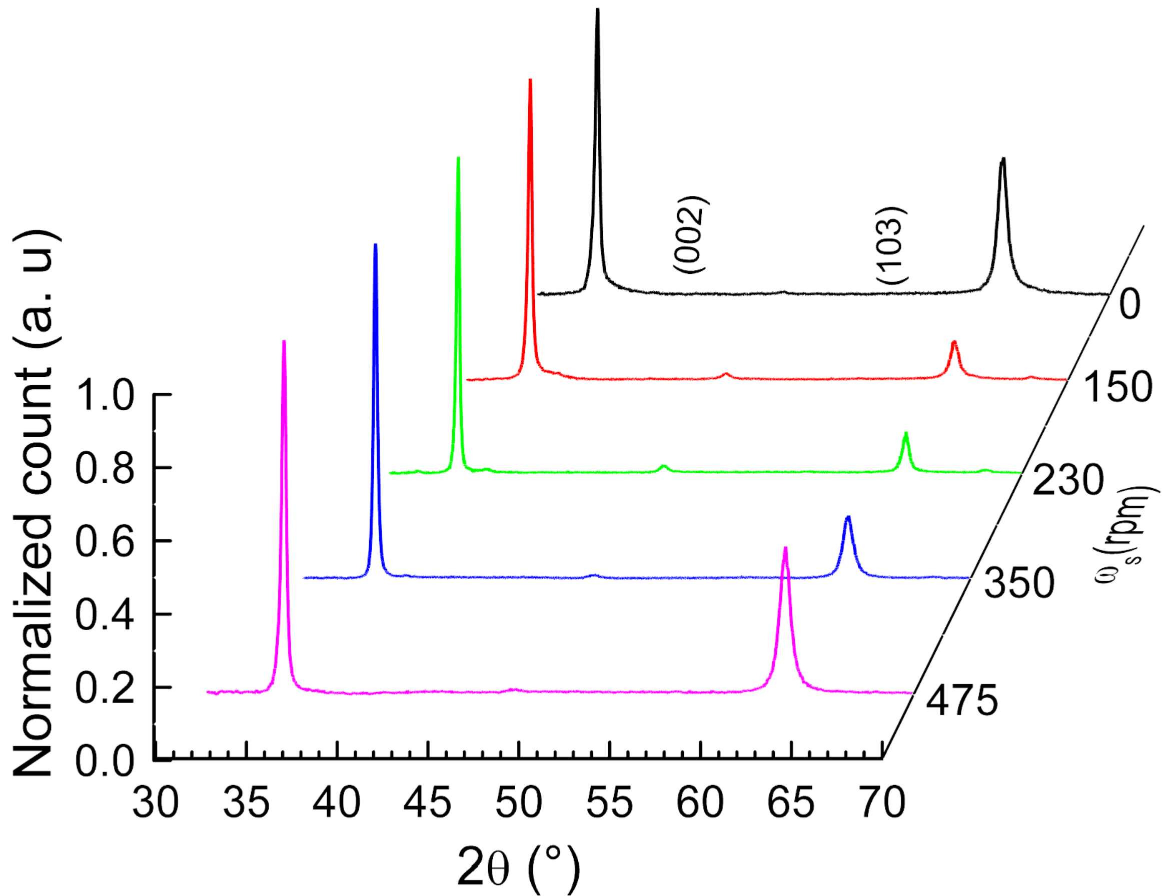

Figure 6.6 XRD patterns of AZO thin films prepared at different rotation velocities.

Figure 6.7 shows the FWHM value and the 2θ position for the (002) planes plotted against the substrate rotation velocity. As the rotation velocity increases, there is a decrement in the value of the FWHM, reaching its minimum for the sample grown at a substrate velocity of 230 rpm, this means that the substrate rotation improves the crystallinity of the thin films. Regarding the 2θ position for the (002) planes it can be seen that all 2θ are shifted to lower values with respect to the standard value for ZnO and

that there is a gradual increasing for the position of the 2θ angle as the substrate velocity increased, this means that the samples that were rotated had closer values to those of the standard which is 34.42° [33]. As it was mentioned before this is evidence of a positive strain, which in turn corresponds to a tensile strain, this suggests that the lattice parameters of the unit cell would show an increasing, this agrees with the reported lattice parameter values summarized in Table 6.1, which are in general bigger than those of the standard ZnO (c_0 = 0.52069 nm and a_0 =0.32495 nm). The explanation of this increment in the lattices parameters is as follows: There two possible ways in which Al atoms are incorporated in the ZnO lattice, either in substitutional or interstitial sites. If Al^{+3} ions are substituting Zn^{+2} ions, the lattice parameter in AZO samples would decrease and this would correspond to a shifting to the right (higher 2θ values) for the (002) peaks in comparison to the standard reported for the ZnO, this is due to the smaller radius of the Al^{+3} (0.054 nm) in comparison of the Zn^{+2} (0.074 nm). Furthermore when Al atoms are incorporated into interstitial sites the lattice parameter increases and this would correspond to a shifting to the left (lower 2θ values) for the (002) peaks [38]. This suggests that the Al atoms might be mostly occupying interstitial sites in the case of the AZO thins films grown in this work. The reported ε values in Table 6.1 show that the samples grown using substrate rotation were under less tensile stress than the samples grown with no substrate rotation. This means that the crystallinity becomes better for thin films under substrate rotation. This is evidence that the crystallinity was greatly influenced by the substrate rotation favoring the formation of bigger crystallite sizes which contributes to the reduction of the tensile stress contribution from crystalline boundaries [30]. These results confirm that the substrate rotation was effective in changing the structural properties of the AZO films. Based on the structural and morphological analysis, the optoelectronic performance is expected to be widely influenced by substrate rotation.

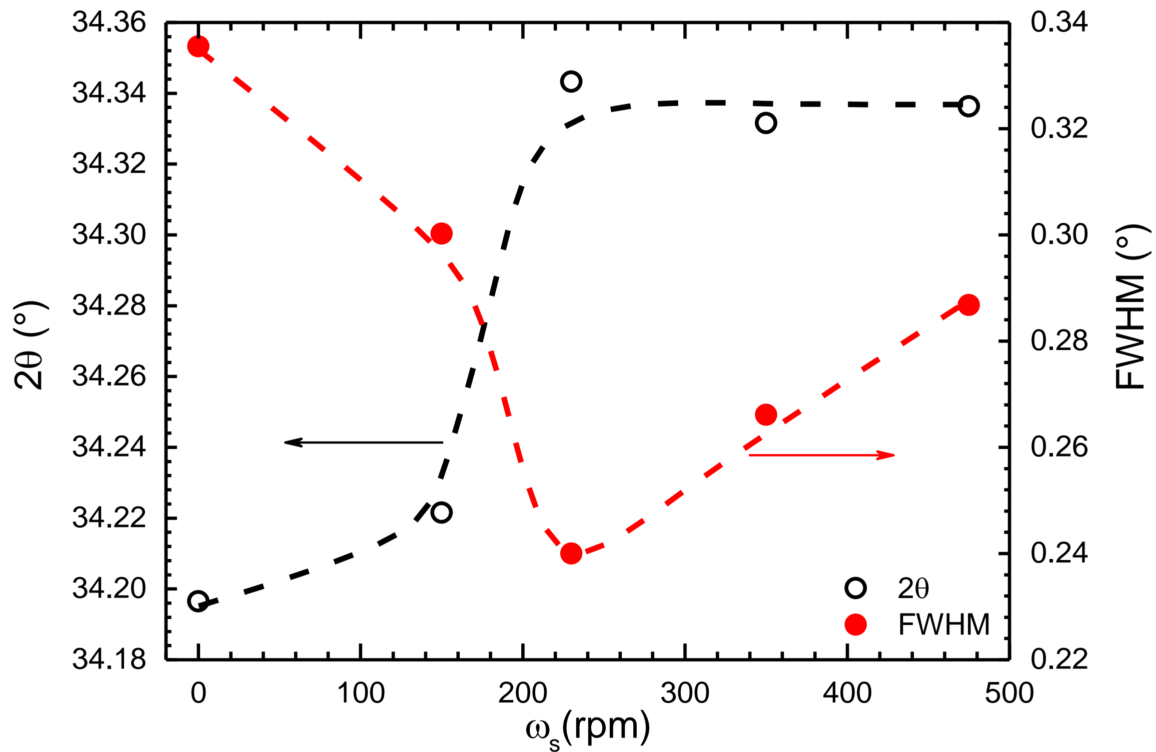

Figure 6.7 Position of the (002) peak and FWHM values at different substrate speed.

Table 6.1 Characteristics of the samples estimated from AFM and XRD data.

Substrate rotation velocity (rpm)	RMS σ (nm)	Crystallite size D (nm)	Lattice parameter *a* (nm)	Lattice parameter *c* (nm)	Strain of the c-axis ε (%)	Average Height <h> (nm)
0	3.5	24.8	0.325	0.524	0.634	12.6
150	5.1	27.7	0.326	0.523	0.442	16.3
230	3.6	34.7	0.325	0.522	0.250	12.9
350	4.7	31.3	0.325	0.521	0.058	14.4
475	2.7	29	0.324	0.522	0.250	7.9

6.5.2 Optical characterization

Figure 6.8 shows the transmission spectra of the samples obtained at different substrate speeds. It is possible to observe oscillations in the high wavelength range due to optical interference, typical in very thin films. The average transmittance over the 400-800 nm range exceeds 90% regardless of the substrate rotation speed. We calculated the optical energy gap using the Tauc equations for all samples considering AZO a direct band gap *n*-type semiconductor obtained from the $(\alpha h\nu)^2$ versus $h\nu$ plot by extrapolating

the linear portion of the curve to ($h\nu$ =0) [40]. The bandgap values were ~3.49, 3.67, 3.65, 3.61, 3.49 eV for the samples grown at ωs = 0, 150, 230, 350 and 475 rpm respectively. All bandgap values presented increased values respect of the standard ZnO, which is in the range of 3.20-3.40 eV. The higher band gap of the present AZO thin films compared with the bulk ZnO film could be attributed to the Burstein Moss effect [41]. The widening of the band gap was caused by increasing of the free electron concentration after doping with Al^{+3} ions; in degenerate semiconductors this causes an increasing of Fermi level, therefore optical band gap of doped zinc oxide is broader than that of undoped zinc oxide films [42].

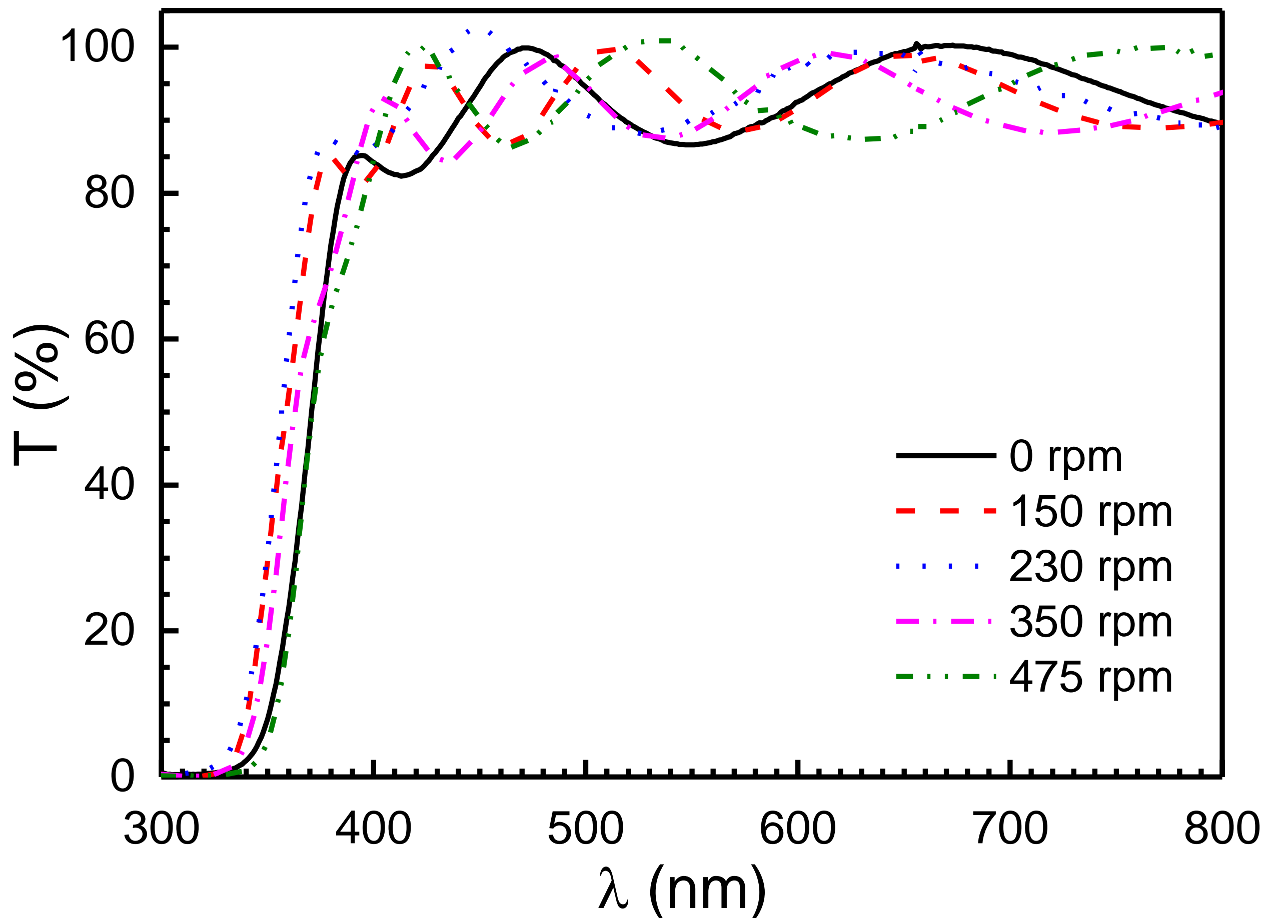

Figure 6.8 Optical transmittance spectra of AZO thin films.

6.5.3 Electrical characterization

The conduction mechanisms in ZnO are attributed to two main factors: The electrons generated from oxygen vacancies and the interstitial Zn Atoms [43]. Due to the incorporation of Al^{+3} on substitutional sites of Zn^{+2} or Al atoms into interstitial sites, as well as oxygen vacancies and Zn interstitial atoms, the electrical conductivity in Al doped ZnO thin films is expected to be higher than in pure ZnO films [38]. The electrical properties of the deposited AZO thin films as a function of the substrate rotation speed are plotted in Figure 6.9. All AZO thin films produced Hall voltages that indicated an *n*-type behavior. The experimental data revealed that as the substrate speed increases the resistivity also increases as the substrate velocity raised in value. The resistivity was increased from its minimum value of 8.5 x 10^{-3}

Ω cm at ω_S = 0 rpm to a maximum of 2.7 x 10^{-2} Ω cm at ω_S = 350 rpm, while for all remaining samples the resistivity was in the order of 10^{-2} Ω cm. Since ρ is proportional to the reciprocal of the product of the carrier concentration *n* and mobility μ, the variations in resistivity with substrate rotation speed are attributed to the change in both *n* and μ. At 0 rpm *n* is ~ 1.8 × 10^{20} cm^{-3} with a Hall mobility of 4.19 cm^2/Vs and remains in the order of 10^{20} cm^{-3} up to 230 rpm, with a Hall mobility of 3.50 cm^2/Vs. Then *n* rapidly decreases and reaches its lowest carrier value at ω_s = 350 rpm (1.29 x 10^{19} cm^{-3}), with the highest value of Hall mobility (18.1 cm^2/Vs), and then increases again to a value of 9.1 x 10^{19} cm^{-3}, for ω_s = 475 rpm, with a Hall mobility of 3.23 cm^2/Vs. We speculate that since the grain size in the AZO thin films was decreased, the resistivity increased due to scattering with grain boundaries [44]. Also the thin films grown under rotation had grains which were more uniform and denser than those presented in the sample grown using a stationary substrate, this type of microstructure contains fewer pores and projections, which act as traps for the free carriers and barriers for transporting the carriers in the films [45]. We suggest that the modification of the morphological and structural properties of our samples by rotating the substrate affected the Hall mobility and carrier concentrations, thus modifying the electrical conductivity. All of these results suggest that the substrate rotation plays an important role in the electrical properties of AZO thin films.

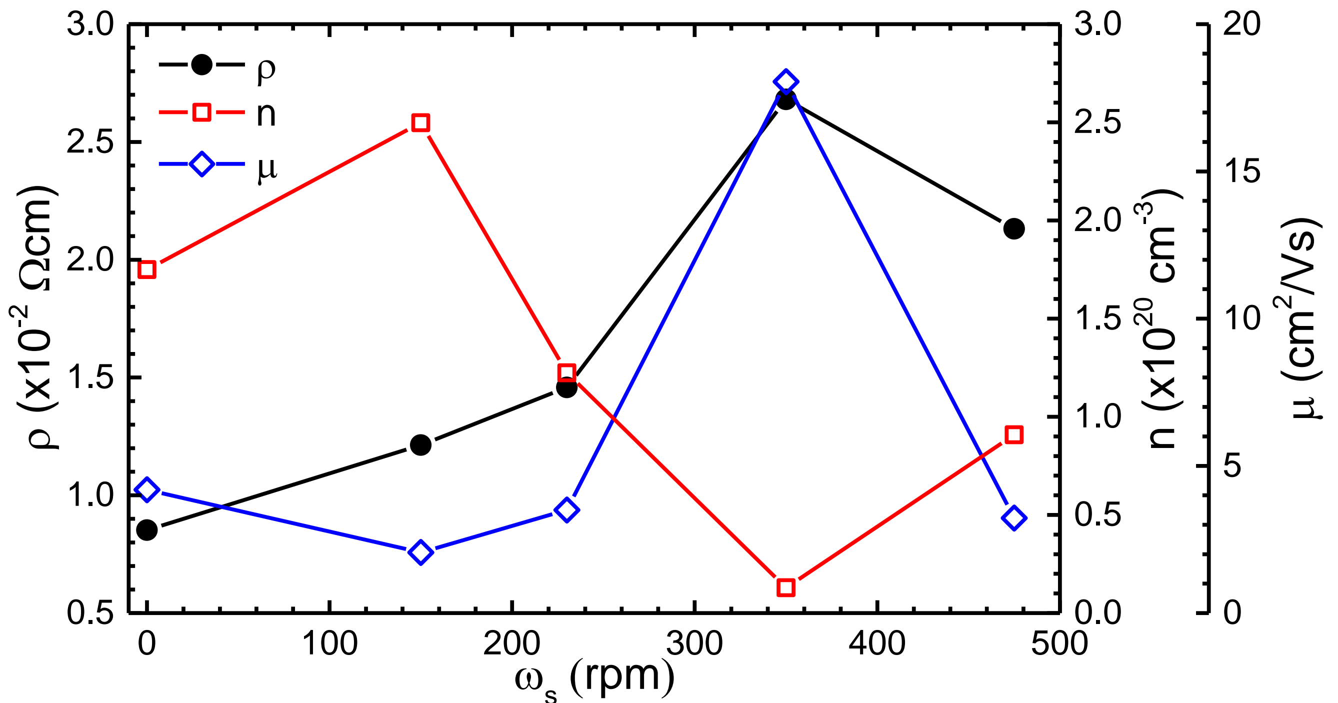

Figure 6.9 Electrical properties of AZO thin films deposited at different substrate rotation velocities.

6.6 Partial conclusions

AZO thin films were deposited at different substrate rotation rates by RF-magnetron sputtering on glass substrates. We applied several techniques such as scanning electron microscopy, X-ray

diffraction, UV-vis and the Van der Pauw technique to analyze the properties of the AZO thin films. Structural properties showed that all samples had grown at a preferential orientation in the (002) plane direction and that the substrate rotation increases the crystallinity. Morphology results showed that substrate rotation produces highly defined nanostructures that became denser and sharper with ω_s. All films presented a transmittance higher than 90% in the visible range, and the estimated optical energy gaps were in the range of 3.49 to 3.67 eV. The electrical properties showed the lowest resistivity was achieved with a static substrate (8.5 x 10^{-3} Ω cm), and that the substrate rotation induced changes in the carrier concentration and hall mobility which resulted in the increasing of electrical resistivity of the AZO thin films.

6.7 References

[1] C. Kittel, Introduction to Solid State Physics, John Wiley and Sons, New York, 7th edn, 1996.

[2] R M. Pasquarelli, D S. Ginley and R O'Hayre, Solution processing of transparent conductors: from flask to film, Chemical Society Reviews, 40 (2011) 5406- 5441.

[3] Y. Li, G.S. Tompa, S. Liang, C. Gorla, Y. Lu, J. Doyle, Transparent and conductive Ga-doped ZnO films grown by low pressure metal organic chemical vapor deposition, Journal Vacuum Science & Technology A, 15 (1997) 1063.

[4] B. Rech, H. Wagner, Potential of amorphous silicon for solar cells, Applied Physics A, 69 (1999) 155-167.

[5] U. Rau, D. Braunger, H.W. Schock, Air-Annealing effects on polycrystalline Cu(In, Ga)Se_2 heterojunctions, Solid State Phenoma 67-8 (1999) 409-414.

[6] Anuj R Madaria, Akshay Kumar and Chongwu Zhou, Large scale, highly conductive and patterned transparent films of silver nanowires on arbitrary substrates and their application in touch screens, Nanotechnology 22 (2011) 245201 (7pp).

[7] K.L. Chopra, S. Major, D.K. Pandya. , Transparent conductors—A status review, Thin Solid Films, 102 (1983) 1-46.

[8] J. H. W. Dewit, Preparation of In_2O_3 single-crystals via chemical transport reaction, Journal of Crystal Growth 12 (1972) 183-184

[9] Vattappalam S C, Thomas D, Matthew T R, Augustine S and Mathew S, Band gap and conductivity variations of ZnO nano structured thin films annealed under vacuum, IOP Conference Series: Materials Science and Engineering 73 (2015) 012107.

[10] Shou-Yi Chang, Yen-Chih Hsiao, Yi-Chung Huang. Preparation and mechanical properties of aluminum-doped zinc oxide transparent conducting films. Surface and Coatings Technology 202 (2008) 5416-5420.

[11] Shen Hong-Lie, Zhang Hui, Lu Lin-Feng, Jiang Feng, Yang Chao. Preparation and properties of AZO thin films on different substrates. Progress in Natural Science: Materials International 20 (2010) 44-48.

[12] Mondal S, Bhattacharyya S R, Mitra P. Effect of Al doping on microstructure and optical band gap of ZnO thin film synthesized by successive ion layer adsorption and reaction. Pramana – Journal of Physics 80 (2013) 315–326.

[13] Lei Po-Hsun, Hsu Chia-Ming, Fan Yu-Siang, Ye Sheng-Jhang. Improved efficiency of InGaN/GaN light-emitting diodes with Al-doped zinc oxide using dual-plasma-enhanced metal-organic chemical vapour deposition system. International Journal of Nanotechnology, 11 (2014) 359.

[14] Liu Chaoying, Xu Zhiwei, Zhang Yanfang, Fu Jing, Zang Shuguang, Zuo Yan. Effect of annealing temperature on properties of ZnO: Al thin films prepared by pulsed DC reactive magnetron sputtering. Materials Letters 139 (2015) 279-283.

[15] Moreno L., Sánchez-Aké C., Bizarro M. Double-beam pulsed laser deposition for the growth of Al-incorporated ZnO thin films. Applied Surface Science, 302 (2014) 46-51.

[16] Mohanta A., Simmons J.G., Everith H.O., Sheng G., Kim S. M., Kung P. Effect of pressure and Al doping on structural and optical properties of ZnO nanowires synthesized by chemical vapor deposition. Journal of Luminescence 146 (2014) 470–474.

[17] T.G. Silva, E. Silveira, E. Ribeiro, K.D. Machado, N. Mattoso, I.A. Hummelgen. Structural and optical properties of ZnO films produced by a modified ultrasonic spray pyrolysis technique. Thin Solid Films 551 (2014) 13-18.

[18] Kim Young-Sung, Tai Weon-Pil. Electrical and optical properties of Al-doped ZnO thin films by sol–gel process. Applied Surface Science 253 (2007) 4911–4916.

[19] Fernandez S., Martinez-Steele A., Gandia J. J., Naranjo F. B. Radio frequency sputter deposition of high-quality conductive and transparente ZnO:Al films on polymer substrates for thin film solar cells applications.Thin Solid Films 517 (2009) 3152-3156.

[20] Jiang Jinlong, Wang Qiong, Huang Hao, Wang Yubao, Zhang Xia, Hao Junying. Microstructure and property changes induced by substrate rotation in titanium/silicon dual-doped a-C:H films deposited by mid-frequency magnetron sputtering [J]. Surface and Coatings Technology 240 (2014) 419-424.

[21] Siyanaki F. H., Dizaji H. R., Ehsani M. H., Khorramabadi S. The effect of substrate rotation rate on physical properties of cadmium telluride films prepared by a glancing angle deposition method.Thin Solid Films 577 (2015) 128-133.

[22] Castro-Rodriguez R., Mendez-Gamboa J., Perez-Quintana I., ,Medina-Ezquivel R. CdS thin films growth by fast evaporation with substrate rotation. Applied Surface Science 257 (2011) 9480-9484.

[23] Panich N., Sun Y. Effect of substrate rotation on structure, hardness and adhesion of magnetron sputtered TiB_2 coating on high speed steel. Thin Solid Films 500 (2006) 190– 196.

[24] Wasa Kiyotaka, Hayakawa Shigeru. Handbook of Sputter Deposition Technology: Principles, Technology, and Applications. Park Ridge, N.J., U.S.A: Noyes Publications, 1992.

[25] Wada K., Yamaguchi N., Matsubara H. Effect of substrate rotation on texture evolution in ZrO_2-4 mol.% Y_2O_3 layers fabricated by EB-PVD. Surface and Coatings Technology 191 (2005) 367-374.

[26] Jayaraman V. K., Kuwabara Y. M., Alvarez A. M., Amador M. D. L. L. O. Importance of substrate rotation speed on the growth of homogeneous ZnO thin films by reactive sputtering .Materials Letters 169 (2016) 1-4.

[27] Shi Qian, Dai Ming-Jiang, Lin Song-Sheng, Hou Hui-Jun, Wei Chun-Bei, Hu Fang. Effect of sputtering conditions on growth and properties of ZnO:Al films. Transactions of Nonferrous Metals Society of China 25 (2015) 1517-1524.

[28] Jun Yeon Sik, Lee Dong Wook, Jeon Duk Young. Influence of dc magnetron sputtering parameters on surface morphology of indium tin oxide thin films. Applied Surface Science, 221 (2004) 136–142.

[29] Hua Qin, Ligang Wang, Ruijin Liu, Wenfeng Yuan. Influence of target substrate distance on the properties of transparent conductive Si doped ZnO thin films. Optik 125 (2014) 3902–3907.

[30] Horcas I., Fernández R., Gómez-Rodríguez J. M., Colchero J., Gómez-Herrero J., Baro A. M. WSXM: A software for scanning probe microscopy and a tool for nanotechnology. Review of Scientific Instruments 78 (2007) 1-8.

[31] Hyoun Woo Kim, Nam Ho Kim. Structural studies of room-temperature RF magnetron sputtered ZnO films under different RF powered conditions. Materials Science and Engineering B103 (2003) 297-302.

[32] Bortoleto J. R. R., Chaves M., Rosa A. M., Da Silva E. P., Durrant S. F., Trino l. D., Lisboa-Filho P. N. Growth evolution of self-textured ZnO films deposited by magnetron sputtering at low temperatures. Applied Surface Science 334 (2015) 210-215.

[33] Santi Maensiri, Paveena Laokul, Vinich Promarak. Synthesis and optical properties of nanocrystalline ZnO powders by a simple method using zinc acetate dehydrate and poly (vinyl pyrrolidone). Journal of Crystal Growth 289 (2006) 102-106.

[34] Lee Ka Eun, wang mingsong, kim eui jung, hahn sung hong. Structural, electrical and optical properties of sol–gel azo thin films. Current Applied Physics 9 (2009) 683–687.

[35] Zak A. K., Majid W. H. A., Abrishami M. E., Yousefi R. X-ray analysis of zno nanoparticles by williamson-hall and size-strain plot methods. Solid State Sciences 13 (2011) 251-256.

[36] Fang G. J., Li D. J., Yao B L. Effect of vacuum annealing on the properties of transparent conductive AZO thin films prepared by DC magnetron sputtering. Physica Status Solidi (A) 193 (2002) 139-152.

[37] Ghosh R., Basak D, Fujihara S. Effect of substrate-induced strain on the structural, electrical, and optical properties of polycrystalline ZnO thin films. Journal of Applied Physics, 96 (2004) 2689-2692.

[38] Park Ki Cheol, Ma Dae Young, Kim Kun Ho. The physical properties of Al-doped zinc oxide films prepared by RF magnetron sputtering. Thin Solid Films 305 (1997) 201-209.

[39] Yildiz A., Cansizoglu H., Turkoz M., Abdulrahman R., Al-hilo Alaa, Cansizoglu M. F., Demirkan T. M., Karabacak T. Glancing angle deposited Al-doped ZnO nanostructures with different structural and optical properties. Thin Solid Films 589 (2015) 764–769.

[40] Al-Ghamdi A. A., Alhumminay H., Abdel-Wahab M. S., Yashia I. S. Structure, optical constants and non-linear properties of high quality AZO nano-scale thin films. Optik 127 (2016) 4324–4328.

[41] Grilli M.I., Sytchkova A., Boycheva S., Piegari A. Transparent and conductive Al-doped ZnO films for solar cells applications. Physica Status Solidi (A) Applications and Material Science 210 (2013) 748–754.

[42] Sun Yi-hua, Wang Hai-lin, Chen Jian, Fang Liang, Wang Lei. Structural and optoelectronic properties of AZO thin films prepared by RF magnetron sputtering at room temperature. Transactions of Nonferrous Metals Society of China 26 (2016) 1655−1662.

[43] Igasaki Y., Saito H. Substrate temperature dependence of electrical properties of ZnO:Al epitaxial films on sapphire (1210). Journal Applied Physics 69 (1991) 2190-2195.

[44] Mayadas A. F., Shatzkes M. Electrical-Resistivity Model for Polycrystalline Films: the Case of Arbitrary Reflection at External Surfaces. Physical Review B 1 (1970) 1382-1389.

[45] Liu Y. Y., Yang S. Y., Wei G. X., Song H. S., Cheng C. F., Xue C. S., Yuan Y. Z. Electrical and optical properties dependence on evolution of roughness and thickness of Ga: ZnO films on rough quartz substrates. Surface Coatings Technology 205 (2011) 3530-3534.

Chapter 7 Tuning of refractive index in Al-doped ZnO films by rf-sputtering using oblique angle deposition

This chapter describes the results obtained from the deposition of Al-doped ZnO thin films grown by RF-sputtering using the oblique angle deposition method (OAD). The tilting angle of the obtained AZO nanostructures and its relation with the optical properties, especially the refractive index was investigated. Nanostructured columns of AZO thin film with different tilting angles and refractive indexes were deposited; additionally the structural, morphological and optical properties were studied in order to explain the relationship between each other. The nanocolumnar tilting of the thin films resulted in a 16% change in the refractive indices of the obtained samples, the columnar tilt changed from 0° to 13.5°, which corresponded to substrate inclination from 0° to 75°, respectively. Band gap energy was found to diminish, which was associated to a local redistribution of Al concentration x in the $Al_xZn_{1-x}O$ solid solution around the $x \approxeq 0.02$ average.

7.1 Introduction

7.1.1 Fundamentals of the Oblique Angle Deposition method

In many physical vapor deposition (PVD) techniques there are a variety of growth parameters that modify the obtained properties of the deposited thin films, e.g., Crystal structure, optoelectronic and morphological properties; among them, the angle between the direction of the incoming particle flux and the normal to the surface of the substrate plays an important role in the morphology of the thin films [1]. Within this context, the Oblique Angle method (OAD) arises as an effective method to fabricate unique nanostructures and diverse nano-architectures which has enabled researchers to develop unique nanostructures with tailored morphology due the fact that it takes advantage of physical vapor deposition processes based on evaporation [2].

The OAD method is a deposition process in which the substrate is held at an oblique angle (θ), with respect to the source of evaporation [3], this contrasts with the conventional deposition method where the flow of particles of material emanating from the source reaches the substrate with a direction parallel to its normal. Additionally, this technique could be employed along with the rotation or control of the substrate's position with respect to the vapor source, this is called the Glancing Angle Deposition (GLAD) technique, and is has proven to be a useful technique to deposited nano-sized columnar films with controlled porosity and shapes [4-8]. Figure 7.1 shows a schematic diagram for the oblique angle deposition technique.

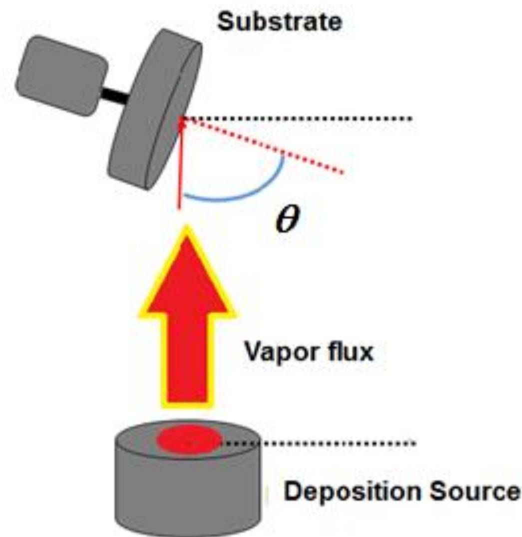

Figure 7.1 Schematic of an OAD setup.

The growth mechanism in OAD is called shadowing effect. This effect begins at the very early stages of deposition, when random nuclei centers are formed on the substrate's surface (Figure 7.2 a). As the deposition process continues the nuclei growth in such a way that prevent the arrival of any further evaporated material to areas which have no nuclei, thus producing "shadowed" areas (Figure 7.2 b). Hence the taller nuclei will receive more material from de vapor flux in comparison to the smaller ones; this prevents the smaller islands from growing any further and leads to the formation of a distinct columnar growth (Figure 7.2 c). Eventually only the top of the tallest columnar structures will continue receiving more vapor flux, thus the smallest columns and nuclei will stop growing, leading to a columnar growth tilted towards the vapor source with a columnar angle β (Figure 7.2 d), this process is called columnar extinction [9]. The columnar structure of the deposited thin film will be heavily influenced by adatom mobility and the shadowing effect. One dimensional nanostructures fabricated by OAD and GLAD have a diverse number of applications, e.g., antireflection coatings [10, 11], omnidirectional reflectors [12], superhydrophobic coatings [13], solar cells [14], sensors [15], photonic band-gap crystals [16], etc.

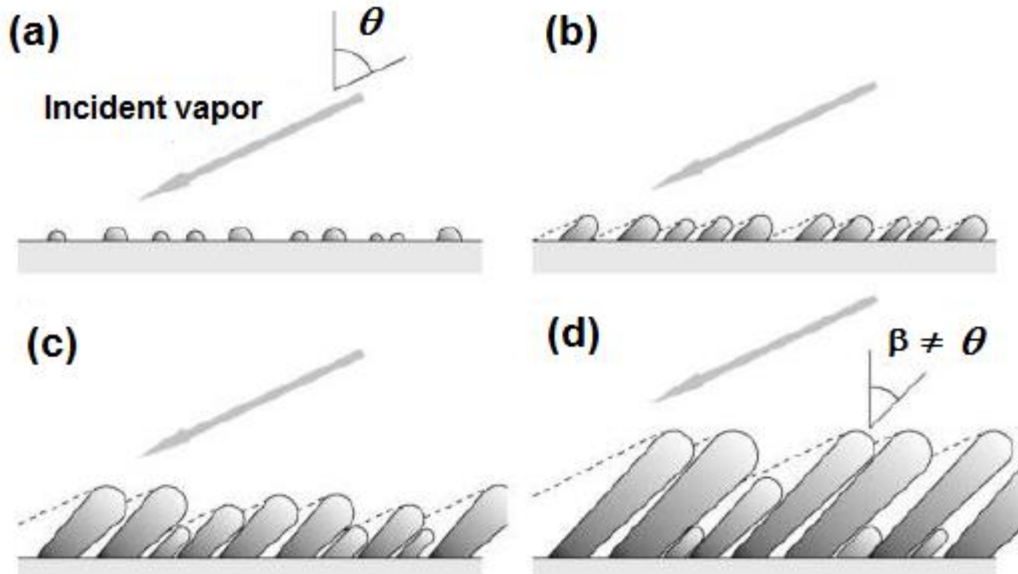

Figure 7.2 OAD growth mechanisms schematically represented [9] (a) Initial arrival of the vapor flux to the substrate in an oblique angle (b) Nuclei centers growth by shadowing effect (c) Columnar growth (d) Columnar extinction by shadowing effect.

Usually the flux incidence angle (θ) is larger than the columnar tilting angle (β) and there have been many attempts to mathematically correlate them [17-20]. Many deposition parameters affect the value of β, namely, substrate temperature, deposition rate, angular distribution of the deposition vapor flux, and the pressure within the vacuum chamber [21]; however, the most widely used heuristic expressions to correlate θ and β are the tangent rule proposed by Nieuwenhuizen and Haanstra [22], which is valid for small values of θ ($\theta \leq 50$) [18]:

$$Tan\,\beta = \frac{1}{2} Tan\,\theta \tag{7.1}$$

Or the cosine rule proposed by Tait et al. employing a purely ballistic model, which applies for higher values of θ [23, 24]:

$$\beta = \theta - arcsin\left(\frac{1 - Cos\theta}{2}\right) \tag{7.2}$$

These expressions suggest that the vapor flux must be directed towards the substrate at a large incidence angle if a highly tilted columnar structure is desired, which in turn will result in a porous film due to the shadowing effect. On the contrary, a flux arriving perpendicularly into the substrate's surface will lead to a nearly columnar growth, resulting in a tightly packed structure [17, 18]. In spite of some concordances, none of these expressions can successfully predict the relationship between the aforementioned angles, failing to account for most of the experimental data. Nonetheless, in recent years Alvarez et al. have proposed a more accurate model to predict the dependence between θ and β which takes into account the interaction between the deposition particles and the surface of the deposited

material, this new model was called "surface trapping mechanism" and it's based on atomistic considerations[25, 26].

Figure 7.3 shows six examples of nanostructures, specifically of TiO_2 fabricated by the OAD method, varying different geometric parameters and growth conditions, which were designed to manipulate the shadowing conditions during growth in different ways, all images are visualized as SEM micrographs. Figure 7.3 (a) shows the cross section image of slanted nanostructured growth [27], as it was mentioned before the columnar inclination angle β will be depended on the incident flux angle θ, this tilted columnar structure is typical of thin films grown using the OAD technique and will change into more complex structures if the substrate is manipulated during deposition, specifically:

- Zigzag structures (Figure 7.3 b) [28]: Columnar structures where their directions changes back and forth will be produce with large values of θ combined with alternating directions.
- Helical structures (Figure 7.3 c) [9]: Slow rotation and large values of θ will continually redirect the columnar orientation thus producing helical structures.
- Vertical columns (Figure 7.3 d) [9]: Both high substrate rotation speeds coupled with a large value of θ produces vertical columnar structures.
- Graded-density structures [28] (Figure 7.3 e): The modulation of θ between high and low values changes the density and diameter of the columnar structure.

Most of these nanostructured thin films are also obtained for other materials besides TiO_2, and find many useful applications such as: humidity sensors [29], microbatteries [30], catalytic nanomotors [31], surface-enhanced Raman spectroscopy [32], hydrogen storage [33], photocatalysis [34], among others.

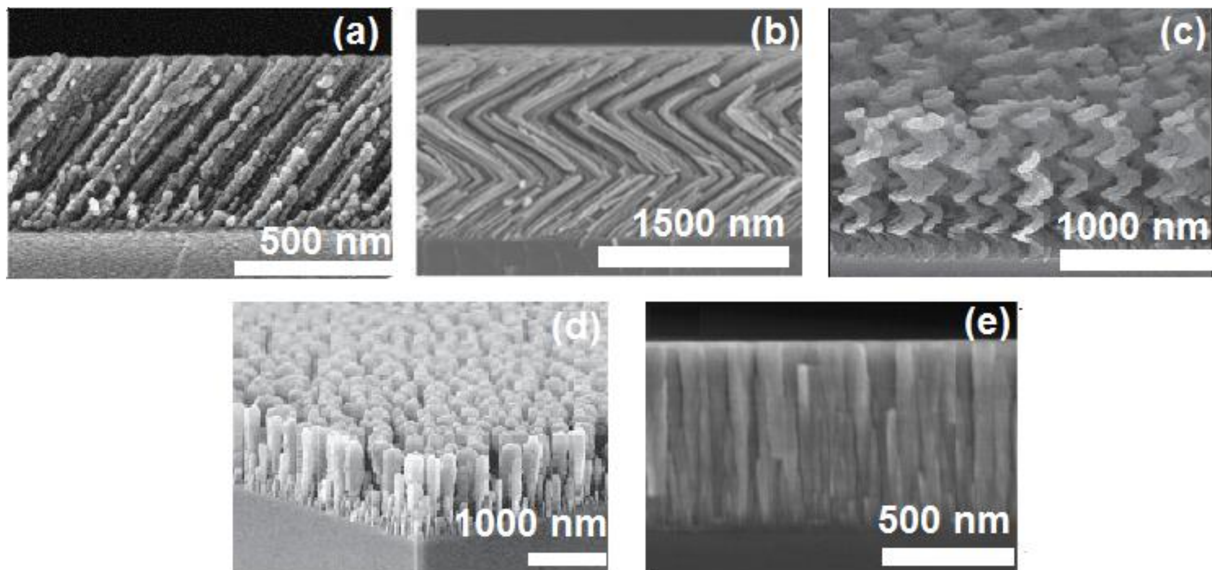

Figure 7.3 Archetypal OAD fabricated nanostructures, (a) slanted columns, (b) zigzag columns, (c) helical columns, (d) vertical columns and (d) graded-density columns.

7.1.2 Importance of Al-doped zinc oxide as TCO

As it was mentioned in chapter 6, there are certain types of materials in which a high electrical conductivity and optical transparency are desirable. Those materials are called transparent conductive oxides (TCO's), it was also stated that these materials had many applications, e.g., flat panel displays, thin film solar cells, and transparent thin film transistors [35–37]. Among them, Tin Indium Oxide (ITO) is regarded as one of the best TCO's because it presents both high electrical conductivity and optical transparency; however it is very scarce and expensive, so there are continuous efforts to find a suitable substitute material. One of the promissory materials is zinc oxide (ZnO) due to its abundance, high transparency, low cost, *n*-type conductivity, wide band gap (Eg ~ 3.4 eV) and large exciton binding energy (60 meV) [38, 39], this makes it an attractive TCO material with many potential. Extrinsic dopants are employed to modify and improve the electrical and optical properties of ZnO. One of these dopants is aluminum, which has been used for producing thin films with high transparency above 90% in the visible spectrum, as well as low electrical resistivity [35]. Al-doped ZnO (AZO) is the most promising material to substitute ITO as TCO due to its cheapness, plentiness and non-toxicity. In order to obtain AZO thin films many deposition techniques have been employed, such as e-beam evaporation, pulsed laser deposition, chemical vapor deposition and RF-sputtering [40–43].

7.1.3 ZnO as antireflective coating

As it was described in chapter 6, when light passes through any material, some of it will be absorbed, transmitted and reflected, particularly in uncoated glass substrates approximately 4% to 6.5% will be reflected at the air-substrate interface [44]. This leads to an inevitable energy loss due to reflected radiation that is detrimental in many technological applications where there are several optical components involved, for example solar cells. One way to solve this, is the implementation of materials which play the role of reducing surface reflection, this materials are called antireflection coatings (ARC's). Anti-reflective layers are placed in many substrates so that interference effects force the reflected waves from the inner surfaces (layer/substrate interface) become out of phase with the waves reflected by their outer surfaces (air/layer interface). Out-of-phase reflected waves destructively interfere with each other, resulting in zero reflected energy. The interference processes described above are illustrated in Figure 7.4, where n_0, n_1, n_2 represent the refractive indices of the air, the deposited coating (either ARC or not), and the substrate, respectively, d_1 represents the thickness of the coating.

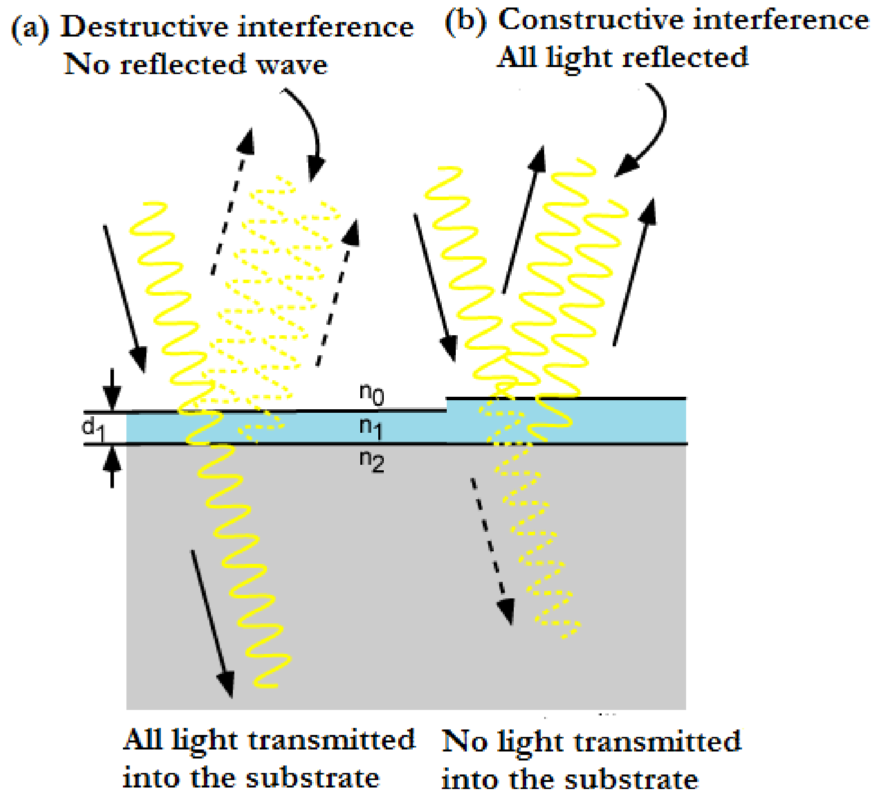

Figure 7.4 Interference process of light in a (a) ARC material and (b) non ARC material.

There are many parameters that affect the transmission properties of a certain material, namely, the substrate's index of refraction, the index of refraction of the coating, the thickness of the coating, and the angle of the incident light. The refractive index is one of the fundamental parameters regarding the optical properties of an ARC; it also has a major importance at the interfaces made between different coatings. Therefore being able to fine-tune its value is of high importance for many technological applications in which light reflection and refraction take place. Light reflection is one of the critical problems to solve for the performance of the optoelectronic devices, such as solar cells [45]. This is due to the Fresnel reflections that reduce the intensity of transmitted light across the TCO, thus decreasing efficiency [46]. By using antireflection coatings (ARCs), the light reflection can be reduced and the cell efficiency enhanced. Current researches study ARCs materials applied to the solar cell technology area and a variety of low refractive index materials and fabrication methods have been developed to improve the device's performance [47].

The manipulation of morphological properties on thin films allows controlling the optical properties [48]. For example, changes in the porosity of the layers have been used for modifying the refractive index in several materials [49, 50]. ARCs are used to reduce the reflection over a wide range of wavelengths and incident angles, in order to approach the full spectra of incident light. However, the conventional quarter-wavelength ARC can reduce the reflection on a specific wavelength and incident angle using the conditions:

$$n_{ARC} = \sqrt{n_1 n_2} \quad (7.3)$$

$$t = \frac{\lambda}{4n_{ARC}} \quad (7.4)$$

Where n_{ARC} is the refractive index of the ARC layer, while n_1 and n_2 are the refractive indexes of the adjacent layers to the ARC, λ is the selected wavelength of the incident light, and t is the optimal thickness for destructive interference at λ. Also, it is well known that an ARC with graded refractive index shows broadband and omnidirectional characteristics [51], thus reducing more efficiently the losses by reflection. One of the TCOs used as an ARC material is AZO [52]. Cao et al., even reported that they were able to adjust the optical and electrical properties of AZO thin films deposited using the OAD process [53].

7.2 Growth conditions and characterization techniques

AZO thin films were grown on Corning 2947 glass substrates by the RF-sputtering method at 80 W process power during 25 min. A 3 inch ZnO: Al target with 2 wt% of Al_2O_3 was used to perform the deposition. The process pressure was fixed at 10 mTorr in argon environment. The distance between the substrate and target was 5 cm and no rotation was used in the course of the growth process. Before the deposition, the target was pre-sputtered 5 min. Each growth was performed using different tilting angles for the substrate holder (θ = 0°, 15°, 30°, 45°, 75°). X-ray diffraction measurements were performed using a D5000 Siemens X-ray diffractometer and CuKα radiation in the grazing incidence geometry with 1° inclination. The crystallite size (D) was calculated from evaluating angle position and full width at half maximum (FWHM) of the (0 0 2) ZnO peak in the Scherrer formula:

$$D = \frac{0.9\lambda}{FWHM Cos\theta_B} \quad (7.5)$$

Where λ = 0.15406 nm is the X-ray wavelength, θ_B the Bragg diffraction angle. Thickness and cross sectional morphology of the AZO nanocolumns were studied by using a field emission scanning electron microscope (FESEM) JEOL 7600F instrument. The samples were cleaved in the direction of the column tilt in order to explore their cross sections. The optical properties were obtained by an Agilent 8453 UV–Vis spectrophotometer. The electrical properties, resistivity, mobility and carrier concentration, were measured with an Ecopia HMS-5000 Van der Pauw Measurement System at room temperature.

7.2.1 Theoretical optical basis

The determination of the absorption profile from experimental transmission measurement T = I/I$_0$, where I and I$_0$ are the transmitted and incident light respectively, was carried out using the Beer–Lambert law and it's described by the expression [54]:

$$I = I_0 e^{-\alpha d} \tag{7.6}$$

Where α *(hv)* is the energy dependent absorption coefficient and *d* is the sample's thickness. The absorption coefficient of an inorganic semiconductor is experimentally defined by two regions. One of them is the absorption edge corresponding to the parabolic extremes of the energy bands and the other one the band tail, which is a consequence of the material disorder including the presence of doping impurities [54]. The expression that describes the absorption coefficient of an inorganic semiconductor is [55]:

$$\alpha(hv) = \begin{cases} A\left(hv - E_g\right)^{0.5} \forall\, hv \geq E_g \\ B e^{\frac{hv}{E_0}} \forall\, hv < E_g \end{cases} \tag{7.7}$$

Where E_g is the band gap energy, *hv* the energy, E_0 is the band tail parameter, while *A* and *B* are fitting coefficients. In practice, there is not a unique point where the absorption coefficient changes from tail to edge, but there is a certain energy range where both regions overlap, as can be experimentally observed. The Rayleigh scattering is the elastic scattering of the electromagnetic radiation by particles much smaller than the wavelength of the incident radiation. That is the case of scattering due to atoms, molecules and punctual defects in a quasi-homogeneous media, like a semiconducting film. The intensity of light scattered is given by the expression [56]:

$$I_{sc} = I_0 F(\theta_1, \varphi) \frac{k^4}{r^2} \left(\frac{n^2-1}{n^2+2}\right)^2 \left(\frac{D}{2}\right)^6 \tag{7.8}$$

Where I_0 is the intensity of the incident light, θ_1 is the observation angle with respect to incident light direction ($0° \leq \theta_1 \leq 180°$), φ is the azimuthal angle determined by the plane given by incident light and the scattered light directions ($0° \leq \varphi \leq 360°$), $F(\theta_1,\varphi)$ is the angular scattering function, *r* is the distance to the light source, $k = 2\pi/\lambda$ is the wave number in vacuum, *n* is the refractive index and $D << \lambda$ is the effective particle diameter. Therefore, the total light that is transmitted through the sample is given by:

$$I = I_0 F(\theta_1, \varphi) \frac{k^4}{r^2} \left(\frac{n^2-1}{n^2+2}\right)^2 \left(\frac{D}{2}\right)^6 e^{-\alpha d} \tag{7.9}$$

Where both the absorption and the scattering are included. Then, applying a logarithm and dividing by *d* in equation (7.9) an expression for an effective absorption coefficient α_{eff} is obtained:

$$-\frac{1}{d}ln\left(\frac{I}{I_0}\right) = \frac{1}{d}ln\left(\frac{I_{SC}}{I_0}\right) + \alpha = \alpha_{eff} \quad (7.10)$$

For $h\nu < E_g$ where the exponential behavior is valid as shown in equation (7.7) and considering the first term as a constant it is possible to approximate equation (7.10) to:

$$\alpha_{eff} \approx Constant + Be^{\frac{h\nu}{E_0}} \quad (7.11)$$

Additionally, the refractive index is a complex equation given by:

$$\hat{n} = n + ik \quad (7.12)$$

Where n is the real refractive index term and k is the imaginary term corresponding to the extinction coefficient. The extinction coefficient is related to the absorption coefficient by the expression $k = \alpha\lambda/4\pi$, where λ is the wavelength. The refractive index can be calculated from the expression [57]:

$$n = \left(\frac{1+R}{1-R}\right) + \sqrt{\frac{4R}{(1-R)^2} - k^2} \quad (7.13)$$

Where R is the normal-incident light reflection. In the region below the band gap energy the absorption $A \rightarrow 0$. Then the expression $T + R + A = 1$ can be reduced to $R = 1 - T$ from where it is possible to estimate the reflected light.

7.3 Results and discussions

7.3.1 Nanocolumnar tilting angle as a function of the substrate inclination

SEM images of the film cross section show the presence of columnar formations. The column tilts correspond to the inclination of the substrate holder. Figure 7.5 shows the SEM image of the columnar formation for substrate holder without tilting and a sample grown with the same conditions but for a substrate inclination of $\theta = 75°$. It is possible to observe the tilting of the columns by looking at the vertical dashed line. The columnar disposition is observed to be dense and without porosity. For the film grown without substrate inclination, the columns present a diameter around 20 nm and smaller at the base region and it increases up to about 40 nm at the top of the film. In the films grown using OAD, the columns keep a uniform diameter $D_{SEM} \approx$ 20–25 nm. Figure 7.5 also displays a surface SEM image of samples grown with a substrate inclination of $\theta = 75°$, where no cracks are observed, along a dense disposition of surface grains with an estimated average size of about 26 nm, although ranging between 20 and 30 nm, which agrees with the column diameter. Figure 7.6 displays the variation of the column tilting angle β as a function of the substrate holder inclination (θ). The point distribution presents a linear behavior given by the expression $\beta_f = (0.18 \pm 0.02)\theta$. The Fitted column tilt, β_f, will be used since it reduces the error due to deviations in the sample cleaving.

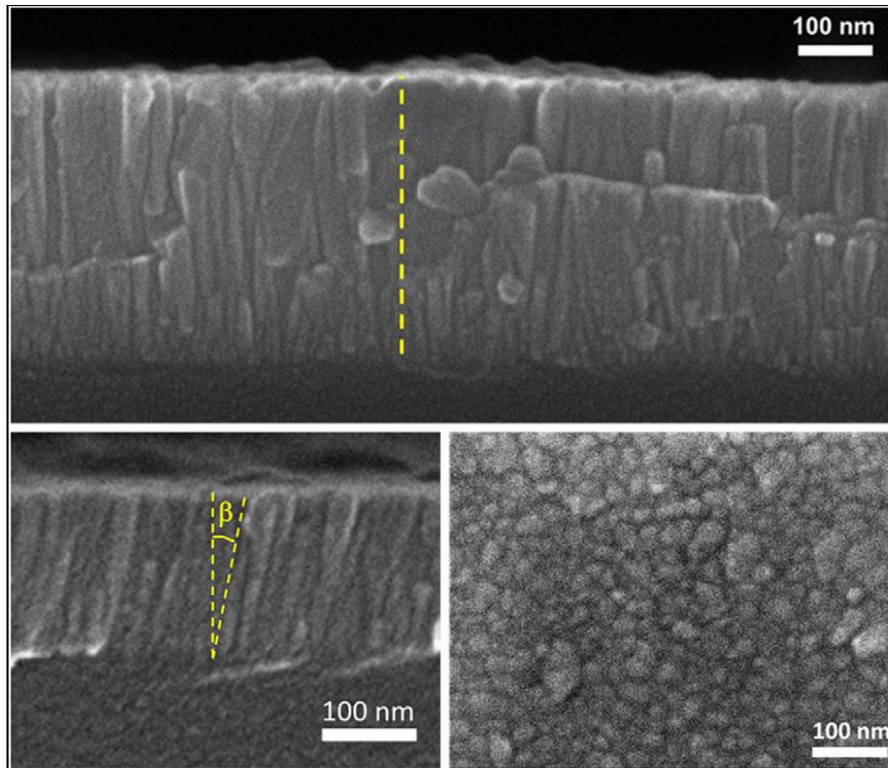

Figure 7.5 SEM image of AZO films without tilting (above), θ = 75° tilted (below left) substrate holder and surface SEM image of θ = 75° tilted (below right).

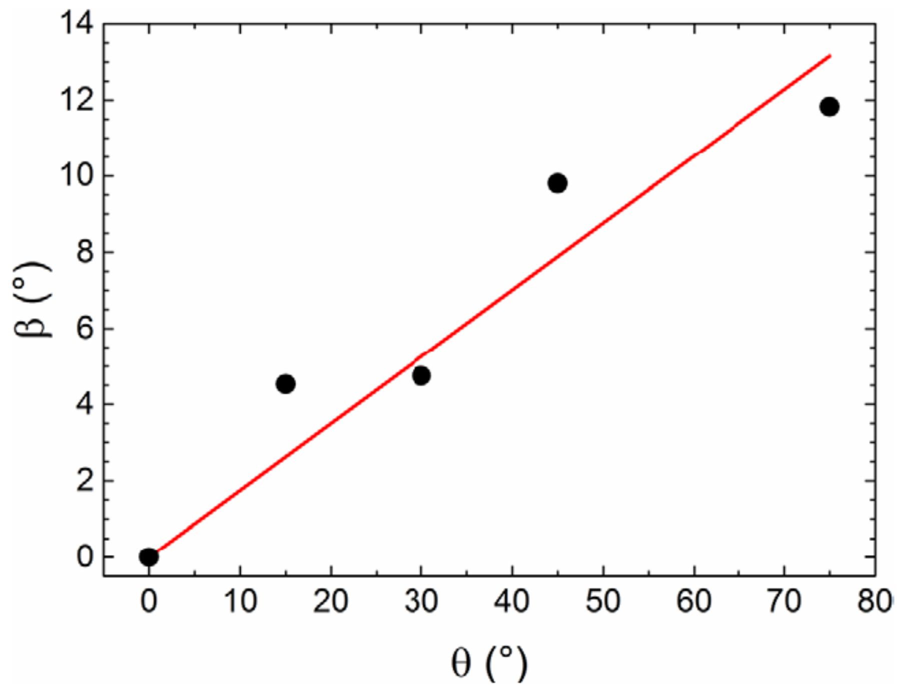

Figure 7.6 Nanocolumnar tilt angle dependence of substrate holder inclination.

7.3.2 Structural properties

The diffractograms of the AZO films grown with different substrate inclination are shown in Figure 7.7. All the peaks correspond to the ZnO wurtzite structure with hexagonal single phase as can be

seen in comparison with the standard pattern [58], which suggests that the Al atoms enter in the lattice Zn sites and form a solid solution of $Al_xZn_{1-x}O$. The preferential orientation is the (0 0 2) plane with respect to the substrate. For $\theta = 0°$ the (1 0 3) peak is also present. However, as the film columns slant the (1 0 1) and (1 0 2) peaks arise. This effect can be associated to the fact that the column inclination lets such planes also highlight. The diffractogram peaks shift to the left with respect to the pattern, which is indicative of an expanded lattice due to inward relaxation around the oxygen vacancies. The left shift of the peaks is also favored by the Al atoms with atomic radii smaller than that of Zn atoms occupying the Zn sites in the ZnO lattice, which leads to inward relaxation. The peaks in the sample with the highest substrate inclination, $\theta = 75°$, coincide with those of the pattern. This fact is associated to a compensation of the mentioned inward relaxation with stress–strain effects due to the slanted columns in the films, perhaps by increasing the other diffraction planes in the preferential growth direction, which could be confirmed by the peak widening. In general, the (0 0 2) peak position, $2\theta_B$, and the FWHM, did not exhibit a specific tendency and were considered to have central values $2\theta_B = (34.28 \pm 0.02)$ ° and FWHM = (0.34 ± 0.02)°. The crystallite size calculated by the Scherrer formula was found to be $D_{XRD} = (25 \pm 1)$ nm. This value agrees with the column diameter measured from the SEM images, which suggests that the columns in our samples are formed by stacked ~25 nm diameter crystallites.

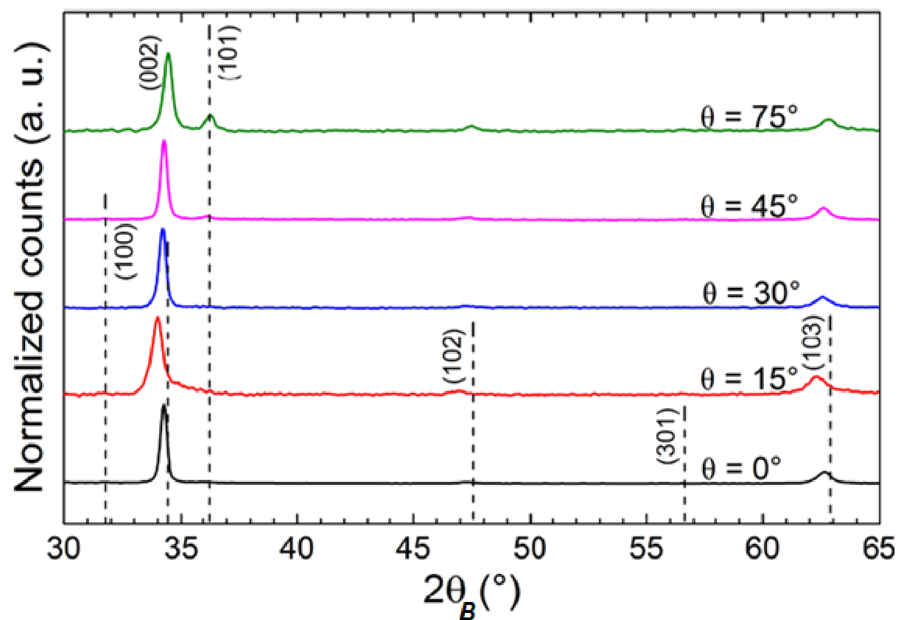

Figure 7.7 Diffractograms of AZO films as a function of the substrate inclination. Dashed lines correspond to the ZnO pattern diffractogram lines.

7.3.3 Optical properties

Figure 7.8 shows the transmission spectra of the samples obtained at different substrate angles. It is possible to observe oscillations in the high wavelength due to optical interference, typical in very thin films.

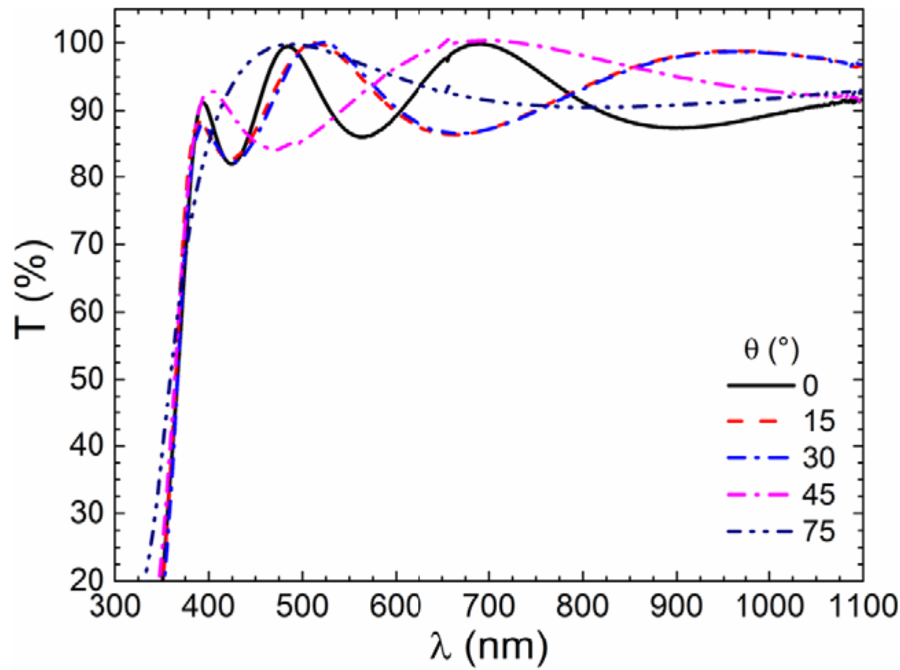

Figure 7.8 Optical transmittance spectra of the AZO thin films deposited at different tilting angles.

From these spectra the band gap energy with a Tauc plot given by plotting $(ahv)^2$ versus hv is determined, as shown in Figure 7.9. The inset displays the behavior of the band gap energy obtained from the intercept on the energy axis of the absorption edge linear region. The behavior of the band edge curves in figure 7.9 shows that the slope in the edge region diminishes with the increasing of the nanocolumnar tilting angle.

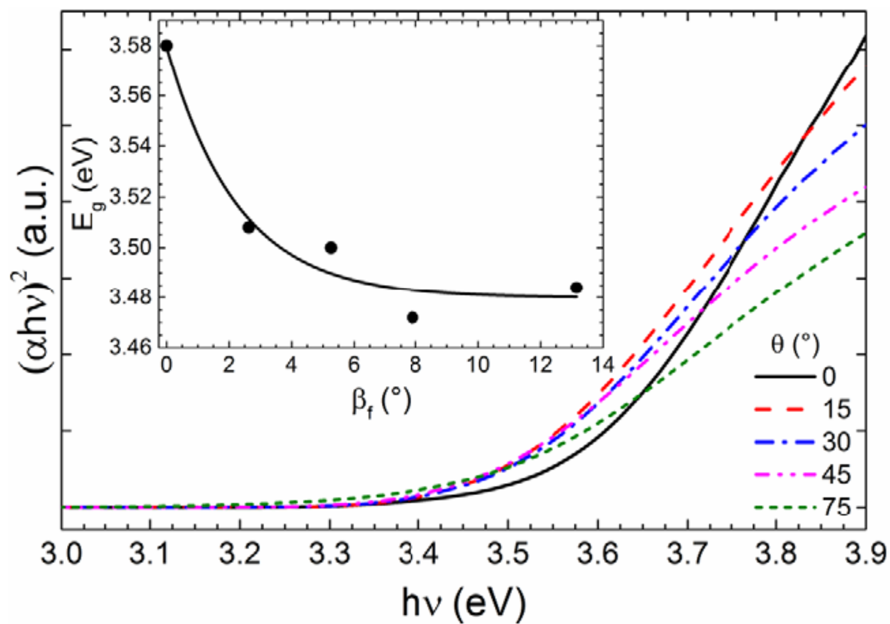

Figure 7.9 Tauc plot of AZO thin film grown at different tilting angles.

The band gap energy for non-tilted column films was found to be $Eg \approxeq 3.58$ eV. The band gap energy given by the introduction of 2 Al% in the lattice of $Al_xZn_{1-x}O$ is estimated to be $E_{gAl2\%} \approx 3.51$ eV, which is less than the band gap value found for this film. The measured electron concentration in the sample with no tilted substrate was $n \approxeq 1.9 \times 10^{20}$ cm^{-3}, which corresponds to a Moss–Burstein (MB)

shift of $\Delta E_{MB} \approx 0.42$ eV for a MB-shifted band gap energy $E_{gMB} \simeq 3.62$ eV, which is higher than the calculated one. For the other samples the electron concentration increases up to $n \simeq 4.4 \times 10^{20}$ cm^{-3}, which would induce an increase of the band gap up to about $E_{gMB} \simeq 3.89$ eV. This suggests that the band gap energy of non-tilted and tilted column films is due to the MB effect. However, as the film columns are tilted the band gap energy reduces, but in such a way that the band edges observed from absorption profiles gradually diminish their slope. All the samples were grown using the same target and no other growth conditions were changed except the substrate inclination. The experimental band gap diminishing effect is contrary to the MB effect. Then, the average Al concentration for all the samples must remain similar to the non-inclined substrate, but, although the samples are under MB effect, this behavior can be associated to local redistribution of Al atoms, i.e. the local Al concentration x in $Al_xZn_{1-x}O$ varies in a certain range around the average $x \simeq 0.02$ in such a way that the resulting absorption profile is given by a compositional mixture as has been previously proposed in compounds with three or more elements [59]. Thus, the edge linear prolongation intercepts the energy axis at $(\alpha h\nu)^2 = 0$ at lower energy values.

7.3.4 Optical processing

Optical interference, in the transmission spectra, hinders the determination of the optical properties of the samples, as shown in Figure 7.8. Thus, in order to eliminate the effect of the undesirable oscillations a mathematical processing is proposed in this section. The process is as follows: the graph $(\alpha h\nu)^2$ versus $h\nu$ is plotted by applying Beer–Lambert's law (equation (7.6)). Once the graph $(\alpha h\nu)^2$ versus $h\nu$ has been obtained, both absorption zones are identified according to equation (7.7). Since the oscillation significantly reduces in this plot, it is possible to fit the exponential tail region where there is no influence of the interference oscillations. The fitting, although is ruled by the exponential band tail, was applied in such a way that includes the mathematically damped oscillations. This method could allow obtaining a 'clean' tail absorption profile because the damped oscillations were only useful for determining the offset of the low absorption region y_0. The absorption profile in the tail region was obtained from the expression:

$$\alpha_f = \frac{1}{h\nu}\left[y_0 + Be^{\frac{h\nu}{E_0}}\right]^{0.5} \tag{7.14}$$

Once α_f, is obtained, the 'clean' transmittance could be recalculated with Beer–Lambert's law by:

$$T_f = e^{-\alpha t} \tag{7.15}$$

Plotting this new transmittance T_f, it can be observed that the interference oscillations are not present as exemplified in Figure 7.10. In this case, only absorption and scattering influence the refractive index. The inset of Figure 7.10 displays the damped oscillations using a logarithmic y-axis.

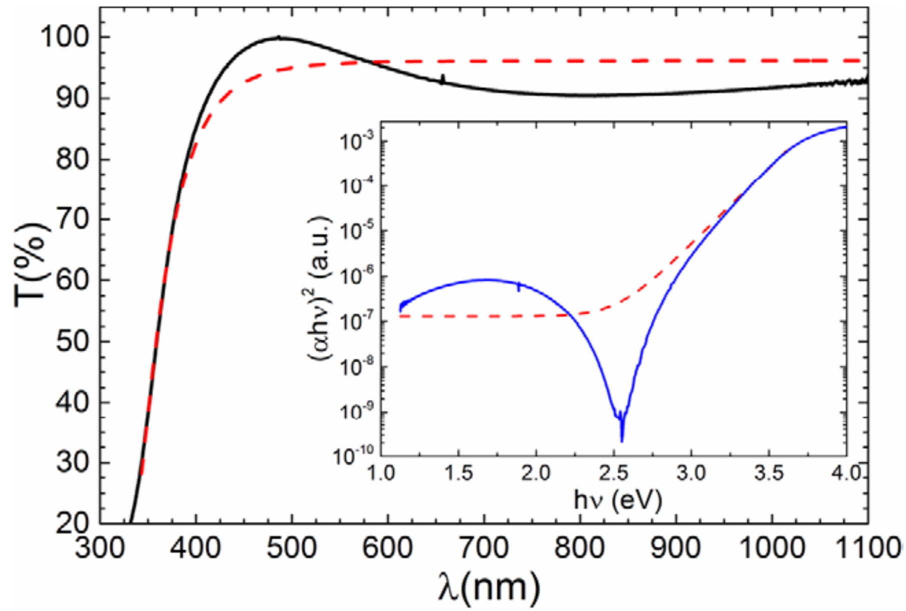

Figure 7.10 Plot of experimental optical transmission (solid line) and Tf (dashed line) of the sample grown at θ = 75°. The inset shows the exponential fitting applied in the plot of $(\alpha h\nu)^2$ as a function of hν where the dashed line corresponds to the fitted tail.

Figure 7.11 displays the calculated refractive index curves as a function of the wavelength using equation (7.13) and the proposed proceeding. For using equation (7.13), R was calculated from the expression $T + R + A = 1$, where A is the absorbed light. In the region of low absorption it is possible to consider that absorption is low, i.e. $k \rightarrow 0$. Then, the reflected light obtained from the fitted transmission is $R_f \approx 1 - T_f$, which is substituted in equation (7.13). Given that the extinction coefficient is actually defined not only by the absorption coefficient, but also by the scattering, it is also valid to consider an effective refractive index, n_{eff}.

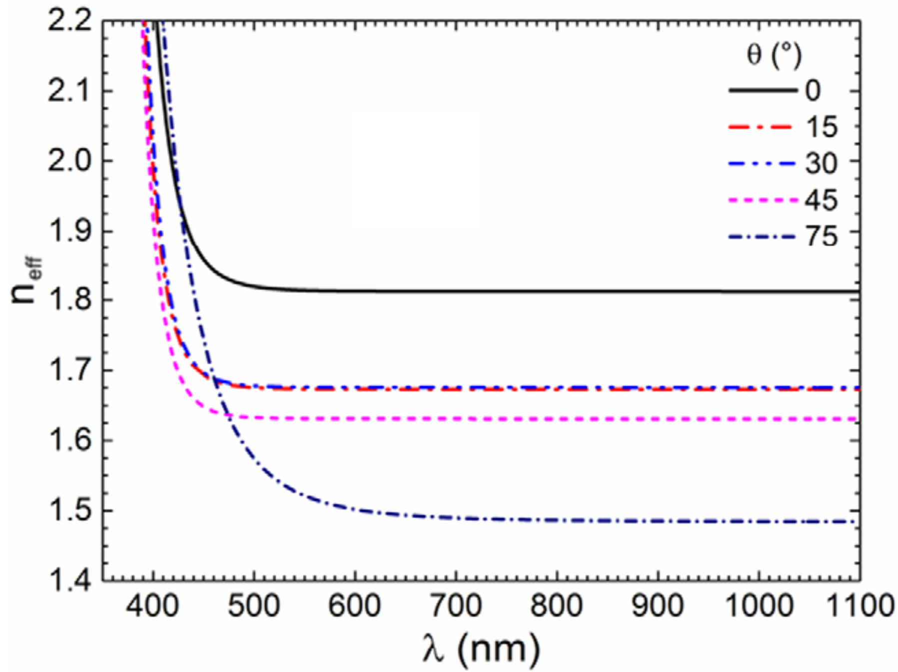

Figure 7.11 Behavior of the refractive index as a function of the wavelength for different substrate holder tilts.

7.3.5 Refractive index versus nanocolumnar tilt

Figure 7.11 shows the behavior of the refractive index as a function of the wavelength for the obtained samples. It is possible to observe the change due to the substrate inclination that films with slanted columns produce. The refractive index presents a sharp diminishing for energy around the band edge and for 600–650 nm the index presents low variation and has tendency to a constant as has been previously reported, even for AZO films [57]. Figure 7.12 displays the variation of the refractive index at λ = 700 nm as a function of the fitted columnar tilting.

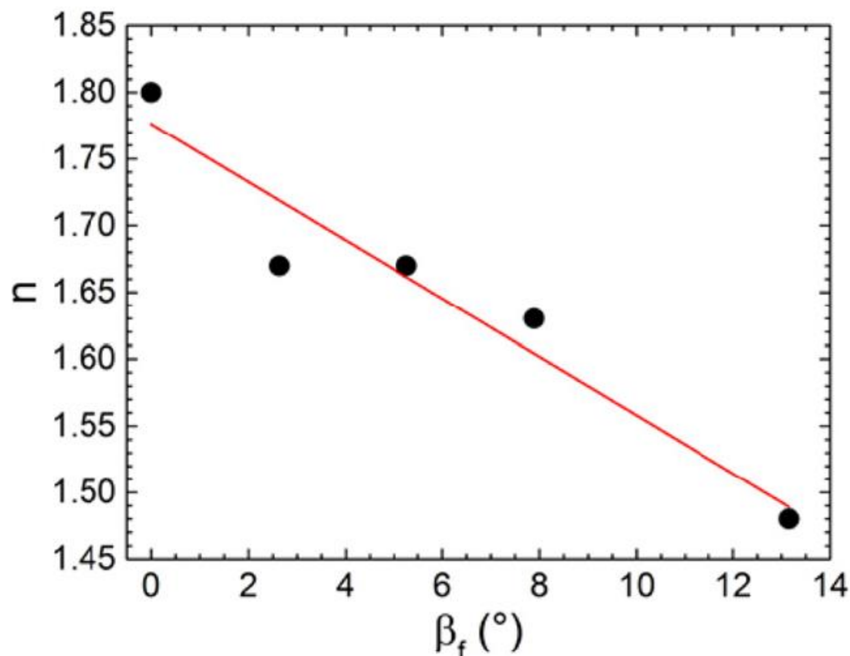

Figure 7.12 Effective refractive index at $\lambda \approx 700$ nm dependence on columnar tilting angle.

The refractive index varies from about $n \approx 1.78$ for $\beta_f = 0°$ to $n \approx 1.49$ for $\beta_f \approx 12–13°$ ($\theta = 75°$), which represents a variation of around 16%. The linear fitting of the refractive index as a function of column tilt angle is given by:

$$n_f = (1.78 \pm 0.03) - (0.022 \pm 0.004)\beta_f \tag{7.16}$$

In the non-inclined substrate case and with light incidence normal to surface, i.e. $\theta = 0°$ and $\beta_f = 0°$, the light falls on the base of the column. Considering good structural organization along the interior of the column, as was found from structural analysis, the main disorder can be only found on a columnar boundary or a lateral surface. This column boundary would be the most significant scattering source, but in this case it is given by the projection of the column lateral surface on the column base plane, which is a thin ring. Thus the light transmits mainly by the interior of the column without significant scattering and $F(\theta_I,\varphi)$ is minimum. However, as the substrate inclines the columns also do it and the projection of the tilted column gives an ellipsoid, as illustrated in Figure 7.13, which induces a higher interaction of light with the disordered column boundary and the scattering increases. Thus, it is possible to associate the column inclination with the scattering, i.e. $F(\theta_I,\varphi)$ increases with the column inclination.

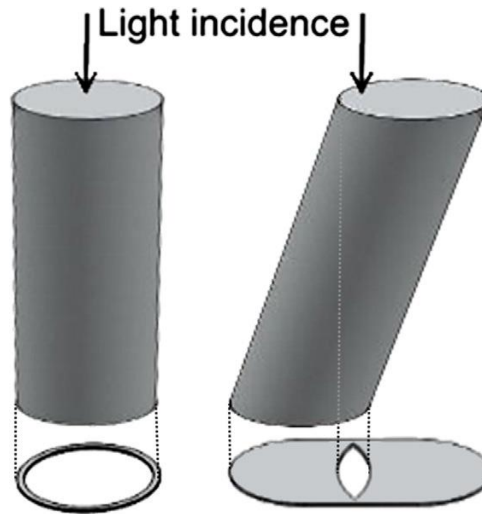

Figure 7.13 Scheme of the disordered area (shadowed region in the projection) that the light cuts across in vertical (left) and slanted (right) nanocolumns at normal incidence.

An optimized antireflective effect can be attained by using a multilayer with a grading refractive index. A proposal of multilayer with layer described in this chapter can gradually change the refractive index from that of the substrate up to that required as illustrated in Figure 7.14 (a). If, besides, it is combined with the optimum thickness of each layer according to the minimum reflection, as mentioned before, it is possible to build a multilayer structure in such a way that each layer maximizes the antireflection effect for a part of the electromagnetic spectrum and attain an anti-reflecting effect for a great part of the visible and infrared spectrum. Figure 7.14 (b) shows an experimentally obtained multilayer with the column tilted from 14.7° at the base to 0° at the top.

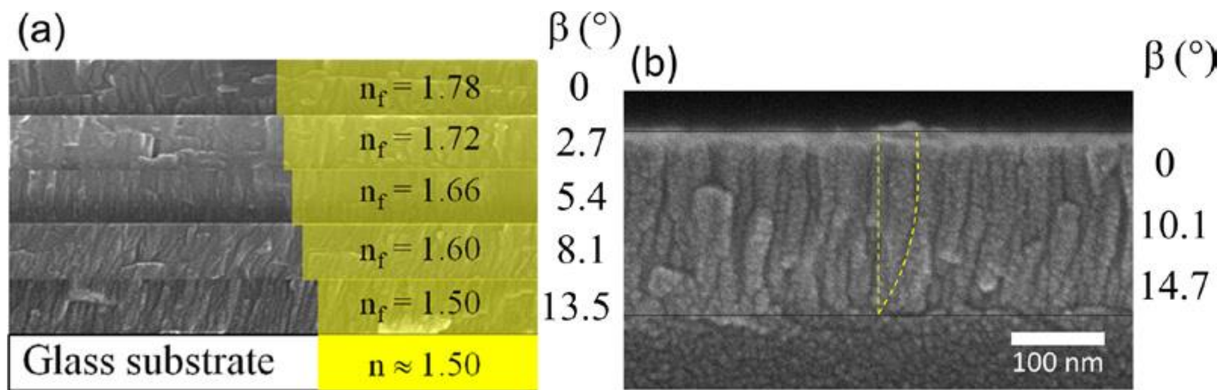

.

Figure 7.14 (a) Scheme of a suggested multilayer changing the nanocolumn tilt angle. Yellow bars proportionally illustrate the values of refractive index for each layer. (b) SEM image of an experimentally obtained multilayer with continuous variation of the nanocolumn tilt angle 14.7° to 0° with respect to the normal at the substrate.

7.4 Partial conclusions

The use of the OAD leads to the growth of dense films with tilted nanocolumns. The optical transmissions of samples were into a range of 85 and 100%. The band gap energy diminished with the substrate inclination presumably due to local variation of Al concentration in the material. The nanocolumns' tilt angle influences the light scattering that falls normal to the film surface. It induces the refractive index to vary in such a way that it diminishes as nanocolumnar tilting angle increases in a range from about 1.78 for no tilted substrate up to about 1.50 for 75° substrate inclination, which corresponds to 13.5° nanocolumnar tilting angle. This result allows refractive index engineering in order to optimize the antireflective effect in AZO films.

7.5 References

[1] A. Lakhtakia, R. Messier. Sculpured thin films: nanoengineered morphology and optics. The society of Photo-Optical instrumental engineers SPIE Bellingham Washington USA 2005

[2] Min Wook Pyun, Eui Jung Kim, Dae-Hwang Yoo, Sung Hong Hahna, Oblique angle deposition of TiO2 thin films prepared by electron-beam evaporation, Applied Surface Science 257 (2010) 1149–1153

[3] Sarkar S., Pradhan S.K. Tailoring of optical and wetting of sputter deposited silica thin films by glancing angle deposition. Applied surface Science 290 (2014) 509-513

[4] Zhengcao Li , Yu Zhu, Qin Zhou, Jie Ni, Zhengjun Zhang, Photocatalytic properties of TiO2 thin films obtained by glancing angle deposition, Applied Surface Science 258 (2012) 2766–2770

[5] Xiudi Xiao, Guoping Dong, Cheng Xu , Hongbo He , Hongji Qi , Zhengxiu Fan , Jianda Shao, Structure and optical properties of Nb2O5 sculptured thin films by glancing angle deposition, Applied Surface Science 255 (2008) 2192–2195

[6] Khedir R. Khedir, Ganesh K. Kannarpady, Hidetaka Ishihara, Justin Woo, Charles Ryerson, Alexandru S. Biris , Morphology control of tungsten nanorods grown by glancing angle RF magnetron sputtering under variable argon pressure and flow rate, Physics Letters A 374 (2010) 4430–4437

[7] Sumei Wang , , Xiaoyong Fu , Guodong Xia , Jianguo Wang , Jianda Shao , Zhengxiu Fan, Structure and optical properties of ZnS thin films grown by glancing angle deposition, Applied Surface Science 252 (2006) 8734–8737

[8] Shuhan Chena, Jingshu Liang, Yunjie Mo, Difan Luo, Shaoji Jiang, Onset of shadowing-dominated growth of Ag films in glancing angle deposition: Kinetic Monte Carlo simulation, Applied Surface Science 264 (2013) 552–556

[9]. Hawkeye, M. M., Taschuk, M. T. & Brett, M. J. Glancing Angle Deposition of Thin Films: Engineering the Nanoscale (John Wiley & Sons, Ltd, 2014)

[10] M.L. Kuo, D.J. Poxson, Y.S. Kim, F.W. Mont, J.K. Kim, E.F. Schubert, S.Y. Lin, Realization of a near-perfect antireflection coating for silicon solar energy utilization, Optics Letters 33 (2008) 2527–2529

[11] J.Q. Xi, M.F. Schubert, J.K. Kim, E.F. Schubert, M. Chen, S.Y. Lin, W. Liu, J.A. Smart, Optical thin-film materials with low refractive index for broadband elimination of Fresnel reflection ,Nature Photonics 1 (2007) 176–179

[12] Y.J. Park, K.M.A. Sobahan, C.K. Hwangbo, Wideband circular polarization reflector fabricated by glancing angle deposition , Optics Express 16 (2008) 5186–5192

[13] G.K. Kannarpady, R. Sharma, B. Liu, S. Trigwell, C. Ryerson, A.S. Biris, G.K. Kannarpady, R. Sharma, B. Liu, S. Trigwell, C. Ryerson, A.S. Biris, Appl. Surf. Silane decorated metallic nanorods for hydrophobic applications, Applied Surface Science 256 (2010) 1679–1682

[14] X. Yan, D.J. Poxson, J. Cho, R.E. Welser, A.K. Sood, J.K. Kim, E.F. Schubert, Enhanced Omnidirectional Photovoltaic Performance of Solar Cells Using Multiple‐Discrete‐Layer Tailored‐and Low‐Refractive Index Anti‐Reflection Coatings , Advanced Functional Materials, 23 (2012) 583-590

[15] Y.P. Zhao, S.H. Li, S.B. Chaney, S. Shanmukh, J.G. Fan, R.A. Dluhy, W. Kisaalita, J., Designing nanostructures for sensor applications Journal of Electronic Materials35 (2006) 846–851

[16] S.R. Kennedy, M.J. Brett, H. Miguez, O. Toader, S. John, S.R. Kennedy, M.J. Brett, H. Miguez, O. Toader, S. John, Optical properties of a three-dimensional silicon square spiral photonic crystal, Photonics and Nanostructures - Fundamentals and Applications 1 (2003) 37–42

[17] K. Robbie, C. Sit, M.J. Brett, Advanced techniques for glancing angle deposition, Journal of Vacuum and Science Technology B, 16 (1998) 1115

[18] F.C. Akkari, M. Kanzari, B. Rezig, Growth and properties of the $CuInS_2$ thin films produced by glancing angle deposition, Materials Science and Engineering: C 28 (2008), 692-696

[19] T. Vicsek Fractal growth phenomena, World Scientific (2nd ed.) (1992)

[20] D.X. Ye, Y.P. Zhao, G.R. Yang, Y.G. Zhao, G.C. Wang, T.M. Lu Manipulating the column tilt angles of nanocolumnar films by glancing-angle deposition, Nanotechnology 13 (2002) 615

[21] Fatemeh Hosseini Siyanaki, Hamid Rezagholipour Dizaji, Mohammad Hossein Ehsani, Shiva Khorramabadi, The effect of substrate rotation rate on physical properties of cadmium telluride films prepared by a glancing angle deposition method, Thin Solid Films 577 (2015) 128–133

[22] J.M. Nieuwenhuizen and H.B. Haanstra. Microfractography of thin films. Philips Technical Review 27 (1966) 87–91

[23] Tait, R. N., Smy, T. & Brett, M. J. Modelling and characterization of columnar growth in evaporated films. Thin Solid Films 226 (1993) 196–201

[24] Xiudi Xiao , Guoping Dong, Jianda Shao, Hongbo He, Zhengxiu Fan, Optical and electrical properties of SnO_2:Sb thin films deposited by oblique angle deposition, Applied Surface Science 256 (2010) 1636–1640

[25]. Alvarez, R. et al. Nanocolumnar growth of thin films deposited at oblique angles: Beyond the tangent rule. Journal of Vacuum Science & Technoogy. B 32 (2014). 041802

[26]. Álvarez, R. et al. Theoretical and experimental characterization of TiO 2 thin films deposited at oblique angles. Journal of Physics D: Applied Physics. 44 (2011) 385302

[27] Sumei Wang, Guodong Xia, Hongbo He, Kui Yi, Jianda Shao, Zhengxiu Fan, Structural and optical properties of nanostructured TiO_2 thin films fabricated by glancing angle deposition, Journal of Alloys and Compounds 431 (2007) 287–291

[28] E. Jiménez-Piqué, L. González-García, V.J. Rico, A.R. González-Elipe, Nanoindentation of nanocolumnar TiO2 thin films with single and stacked zig-zag layers, Thin Solid Films 550 (2014) 444–449

[29] J.J. Steele, G.A. Fitzpatrick, M.J. Brett, Nanostructured Metal Oxide Thin Films for Humidity Sensors, IEEE Sensors Journal 8 (2008) 1422–1429

[30] M.D. Fleischauer, J. Li, M.J. Brett, Columnar Thin Films for Three-Dimensional Microbatteries , Journal of Electrochemical Society 156 (2009) A33–A36

[31] J.G. Gibbs, Y.P. Zhao, Design and Characterization of Rotational Multicomponent Catalytic Nanomotors ,Small 5 (2009) 2304–2308

[32] Qin Zhou, Ye Yang, Jie Ni, Zhengcao Li, Zhengjun Zhang, Rapid detection of 2, 3, 30 , 4, 40 - pentachlorinated biphenyls by silver nanorods-enhanced Raman spectroscopy, Physica E 42 (2010) 1717–1720

[33] Yuping He , Jianguo Fan, Yiping Zhao, The role of differently distributed vanadium nanocatalyst in the hydrogen storage of magnesium nanostructures, International Journal of Hydrogen Energy 35 (2010) 4162–4170

[34] Motofumi Suzuki, Tadayoshi Ito, Yasunori Taga, Photocatalysis of sculptured thin films of TiO_2 , Applied Physics Letters 78 (2001) 3968–3970

[35] Liu H, Avrutin V, Izyumskaya N, Özgür Ü and Morkoç H., Transparent conducting oxides for electrode applications in light emitting and absorbing devices Superlattices Microstructures 48 (2010) 458–84

[36] Nistor M, Millon E, Cachoncinlle C, Seiler W, Jedrecy N, Hebert C and Perrière J 2015 Transparent conductive Nd-doped ZnO thin films Journal of Physics D: Applied Physics. 48 (2015) 195103–12

[37] Ellmer K. Past achievements and future challenges in the development of optically transparent electrodes Nature Photonics 6 (2012) 809–17

[38] Vattappalam S. C., Thomas D., Matthew T. R., Augustine S. , Mathew S., Band gap and conductivity variations of ZnO nano structured thin films annealed under vacuum, IOP Conference Series: Materials Science and Engineering 73 (2015) 012107

[39] P. Nunes, E. Fortunato, P. Tonello, F. Braz Fernandes, P. Vilarinho, R. Martins, Effect of different dopant elements on the properties of ZnO thin films, Vacuum 64 (2002) 281–285

[40] Bernal-Correa R, Morales-Acevedo A, Montes-Monsalve, Pulzara-Mora A., Design of the TCO (ZnO: Al) thickness for glass/TCO/CdS/CIGS/Mo solar cells, Journal of Physics D: Applied. Physics 49 (2016) 125601

[41] Sharma B. K., Khare N., Stress-dependent band gap shift and quenching of defects in Al-doped ZnO films Journal of Physics D: Applied Physics 43 (2010) 465402

[42] Treharne R. E., Hutchings K., Lamb D. A., Irvine S. J. C., Lane D, Durose K., Combinatorial optimization of Al-doped ZnO films for thin-film photovoltaics, Journal of Physics D: Applied Physics. 45 (2012) 335102

[43] Hernandez-Como N., Morales-Acevedo A., Aleman M., Mejia I., Quevedo-Lopez M. A. Al-doped ZnO thin films deposited by confocal sputtering as electrodes in ZnO based thin-film transistors, Microelectronic Engineering 150 (2016) 26–31

[44] Jeri'ann Hiller, Jonas D. Mendelsohn, Michael F. Rubner, Reversibly erasable nanoporous anti-reflection coatings from polyelectrolyte multilayers, Nature Materials 1 (2002) 59 - 63

[45] Sai H., Matsui T., Saito K., Kondo M., Yoshida I., Photocurrent enhancement in thin-film silicon solar cells by combination of anti-reflective sub-wavelength structures and light-trapping textures Progress in. Photovoltaics: Research and Applications 11 (2015) 1572–80

[46] Bruynooghe S., Tonova D., Sunderman M., Koch T., Schulz U., Antireflection coatings combining interference multilayers and nanoporous MgF2 top layer prepared by glancing angle deposition, Surface and Coatings Technology 267(2015) 40–4

[47] Deng C., Ki H., Pulsed laser deposition of refractiveindex- graded broadband antireflection coatings for silicon solar cells, Solar Energy Materials and Solar Cells , 147 (2016) 37–45

[48] Chen J. Y., Sun K. W. Growth of vertically aligned ZnO nanorod arrays as antireflection layer on silicon solar cells, Solar Energy Materials and Solar Cells 94 (2010) 930–4

[49] Yan X, Poxson D J, Cho J, Welser R E, Sood A K, Kim J K and Schubert E F 2013 Enhanced omnidirectional photovoltaic performance of solar cells using multiplediscrete- layer tailored- and low-refractive index antireflection coatings Advanced Functional Materials 23 (2013) 583-590

[50] Toledano D., Escobar Galindo R., Yuste M., Albella J. M. , Sánchez O., Compositional and structural properties of nanostructured ZnO thin films grown by oblique angle reactive sputtering deposition: effect on the refractive index, Journal of Physics D: Applied Physics46 (2013) 045306

[51] Chajed S., Schubert M. F., Kim J. K., Schubert E. F., Nanostructured multilayer graded-index antireflection coating for Si solar cells with broadband and omnidirectional characteristics, Applied. Phyics Letters 93 (2008) 251108

[52] Amita Verma, F. Khan, D. Kumar, M. Kar, B.C. Chakravarty, S.N. Singh, M. Husain, Sol–gel derived aluminum doped zinc oxide for application as anti-reflection coating in terrestrial silicon solar cells, Thin Solid Films 518 (2010) 2649–2653

[53] Cao S. P., Ye F., Hou B., Xu A. Y., Aluminum-doped zinc oxide film with gradient property deposited at oblique angle Thin Solid Films(2013) 545 205–9

[54] Smith R. A. Semiconductors (Cambridge: Cambridge University Press, 1964)

[55] Iribarren A, Castro-Rodríguez R, Sosa V and Peña J L Modeling of the disorder contribution to the bandtail parameter in semiconductor materials Physical Review B 60 (1999) 4758–62

[56] Seinfeld J. H. , Pandis S. N ., Atmospheric Chemistry and Physics 2nd edn (Hoboken, NJ: Wiley, 2006) ch 15.1.1

[57] Kim M S, Yim K G, Son J-S and Leem J-Y Effects of Al concentration on structural and optical properties of Al-doped ZnO thin films Bulletin of the Korean Chemical Society 33 (2012) 1235–41

[58] JCPDS-International Centre for Diffraction Data 2003 PCPDFWIN v. 2.4 Chart No. 89-0510

[59] Iribarren A., Menéndez-Proupin E., Caballero-Briones F., Castro-Rodríguez R., Peña J. L. Composition mixture probabilistic model in the formation of semiconductor materials obtained by random growth techniques Modern Physics Letters B 15 (2001) 643–646

GENERAL CONCLUSIONS

- Doped and undoped ZnO thin films were deposited on glass substrates using the pulsed laser deposition (PLD) and the rf-magnetron sputtering techniques.
- CdTe doped ZnO thin films were deposited by the PLD technique. The isoelectronic doping was confirmed by the presence of Zn-Te bonds, meaning that Te successfully passivated the oxygen vacancies in the ZnO crystal lattice.
- Nitrogen doped ZnO thin films were deposited by the PLD technique using a hybrid target made of pure ZnO powder embedded into poly (ethyl cyanoacrylate) matrix. The incorporation of the cyanoacrylate produced thin films with very low stress, similar to that of the standard ZnO powder pattern. The chemical analysis confirmed the successful nitrogen doping by means of the Zn-N bonds.
- Aluminum doped ZnO thin films were deposited using the rf-magnetron sputtering technique in order to study the effect of substrate rotation into the structural, optical, morphological and electrical properties of the obtained samples. The rotation speed of the substrate produced a well-defined columnar growth that became denser as the former increased. All samples presented high transmittance values (up to 90%) with increased band gaps in the range 3.49 to 3.67 eV, and electrical resistivities in the range of 10^{-2}-10^{-3} Ω cm.
- Aluminum doped ZnO thin films were deposited using the rf-magnetron sputtering technique along with the oblique angle deposition method. The OAD method resulted in the growth of nanocolumnar films, which presented different angles of inclination. The presence of the aforementioned nanocolumns influenced the light scattering process within the films, thus modifying their optical properties, especially its refractive index. The refractive index value changed from 1.78 for the thin film deposited with no inclination up to 1.50 for an inclination angle of 75°, which corresponded to nanocolumnar inclination angle of 13.5°.